INFORMATION TO USERS

This manuscript has been reproduced from the microfilm master. UMI films the text directly from the original or copy submitted. Thus, some thesis and dissertation copies are in typewriter face, while others may be from any type of computer printer.

The quality of this reproduction is dependent upon the quality of the copy submitted. Broken or indistinct print, colored or poor quality illustrations and photographs, print bleedthrough, substandard margins, and improper alignment can adversely affect reproduction.

In the unlikely event that the author did not send UMI a complete manuscript and there are missing pages, these will be noted. Also, if unauthorized copyright material had to be removed, a note will indicate the deletion.

Oversize materials (e.g., maps, drawings, charts) are reproduced by sectioning the original, beginning at the upper left-hand corner and continuing from left to right in equal sections with small overlaps. Each original is also photographed in one exposure and is included in reduced form at the back of the book.

Photographs included in the original manuscript have been reproduced xerographically in this copy. Higher quality 6" x 9" black and white photographic prints are available for any photographs or illustrations appearing in this copy for an additional charge. Contact UMI directly to order.

UMI

A Bell & Howell Information Company
300 North Zeeb Road, Ann Arbor MI 48106-1346 USA
313/761-4700 800/521-0600

Mechanical Properties of Bulk Metallic Glass Matrix Composites

Thesis by
Robert Dale Conner

In Partial Fulfillment of the Requirements
for the Degree of
Doctor of Philosophy

California Institute of Technology
Pasadena, CA 91125

1998
(Submitted October 28, 1997)

UMI Number: 9818773

UMI
300 North Zeeb Road
Ann Arbor, MI 48103

For Susan

ACKNOWLEDGMENTS

When I graduated from high school, our class song was *The Long and Winding Road*. It was a suprisingly good choice, coming from young people who had never been away from the safety of home. My journey has taken many paths. I have watched the sun rise from a muddy foxhole on a freezing morning, and while piloting an aircraft between cloud layers. I have spent the sunrise hours bathed in the glow of a radar display, in a room where the sun never shines. Our lives can change forever in the blink of an eye. One of those moments happened to me on September 8, 1991. I found myself on the edge of a chasm, unable to return to my former life, and with the need to build a bridge to the future. Caltech was the ideal place at which to begin.

I would like to thank Dr. Garland Scott, who, above all else, encouraged me to attend graduate school. I will always be indebted to Dr. Tom Christman, without whom I never would have attended Caltech; to Dr. Brent Fultz, who wisely suggested a leave of absence rather than withdrawal; and to both because they facilitated my return when I was ready. My advisors, Dr. Ares Rosakis and Dr. William Johnson, provided far more than guidance and financial support; I will always be grateful for their good humor and faith in my abilities.

Richard Dandliker became much more than my coinvestigator on the metallic glass composite project. We obtained a synergism in developing the composites which strengthened a friendship that I trust will always endure. Karina (Montilla) Edmunds was an entertaining, if somewhat disorganized, office mate. .Pam Albertson was the grease that lubricated the bureaucratic wheels. Haein Choi-Yim contributed the samples of particulate reinforced composite for testing, and her laughter was infectious. Carol Garland was an invaluable resource in the microscopy lab. So many others contributed to my stay at Caltech: the machine shop and physical plant personnel, the secretarial and custodial staff, and my fellow students. A partial list would include Stephen Glade, Xianghong Lin, Mo Li, Dave Lee, Mohit Jain, Ralf Busch, Andy Masuhr, Sven Bossuyt, Valerie Scruggs, Heather Frase, Chuck Witham, Tab Stephens, Dave Owen, and the staff at the Red Door Cafe.

Finally I must acknowledge the contribution of my wife, Susan, who kept me sane and was a bottomless well of encouragement. I could not imagine my life without her.

Now my bridge is nearly complete. There will be new paths to take, fresh challenges, and more turns in my road. It has been an interesting trip in the years since high school, and, when I look back I think, what a long, strange trip it's been.

ABSTRACT

This report discusses two aspects of research on bulk metallic glasses The first is an effort to increase their toughness by combining them with reinforcement to form a composite. The second is the first direct measurement of plane strain fracture toughness of bulk metallic glass.

Particulate and continuous fiber reinforced composite materials were fabricated using bulk metallic glass as the matrix. The particulate composites combined W, WC, SiC and Ta reinforcements in a matrix with the composition $Zr_{57}Nb_5Al_{10}Cu_{15.4}Ni_{12.6}$. Continuous fiber composites were fabricated using W and 1080 carbon steel (music) wire reinforcement in a $Zr_{41.25}Ti_{13.75}Cu_{12.5}Ni_{10}Be_{22.5}$ matrix. In both cases the metallic glass remained amorphous during processing.

Compressive strain to failure was greatly enhanced in both particulate and continuous fiber composites by the formation of multiple shear bands. Tungsten reinforcement provided the greatest improvement. The tungsten is wet well by the metallic glass, and forms a strong interface.

Both particulate and fiber reinforced composite showed improved tensile properties. Energy (per unit volume) to break increased 52% for 5% V_f, 150 μm W reinforced $Zr_{57}Nb_5Al_{10}Cu_{15.4}Ni_{12.6}$ and 18% for 60% V_f music wire reinforced $Zr_{41.25}Ti_{13.75}Cu_{12.5}Ni_{10}Be_{22.5}$. Tightly bonded ductile particles and weakly bonded continuous fibers proved best for enhancing the tensile properties of bulk metallic glass.

Fracture toughness of the unreinforced $Zr_{41.25}Ti_{13.75}Cu_{12.5}Ni_{10}Be_{22.5}$ bulk metallic glass was determined using 3-point bend measurements and coherent gradient sensing

(CGS). The measured fracture toughness is nominally 55 MPa√m. Once initiated, cracks in the unreinforced metallic glass propagated in an unstable manner. Continuous fiber reinforcement was demonstrated to arrest crack propagation in 3-point bend fracture tests of bulk metallic glass matrix composites.

TABLE OF CONTENTS

CHAPTER 1

INTRODUCTION

1.1 Motivation and Objectives

Metallic glasses were discovered by Klement, Willens, and Duwez at the California Institute of Technology in 1960[1]. Rapidly quenching a Au-Si alloy, using "splat-cooling" to produce a cooling rate on the order of 10^6 Ks^{-1}, suppressed crystallization and produced thin wafers of glassy metal. Over the next two decades glass forming systems based on Fe, Pd and Ni were discovered[2,3]. Cooling rates of 10^4 to 10^6 Ks^{-1} were required for all of the glass forming alloys. The high cooling rates required samples to be thin, typically about 50 μm.

The thin samples limited the types of mechanical tests that could be performed on these early glasses. However, the metallic glass exhibited remarkable behavior in the tests that were performed. Tensile tests on ribbons revealed strength approaching theoretical values, with $\sigma \sim E/50$ [4]. Fracture toughness measurements of Fe and Ni based glasses showed K_{IC} values from 10 to 50 MPa√m (although, because of the thin sections, this was not plane strain fracture toughness)[3,5]. The elastic modulus of a Pd-Si glass was determined to be 50 GPa[4]. These mechanical properties of the metallic glass, combined with its low density, promised high specific strength and good specific stiffness. Unfortunately, the material showed no room temperature ductility and failed due to shear localization. Chemically etching cold rolled metallic glass ribbons revealed that the material deformed from localized plastic deformation in a diffuse network of shear bands[6,7].

In 1969 Chen and Turnbull made a $Pd_{78}Cu_6Si_{16}$ metallic glass with a critical cooling rate of 10^3 Ks^{-1}[8]. This glass could be cast into 2 mm rods, which allowed more extensive mechanical testing to be performed. Uniaxial compression tests revealed that the glass behaved in an elastic-perfectly plastic manner. The material showed significant compressive ductility prior to catastrophic failure due to fracture along shear bands[9]. Kimura and Masumoto, attempting to complete the quasi-static constitutive characterization of this alloy, determined that the material obeyed a von Mises yield condition[10]. There is, however, some contention over this. In 1989 Donovan performed experiments on a $Pd_{40}Ni_{40}P_{20}$ glass and found it to obey a pressure sensitive Mohr-Coulomb yield criterion[11].

In 1993 Peker and Johnson, at the California Institute of Technology, discovered a metallic glass with a critical cooling rate of 1 Ks^{-1}[12]. This glass, which has a nominal composition of $Zr_{41.25}Ti_{13.75}Cu_{12.5}Ni_{10}Be_{22.5}$ and goes by the trade name Vitreloy® 1, could be cast in evacuated quartz tubes with a diameter of up to 16 mm. This discovery was followed by the work of Bruck, et al., who determined the quasi-static constitutive behavior of this glass[13]. Bruck found the glass to obey a von Mises yield criterion. Ductility, though still limited, varied slightly with the addition of up to a small percentage of Boron and also with quench rate. Study of quasi-static and dynamic compression showed that the glass was insensitive to strain rate[14]. The mechanical properties of this glass are listed in Table 1.1 [14, 15, 16].

This bulk glass forming alloy shares a property with all other metallic glasses: catastrophic failure occurs with the formation of shear bands, or narrow regions of intense

Property	Value
Young's Modulus	96 GPa
Shear Modulus	34.3 GPa
Poisson's ratio	0.36
Tensile yield strength	1.9 GPa
Strain to failure	2 %
Plane Strain Fracture Toughness, K_{IC}	55 MPa $m^{1/2}$
Hardness (Vickers)	534 kg/mm^2
Coefficient of thermal expansion	10.1 x 10-6/^{0}C
Density	6.11 g/cm^3

Table 1.1 Mechanical Properties of $Zr_{41.25}Ti_{13.75}Cu_{12.5}Ni_{10}Be_{22.5}$ Metallic Glass

plastic deformation. In tension, the metallic glass shows no inelastic deformation prior to failure, while in compression it does show limited plastic deformation for some geometries. Unfortunately, useful structural applications rarely afford the luxury of being loaded only in compression.

This leads to the purpose of the work reported here. In an effort to increase the toughness of the bulk metallic glass (or, at least to reduce the inclination of catastrophic failure), composite materials were fabricated using ductile metal wires and particles to reinforce a bulk metallic glass forming matrix. The quasi-static mechanical properties of the composite were then measured using compression, tension and 3-point bend tests.

1.2 Brittle Matrix Composites

The McGraw-Hill Dictionary of Scientific and Technical Terms (4th ed.) defines a composite as "a structural material composed of combinations of metal alloys or plastics, usually with the addition of strengthening agents." The strengthening agents may be ductile or brittle materials in the form of particles, short fibers (whiskers) or continuous fibers, which are embedded in a polymer, metal or ceramic matrix.

Composite materials are desirable because by combining materials one can obtain properties that no single material can provide. For example, the most common composite, glass reinforced plastic (or fiberglass), is ubiquitous because it is relatively inexpensive and easily formed into complex shapes. Other types of composites exploit other properties; for example, tungsten-reinforced copper is a metal matrix composite that combines low thermal expansion with high thermal conductivity. Many engineering applications require materials with high specific strength and stiffness, stability at high temperatures, high energy absorption, e.g., bullet proof vests, and so on. While no single material can deliver the desired properties, many composite materials can.

Ceramic materials have excellent resistance to harsh environments and high temperatures, but, unfortunately, are brittle. This lack of toughness limits their use in many applications. This motivates the fabrication of ceramic matrix composites; the ceramic matrix contributing the high temperature properties, with the reinforcement improving the toughness by providing resistance to crack growth.

Increases in crack resistance for a metal-reinforced brittle matrix material was shown by Forwood and Forty[17] with sodium chloride crystals reinforced by metallic gold particles. Since then, numerous studies have shown that brittle materials (particularly glass) can achieve increased strength, fracture toughness and elastic modulus when combined with ductile reinforcements[18-28].

Most ductile-metal glass-matrix composite studies employed spherical particles. Troczynski, Nicholson and Rucker demonstrated that strength enhancement depends upon reinforcement volume fraction, rather than particle size[27]. Their study showed monotonically increasing strength with particle volume fraction (V_f), with a 2-fold increase in strength in a silicate glass reinforced with 40% V_f aluminum alloy particles. Benefits diminished with $V_f > 50\%$. Similar strength improvements were reported in tungsten-reinforced silica-glass[23], vanadium-reinforced borosilicate glass[24], and tungsten-reinforced sodium borosilicate glass[22].

Most favorable strength enhancement occurs when the thermal expansion coefficients of the reinforcement and matrix are equal[21,25]. Residual stresses imposed as a result of differential thermal expansion caused asymmetrical behavior in tensile and compressive strength[20].

Toughness is also improved in glass reinforced with ductile particles. Jessen, Mecholsky and Moore produced a 6-fold increase in fracture toughness of a 60% V_f Fe-Ni-Co reinforced borosilicate glass[26]. Krstic, et al., reported a 60x increase in toughness for a sodium-silicate glass reinforced with partially oxidized aluminum particles[21]. The increases in toughness apparently come from the cracks being guided to the particles (as a result of residual stresses from thermal mismatch) then dissipating energy by plastically deforming the particle. The most ductile particles provide the largest increase in toughness[25].

Krstic claimed that the largest increase in toughness occurs when thermal expansion between glass and particle (α_m and α_p, respectively) are matched, resulting in low residual stress[21]. When $\alpha_p > \alpha_m$ the matrix is placed in compression and cracks bypass particles. If $\alpha_p < \alpha_m$ the cracks are attracted to the particle due to residual tensile stresses in the matrix; however, the presence of tensile stress in the matrix lowers the load at which it fails. This disagrees with the work of Donald, Metcalf and Bradly, who found best improvements in strength when α matched, and largest increases in toughness when $\alpha_p > \alpha_m$.[18]

Toughness is also affected by the bond between the matrix and reinforcement. In brittle matrix composites reinforced with a brittle fiber, e.g., SiC in a ceramic matrix, an increase in toughness results from the weakly bonded fiber being pulled away from the matrix as the crack advances[19]. In a composite with ductile particle reinforcement, however, a tightly bonded particle applies a closure traction to the advancing crack. Energy is then absorbed by the particle as it plastically deforms, as illustrated in Figure 1.1. Several studies have demonstrated that tightly bonded ductile metal particles increase the toughness of glass[19,21,24,25]. Large increases in toughness may be available if the two mechanisms (pull-out and plastic deformation) can be combined.

1.2.1 Metallic Glass Composites

As noted previously, metallic glasses fail catastrophically in a narrow band of large shear strain and have no noticeable macroscopic inelastic deformation. If numerous shear bands, rather than one, can be generated then the metallic glass may be able to undergo significant deformation prior to failure. This motivates the fabrication of composites of metallic glass. Metallic glass ribbon has been used as reinforcement in oxide glass/metallic glass laminates[30], and also as the reinforced phase in ductile metal/metallic glass composites[29, 31-34]. To date no one has reported using a metallic glass as the matrix phase in a composite.

The first metallic glass/ductile metal composites were reported by Cytron in 1982[31]. He vacuum hot pressed short $Ni_{60}Nb_{40}$ metallic glass ribbons between wafers of superplastic aluminum at 450-500 °C. The reinforcement retained its glassy nature through the processing. No mechanical tests were reported.

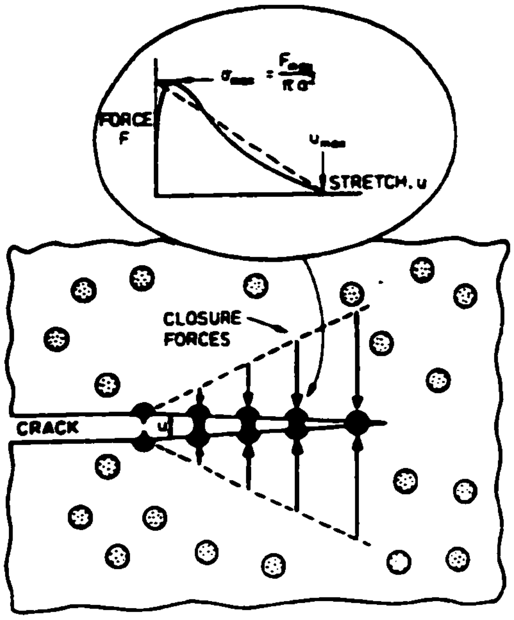

Figure 1.1 A crack in a brittle matrix, intersected by ductile particles. The particles stretch and fail as the crack opens. The work of stretching contributes to the toughness of the composite. The force-distance curve for the stretching of one particle is shown inset (from Bannister, et al.)[43].

Vaidya and Subramanian fabricated a laminate consisting of a 25 μm Fe-B-Si (Metglas® 2605S-2) ribbon sandwiched between two 0.5 mm plates of Corning 7572 (PbO-ZnO-B_2O_3-SiO_2-Al_2O_3) glass[30]. This corresponds to a reinforcement volume fraction of 2.5%. The edge notched specimen was tested in bending. They found up to a 6-fold increase in K_{IC}, depending upon the metallic glass/glass bond strength. Weak bonding provided the largest increase in toughness as a result of debonding and fiber pull out.

Leng and Courtney constructed brass (70% Cu, 30% Zn)/metallic glass (MBF-35, $Ni_{91}B_2Si_7$) laminates ($V_f = 7\%$) which were tested in tension and as edge-notched specimens in bending[29,32,34]. The metal reinforcement allowed for multiple shear band generation, resulting in enhanced strain to failure (from 1.3% for the glass alone to ~2% for the composite), while suppressing catastrophic failure. Stable crack growth in the bend specimens was combined with multiple shear bands forming at the crack tip to provide enhanced deformation of the metallic glass. Similar results were found in tensile and rolling tests performed by Alpas and Embury on a composite of $Ni_{78}Si_{10}B_{12}$ diffusion bonded to copper[33].

1.3 Composite Models

Composite materials are composed of two (or more) phases with differing properties. In a metal matrix composite, the difference in the constituents' respective thermal expansion coefficients will cause residual internal stresses to form upon cooling from the processing temperature. The combination of the mechanical properties of each component, i.e., elastic modulus and Poisson's ratio, and the relative amount of each phase present, determines the physical properties of the finished composite and the distribution of stresses within the composite when a load is applied. Several models have been developed to predict the composite properties based on the properties of each component. Four models will be reviewed here: the slab model (or rule of mixtures)[35]; the shear-lag model[35,36], the coaxial cylinder model[35,37,38], and the Eshelby equivalent inclusion model[35,44,45]. Each model has a regime of fiber length over which it is most applicable. The slab and coaxial cylinder models are most effective for continuous fiber composites.

The Eshelby method is particularly applicable to particulate and short fiber composites. The shear-lag model is useful on long fiber composites (or high aspect ratio whiskers) when fiber-matrix bond strength and load transfer are taken into consideration. Finite element analysis may also be used to calculate composite stresses as a result of load or thermal strain, although this is not strictly in the realm of a physical model.

1.3.1 The Slab Model

The slab model is used to calculate physical properties of a composite made up of continuous, aligned fibers (Figure 1.2). The model assumes that, for loads applied in the axial (3) direction, the strain of the composite (ε_c) is the same as the strain of the fibers (ε_f) the matrix (ε_m):

$$\varepsilon_{3c} = \varepsilon_{3f} = \varepsilon_{3m} \tag{1.1}$$

The applied axial force, F, is shared by the fibers and the matrix:

$$F_{3c} = F_{3f} + F_{3m} \tag{1.2}$$

which may be expressed in terms of stress:

$$\sigma_{3c} A_c = \sigma_{3f} A_f + \sigma_{3m} A_m \tag{1.3}$$

Dividing through by the composite area, A_c and converting area fractions to volume fractions (by multiplying each area by the length, l), gives the relationship for the axial stress:

$$\sigma_{3c} = f\sigma_{3f} + (1-f)\sigma_{3m} \tag{1.4}$$

where f represents the volume fraction of the reinforcement phase. The elastic modulus may be obtained from 1.4 using Hooke's law:

$$E_{3c} = \frac{\sigma_{3c}}{\varepsilon_c} = \frac{f\sigma_{3f}}{\varepsilon_f} + \frac{(1-f)\sigma_{3m}}{\varepsilon_m} = fE_f + (1-f)E_m \tag{1.5}$$

This is the "rule of mixtures," and illustrates that the composite properties are simply the weighted mean of the matrix and reinforcement properties, and will vary linearly with fiber volume fraction.

The transverse properties are obtained in a similar manner, except that stress, not strain, is assumed equal in both the reinforcement and the matrix. The composite strain is then expressed as a weighted average:

$$\varepsilon_{2c} = f\varepsilon_{2f} + (1-f)\varepsilon_{2m} \tag{1.6}$$

and the transverse composite modulus is given by:

$$E_{2c} = \left[\frac{f}{E_f} + \frac{(1-f)}{E_m}\right]^{-1} \tag{1.7}$$

While the axial model, under the equal strain assumption, gives results in good agreement with experiment, the equal stress assumption in this transverse case is not as reliable. Various other models have been developed to improve the accuracy, including the Halpin-Tsai model[39], the Spencer model[40] and the Eshelby model[35].

The slab model may also be used to predict shear moduli and Poisson contractions. Shear modulus (G) is related to shear stress (τ) and shear strain (γ) in a manner similar to Hooke's law:

$$\tau_i = G_{ij}\gamma_j \tag{1.8}$$

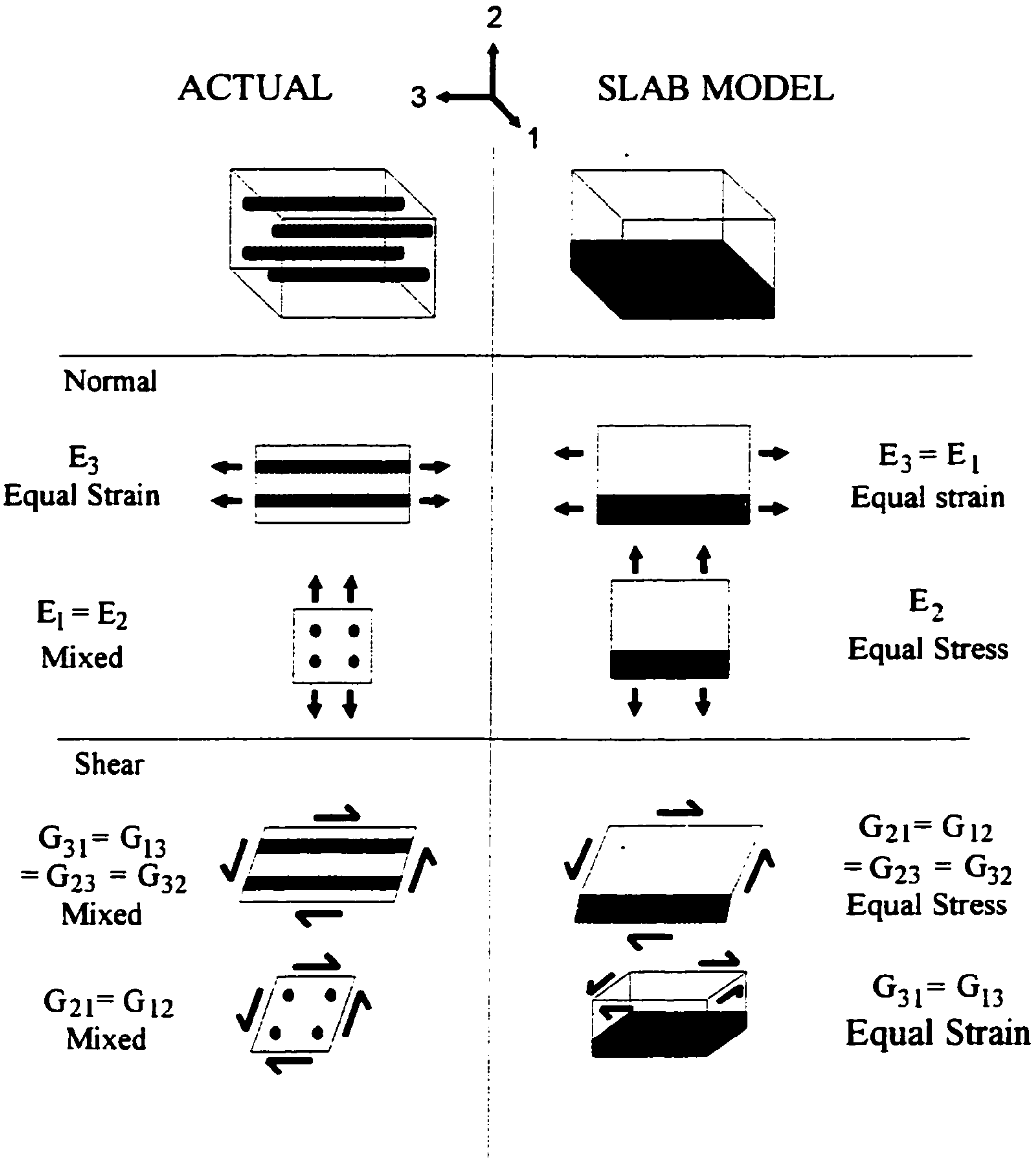

Figure 1.2 Comparison between real uniaxial, continuous fiber composite and slab model (from Clyne and Withers)[35].

A shear stress, τ_{ij} $(i \neq j)$, refers to a stress acting in the i direction on the plane with a normal in the j direction. A shear strain, γ_{ij} is a rotation of the j axis toward the i direction. In a continuous fiber composite the 1 and 2 directions are equivalent to each other, but not to the 3 direction, which leads to two shear moduli: $G_{32c} = G_{23c} = G_{13c} = G_{31c} \neq G_{21c} = G_{12c}$. The relationships for shear moduli are derived in a similar way those of Young's modulus and transverse modulus:

$$G_{32c} = \left[\frac{f}{G_f} + \frac{(1-f)}{G_m}\right]^{-1} \quad (1.9)$$

and

$$G_{31c} = fG_f + (1-f)G_m \quad (1.10)$$

Poisson's ratio, ν_{ij}, is defined as the contraction in the j direction as a result of a strain in the i direction:

$$\nu_{ij} = -\frac{\varepsilon_j}{\varepsilon_i} \quad (1.11)$$

Under the equal strain assumption of axial loading, the contractions in the 1 and 2 direction follow a rule of mixtures model:

$$\nu_{32c} = \nu_{31c} = -\frac{\varepsilon_2}{\varepsilon_3} = f\nu_f + (1-f)\nu_m \quad (1.12)$$

From the interrelationship of elastic constants provided by Nye[41], $\frac{\nu_{32}}{E_{3c}} = \frac{\nu_{23}}{E_{2c}}$, which may applied to find the Poisson contractions of a transversely loaded material:

$$\nu_{23c} = \left[f\nu_f + (1-f)\nu_m\right]\frac{E_{2c}}{E_{3c}} \quad (1.13)$$

This will be inaccurate to the degree of error in calculating E_{2c}. It will be lower than ν_{32c} because, when loaded transversely, the fibers will strongly resist axial contraction. This resistance to contraction will cause a substantial contraction in the other transverse direction, so that ν_{21c} will be high. An expression for ν_{21c} is obtained by considering the overall volume change experienced by the material[42] leading to:

$$\nu_{21c} = 1 - \nu_{23c} - \frac{E_{2c}}{3K_c} \qquad (1.14)$$

where K_c is the bulk modulus of the composite, which may be estimated using the equal stress assumption:

$$K_c = \left[\frac{f}{K_f} + \frac{(1-f)}{K_m}\right]^{-1} \qquad (1.15)$$

The bulk moduli of the fiber and matrix components may be calculated from their respective elastic constants through the expression:

$$K = \frac{E}{3(1-2\nu)} \qquad (1.16)$$

The slab model provides good estimates of the elastic properties and component stresses when loaded in the axial direction. The predictions are generally worse when considering transverse loading. Its use becomes limited when applied to discontinuously reinforced composites.

1.3.2 The Shear Lag Model

The shear lag model was developed to describe the behavior of composites with aligned discontinuous fibers, and also to include the effects of matrix/fiber interfacial strength on load transfer between the fiber and the matrix. Referring to figure 1.3, balancing the force that comes from the shear stress acting on the fiber surface with the force as a result of axial stress in the fiber leads to:

$$\sigma_{zz}\pi r^2 = \tau_{rz} 2\pi rz \qquad (1.17)$$

where σ_{zz} = axial stress along the fiber length

τ_{rz} = shear stress acting along the fiber-matrix interface at the ends of the fiber

r = fiber radius

z = shear stress transfer length (distance from each fiber end)

Rearranging (1.17) gives: $$\sigma_{zz} = \frac{2\tau_{rz} z}{r} \tag{1.18}$$

As depicted in figure 1.4, when $z = 0$ there is no stress in the fiber; the stress gradually builds up along the fiber length, reaching a maximum at $z = l_c/2$, where l_c is defined as the critical length of the fiber. At this point, the fiber will either begin to deform plastically or break. Replacing z with $l_c/2$ and $d = 2r$ in equation (1.18) and rearranging gives a critical aspect ratio for the fiber:

$$\frac{l_c}{d} = s_* = \frac{\sigma_{f*}}{2\tau_{rz*}} \tag{1.19}$$

This equation provides a measure of the bond strength between the fiber and the matrix. For a given fiber strength, s_* (at failure) will increase as the load transfer between the matrix and the fiber (i.e. τ_{rz}) decreases. Also, as the reinforcement aspect ratio decreases the composite will reach a point at which it can no longer reach the strength predicted by equation (1.18). Figure 1.4 illustrates that when $l = l_c$ the average stress in the fiber $\langle \sigma_f \rangle$

is: $$\langle \sigma_f \rangle = \frac{\sigma_f (l_c/2)}{l_c} = \sigma_f/2 \tag{1.20}$$

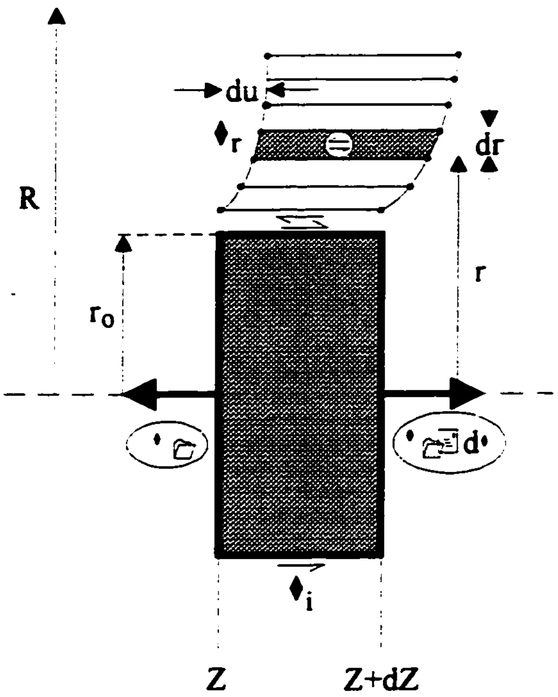

Figure 1.3 Schematic representation of shear lag model, showing variation of stresses with radial position (from Clyne and Withers)[35].

If $l > l_c$ the average fiber stress increases:

$$\langle\sigma_f\rangle = \frac{\sigma_f l - \sigma_f (l_c/2)}{l} = \sigma_f\left(1 - \frac{l_c}{2l}\right) \tag{1.21}$$

Substituting (1.21) into (1.4) provides an expression for the strength of a composite

containing short fibers: $$\sigma_c = f\sigma_f\left(1 - \frac{l_c}{2l}\right) + (1 - f)\sigma_m' \tag{1.22}$$

where σ_m' is the stress acting on the matrix phase when the fibers begin to either plastically deform or fail.

As the weaker fibers fracture load is transferred to the broken fiber segments and the unbroken fibers. As the fibers break the effective aspect ratio (s) decreases, resulting in a noticeable change in the composite stiffness, which can be noted by the change in slope of the stress-strain curve.

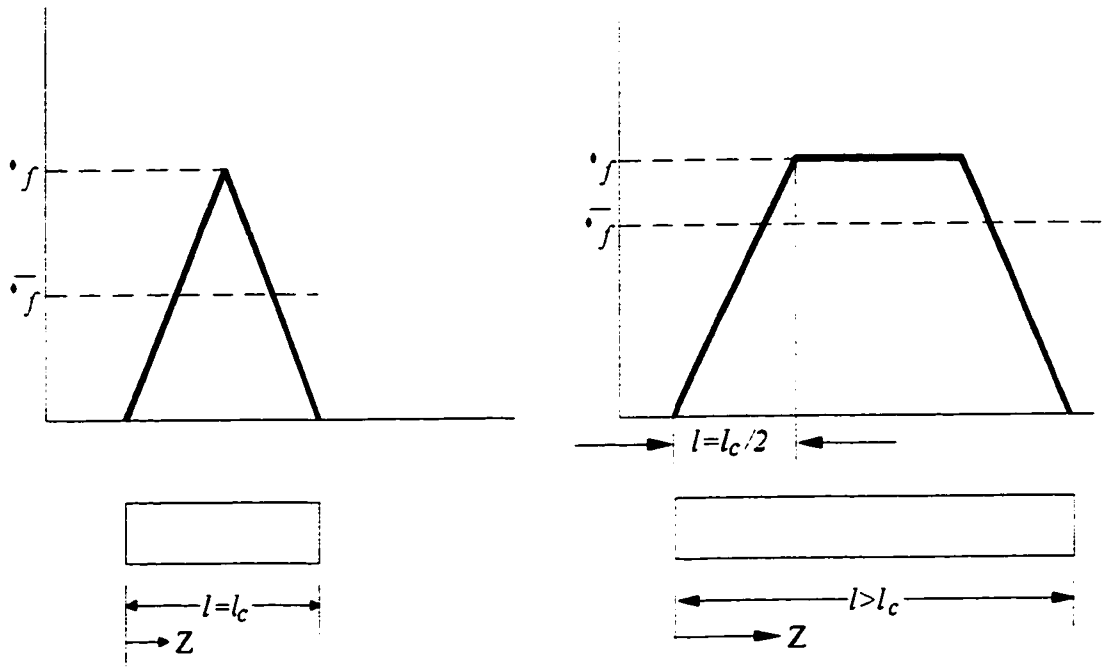

Figure 1.4 Axial stress distribution along fiber length when fiber length is (a) equal to and (b) greater than critical length for reinforcement (from Hertzberg)[36].

The shear lag model has also been modified to include the effect of load transfer on the ends of the fibers[35]. In the modified model, the fiber stress is given by:

$$\sigma_f = \varepsilon_c\left[E_f - \left(E_f - E_m^{\bullet}\right)\cosh\left(\frac{nz}{r_o}\right)\operatorname{sec}h(ns)\right] \tag{1.23}$$

where

$$n = \left[\frac{2E_m}{E_f\left(1+\nu_m\right)\ln(1/f)}\right]^{1/2} \tag{1.24}$$

and

$$E_m^{\bullet} = \frac{E_f\left[1-\operatorname{sec}h(ns)\right]+E_m}{2} \tag{1.25}$$

The fiber radius is r_o, and ε_c is the axial composite strain.

Substituting equation (1.25) into the rule of mixtures estimate for average composite strength (eqn. (1.4)) gives an average fiber stress:

$$\langle \sigma_f \rangle = E_f \varepsilon_c \left[1 - \frac{\left(E_f - E_m^*\right) \tanh(ns)}{E_f ns} \right] \tag{1.26}$$

which may then be used to estimate elastic modulus of the composite:

$$E_{3c} = \left\{ fE_f \left[1 - \frac{\left(E_f - E_m^*\right) \tanh(ns)}{E_f ns} \right] + (1 - f) E_m \right\} \tag{1.27}$$

As the aspect ratio s becomes large, tanh(*ns*)/*ns* becomes small and the elastic modulus approaches that for the continuous fiber composite. An aspect ratio $s = 10/n$ provides a reasonably small value of tanh(*ns*). For most metal matrix composites $n \sim 0.4$, so the aspect ratio necessary to maximize composite strength and stiffness is $s \sim 25$.

Composite failure begins with matrix (or fiber) plasticity or interfacial sliding. Assuming a critical shear stress τ_{i*} and length z = L it can be shown that failure begins at a composite strain of

$$\varepsilon_{c*} = \frac{2\tau_{i*} \coth(ns)}{nE_f} \tag{1.28}$$

which gives an axial composite stress of:

$$\sigma_{3*}^{A} = \frac{2\tau_{i*}}{nE_f} \left\{ \left[fE_f + (1 - f) E_m \right] \coth(ns) - \frac{fE_f}{ns} \right\} \tag{1.29}$$

At this stress either interfacial sliding, fiber fracture or (fiber or matrix) plasticity should begin, with a corresponding change in the slope of the stress-strain curve. This analysis does not include the effect of residual stresses imposed by the thermal contraction that occurs when the composite is fabricated.

Figure 1.5 illustrates peak fiber stresses versus interfacial shear stress, and provides an indication of the expected values of $\tau_{i\bullet}$.

The rule of mixtures and shear lag models both have utility in predicting composite behavior. The rule of mixtures model is best applied to continuous fiber composites with uniaxial loading, and the shear lag model preferred when used with discontinuous aligned fiber composites. While the shear lag model may provide information on matrix-fiber interface strength when combined with experimental evidence (i.e. fiber length as revealed through microscopy), neither model reveals the nature of the residual stress that occur upon cooling. Two models that do provide insight as to the nature of the residual stresses are the coaxial cylinder model for continuous fibers, and the Eshelby method for short fibers.

1.3.3 The Coaxial Cylinder Model

For continuous fiber materials with transverse isotropy, analytical solutions for the elastic stress state may be obtained by treating the composite as a series of coaxial cylinders. It may be used to calculate the stresses resulting from radial and axial loads and temperature change (or both). The method uses the equations of elasticity which are satisfied for the particular boundary conditions; papers have been published with solutions for a four-layer structure with infinite surroundings[37], and for a composite with any number of layers and a free outer surface[38], among others.

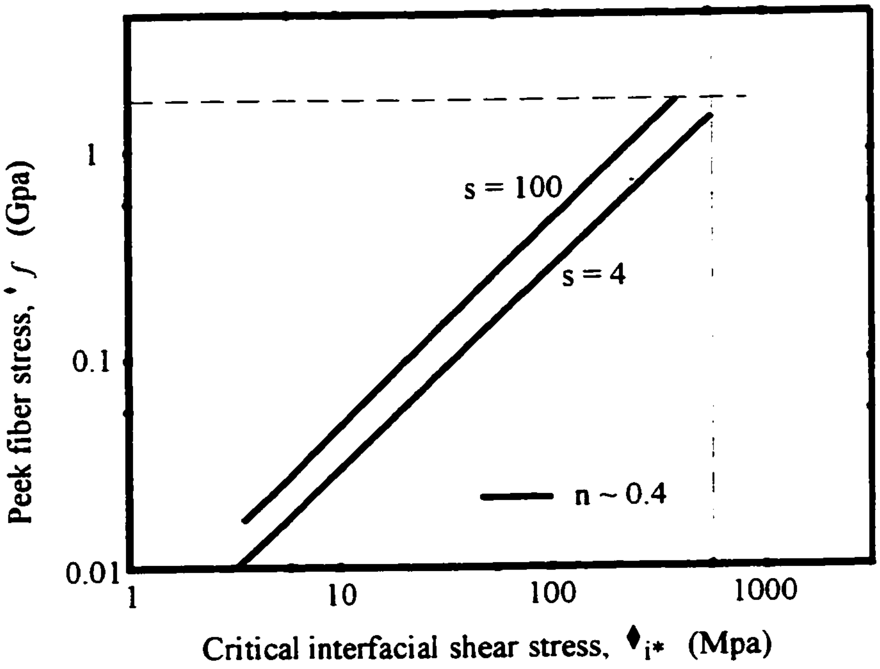

Figure 1.5 Plots of the dependence of peak fiber stress as a function of critical shear stress for the onset of interfacial sliding or (matrix or fiber) yielding (from Clyne and Withers)[35].

Figure 1.6 is a plot of the stress distribution in 30% V_f tungsten fiber composite with a Vitreloy® 1 matrix. The radius of the fiber and matrix are chosen to obtain the proper volume fraction. This figure shows the radial, hoop and axial stress developing in the fiber and matrix resulting from a temperature decrease of 350° C.

The stresses predicted by the model will vary from the actual stresses because the free-surface boundary condition is incorrect for a real composite.. However, the model does provide insight as to the stress state in the composite; there are high shear stresses at the interface in both the axial and hoop components. Also, in this case, the matrix is left with a residual axial stress which will decrease the maximum load which can be sustained. Although Vitreloy® 1 shows no inelastic behavior, other more typical matrix materials, e.g., aluminum and titanium, would likely show plastic flow in these areas first.

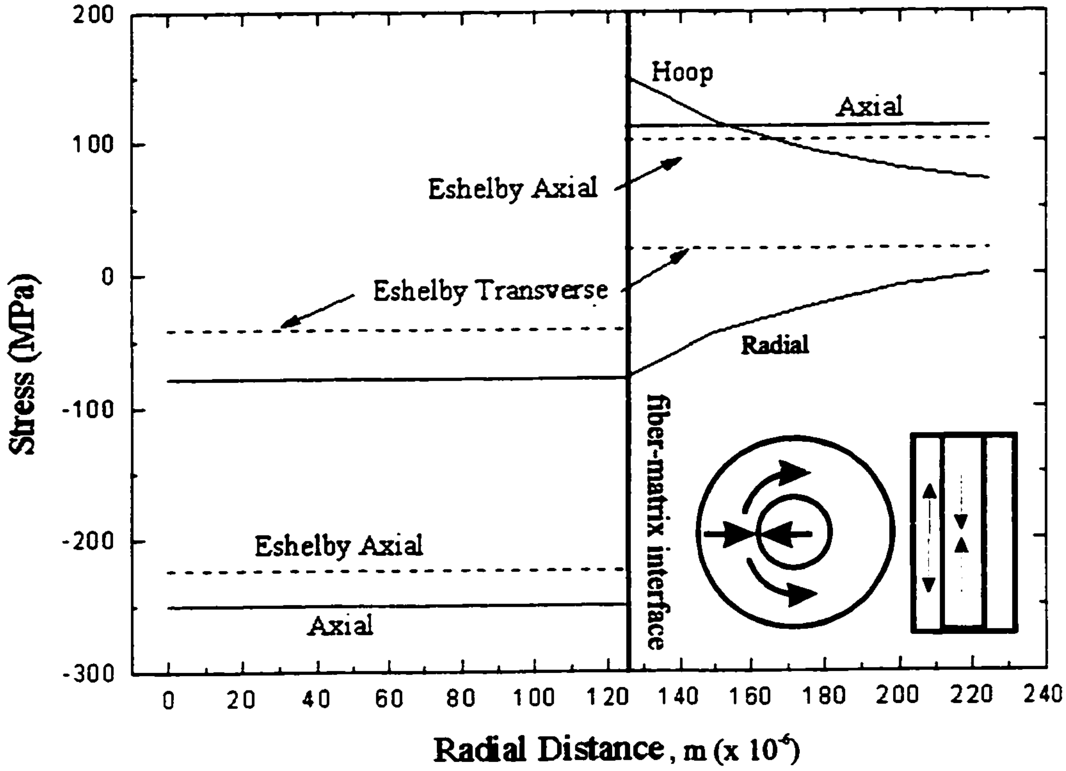

Figure 1.6 Fiber and matrix stress predicted as a result of cooling a 30% V_f tungsten wire/Vitreloy® 1 matrix composite through 350° C. Solid lines represent coaxial cylinder results; dashed lines apply to the Eshelby model.

1.3.4 The Eshelby Model

The Eshelby method is an elegant approach for analyzing the stresses in composites. The technique investigates the internal stresses arising from misfit between reinforcement (particle, fiber, whisker) and the matrix. Although the method may be solved analytically for ellipsoid-shaped particles, numerical solution can be used for other reinforcement shapes. In this method, one imagines that the (ellipsoid) particle is removed from the matrix, and replaced with an (oversized) elliptical particle made of the matrix material that, when inserted into the matrix, gives the same stress fields as did the original particle.

The internal stresses (and strains) generated within a single inclusion as a result of thermal mismatch may be calculated from:

$$\sigma_f = C_m(S-I)\left[(C_f - C_m)S + C_m\right]^{-1} C_f \varepsilon^{t*} \tag{1.30}$$

where ε^{T*} = thermal mismatch strain = $(\alpha_f - \alpha_m)\Delta T$

C_m and C_f are the stiffness matrices of the matrix and fiber, respectively

S is the Eshelby 'S' tensor

The preceding equation applies to thermal mismatch with respect to a single fiber. For modeling a nondilute system allowance must be made for a range of fiber volume fractions, as provided by the following equation, in which thermal mismatch strain is converted to a total transformation strain, ε^t:

$$\varepsilon^t = -\left\{(C_m - C_f)\left[S - f(S - I)\right] - Cm\right\}^{-1} C_f \varepsilon^{t*} \tag{1.31}$$

A similar expression is used to describe the total transformation strain when a load is applied, which produces a corresponding applied strain, ε^A:

$$\varepsilon^t = -\left\{(C_m - C_f)\left[S - f(S - I)\right] - Cm\right\}^{-1} (C_m - C_f)\varepsilon^A \tag{1.32}$$

In the elastic region, equations (1.31) and (1.32) may be summed to obtain the total transformation strain.

Once the total transformation strain is determined, the mean stresses may be calculated:

$$\langle\sigma\rangle_m = -fC_m(S-I)\varepsilon^t \tag{1.33}$$

$$\langle\sigma\rangle_f = (1-f)C_m(S-I)\varepsilon^t \tag{1.34}$$

The mean stress in the matrix and fiber are $\langle\sigma\rangle_m$ and $\langle\sigma\rangle_f$, respectively. The mean internal stress is defined as the difference between the average phase stress and the external stress. When no external stress is applied, e.g., upon cooling, the mean and average internal stress are the same.

Although the Eshelby method was originally developed for elliptical fibers, it has been extended to include particles and long fibers through modifications to the 'S' tensor. Figure 1.6 includes stresses calculated for a 30% V_f tungsten/Vitreloy® 1 composite using this method, for comparison to those calculated using the coaxial cylinder model. The agreement between the models is quite good, particularly in describing the compressive or tensile nature of the stress. It is this quality of the residual stresses that controls the path of crack propagation and the resulting failure behavior of the composite.

BIBLIOGRAPHY

CHAPTER 1

1. Klement, K., Willens, R.H., and Duwez, P., Nature, **187**, 869 (1960).
2. Duwez, P., Trans. AIME, **60**, 606, (1967).
3. Davis, L.A., Metallurgical Transactions A, **10A**, 235, (1979).
4. Chen, H.S., and Wang, T.T., Journal of Applied Physics, **41**, 5338, (1970).
5. Ocelik, V., Diko, P., Hajko, V. Jr., Miskuf, J., and Duhaj, P., Journal of Materials Science, **22**, 2305, (1987).
6. Masumoto, T., and Maddin, R., Materials Science and Engineering, **19**, 1, (1975).
7. Takayama, S., Materials Science and Engineering, **38**, 41, (1979).
8. Chen, H.S., and Turnbull, D., Acta Metallurgica, **17**, 1021, (1969).
9. Pampillo, C.A., Scripta Metallurgica, **6**, 915, (1972).
10. Kimura, H., and Masumoto, T., Amorphous Metallic Alloys, ed. by F.E. Luborsky, Buttersworth, London, 187, (1983).
11. Donovan, P., Acta Metallurgica, **37**, 445, (1989).
12. Peker, A., and Johnson, W.L., Applied Physics Letters, **63**, 2342, (1993).
13. Bruck, H.A., Christman, T., Rosakis, A.J., and Johnson, W.L., Scripta Metallurgica et Materialia, **30**, 429, (1994).
14. Bruck, H.A., Ph.D. Thesis, California Institute of Technology, (1995).
15. He, Y., Schwarz, R.B., Mandrus, D., and Jacobson, L., Journal of Non Crystalline Solids, **207**, 602, (1996).

16. Conner, R.D., Rosakis, A.J., Johnson, W.L., and Owen, D.L., Scripta Metallurgica et Materialia, in press, (1997).

17. Forwood, C.T., Forty, A.J., Philosophical Magazine, **11** [113], 1067, (1965).

18. Donald, I.W., Metcalf, B.L., and Bradley, D.J., Institute of Physics Conference Series no.III, International Symposium on New Materials and their Applications, University of Warwick, (1990).

19. Lee, T.K., and Subramanian, K.N., Journal of Materials Science, **30**, 2401, (1995).

20. Arsenault, R.J. and Taya, M., Acta Metallurgica, **35** [3], 651, (1987).

21. Krstic, V.V., Nicholson, P.S., and Hoagland, R.G., Journal of the American Ceramics Society, **64** [9], 499, (1981).

22. Hasselman, D.P.H., and Fulrath, R.M., Journal of the American Ceramics Society, **48** [10], 548, (1965).

23. Dungan, R.H., Gilbert, J.A., and Smith, J.C., Journal of the American Ceramics Society, Discussions and Notes, **56**, 345, (1973).

24. Dlouhy, I., and Boccaccini, A.R., Composites Sciences and Technology, **56**, 1415, (1996).

25. Baran, G., Degrange, M., Roques-Carmes, C., and Wehbi, D., Journal of Materials Science, **25**, 4211, (1990).

26. Jessen, T.L., Mecholsky, J.J., and Moore, R.H., American Ceramics Society Bulletin, **65** [2], 377, (1986).

27. Troczynski, T.B., Nicholson, P.S., and Rucker, C.E., Journal of the American Ceramics Society, **71** [5], C-276, (1988).

28. Kunz-Douglas, S. Beaumont, P.W.R., and Ashby, M.F., Journal of Materials Science, **15**, 1109, (1980).

29. Leng, Y. and Courtney, T.H., Metallurgical Transactions A, **21A**, 2159, (1990).

30. Vaidya, P.U., and Subramanian, K.N., SAMPE Journal, **29** [4], 26, (1993).

31. Cytron, S.J., Journal of Materials Science Letters, **1**, 211, (1982).

32. Leng, Y., and Courtney, T.H., Journal of Materials Science, **24**, 2006, (1989).

33. Alpas, A.T., and Embury, J.D., Scripta Metallurgica, **22**, 265, (1988).

34. Leng, Y., and Courtney, T.H., Journal of Materials Science, **26**, 588, (1991).

35. Clyne, T.W., and Withers, P.J., An Introduction to Metal Matrix Composites, ed. by A.E. Davis and I.M. Ward, Cambridge University Press, (1993).

36. Hertzberg, R.W., Deformation and Fracture Mechanics of Engineering Materials, 3rd ed., John Wiley & Sons, (1989).

37. Mikata, Y., and Taya, M., Journal of Composite Materials, **19**, 554, (1985).

38. Warwick, C.M., and Clyne, T.W., Journal of Materials Science, **26**, 3817, (1991).

39. Halpin, J.C., and Tsai, S.W., Environmental Factors in Composite Design, Air Force Materials Laboratory, AFML-TR-67-423, (1967).

40. Spencer, A., Composite Science and Technology, **27**, 93, (1986).

41. Nye, J.F., Physical Properties of Crystals - Their Representation by Tensors and Matricies, Clarendon, Oxord, (1985).

42. Clyne, T.W., Journal of Materials Science Letters, **9**, 336, (1990).

43. Bannister, M., Shercliff, H., Bao, G., Zok, F., and Ashby, M.F., Acta Metallurgica, **40** [7], 1531, (1992).

44. Eshelby, J.D., Proceedings of the Royal Society, **A241**, 376, (1957).

45. Eshelby, J.D., Progress in Solid Mechanics, ed. by I.N. Sneddon and R. Hill, 89, (1961).

CHAPTER 2

PARTICULATE MATRIX COMPOSITES

2.1 Introduction

One of the bulk amorphous alloys developed at Caltech has the nominal composition $Zr_{57}Nb_5Al_{10}Cu_{15.4}Ni_{12.6}$; the trade name is Vitreloy® 106. It has mechanical properties common to other metallic glasses, such as high strength (~ 1.8 GPa), high elastic limit (~ 2%), moderate stiffness (85 GPa), and a tendency to fail catastrophically along narrow shear bands. In an effort to increase the toughness of this metallic glass while (hopefully) retaining its desirable mechanical properties, it was combined with particulate reinforcements to make metallic glass matrix/particulate composites. The particles were imagined to interact with the propagating shear band, causing it to slow (or stop) and deflect, thus delaying failure and improving toughness. Ductile metals have been shown to improve the toughness in traditional oxide glasses[1-4].

The properties of Vitreloy® 106 and the various ceramic particles and refractory metals used as reinforcement are listed in Table 2.1.

2.2 Experimental Procedure

Ingots of metallic glass, with a nominal composition of $Zr_{57}Nb_5Al_{10}Cu_{15.4}Ni_{12.6}$, were prepared by arc melting elemental metals in a Ti-gettered argon atmosphere. Metals of the highest available purity were used; the purity ranged from 99.7% for zirconium to 99.999% for copper (metals basis). These metallic glass ingots were combined with the second phase particles by induction melting and mixing on a water cooled copper crucible in a Ti-gettered argon atmosphere. The composite ingots were then induction melted in a

	Young's Modulus (E) (GPa)	Shear Modulus (G) (GPa)	Poisson's Ratio (ν)	Thermal Expansion (α) (10^{-6}/°C)	Nominal Strength MPa
Vitreloy® 106	84.7	30.8	0.376	8.7	1800[2] 1200[3]
Tungsten[17]	411	160	0.280	4.6	$\sigma_y \sim 725$ $\sigma_u \sim 1000$
Tantalum[18]	186	69	0.342	6.5	$\sigma_y \sim 350$
Tungsten carbide[16]	690	278	0.24	4.42	345
Silicon Carbide[16]	411	174	0.185[1]	6.5	35 - 138 at 25°C

[1]Self-bonded [2]Uniaxial Compression [3]Uniaxial Tension

Table 2.1 Properties of Vitreloy® 106 and selected reinforcing particles

quartz crucible and injected into a copper mold using argon at 1 atmosphere pressure. Figure 2.1 is a schematic of the casting apparatus.

The castings were rods 3 mm in diameter and 25 mm long, and dogbone-shaped ingots with the shape and dimensions shown in Figure 2.2. The rods, which were to be used in compression tests, were cut to a nominal length of 6 mm using an Isomet saw equipped with a diamond blade. The cut rods were mounted in a collet holder which was clamped in a V-block, and the ends were lapped flat and square to the axis on SiC wet-dry sand paper, with a final polish using 600 grit. The flatness and perpendicularity of the faces was checked by clamping the polished rod in a micrometer and examining the gap at 40x magnification using a binocular microscope. The dogbone-shaped tensile test ingots were ground in the gage length to the nominal thickness shown in Figure 2.2.

Quasi-static compression and tension tests were performed on an Instron 4204 load frame, at a cross head speed of 0.02 inches per minute. A compression test fixture, as shown in Figure 2.3, was used to insure axial loading. The test specimens were compressed between tungsten carbide platens, the faces of which were lubricated to reduce friction at the ends and prevent the sample from "barreling". The flared ends of the tensile test specimens fit into matching recesses in the tensile grips, which are attached to the Instron machine via universal joints to guarantee axial loading. A calibrated extensometer was used to measure strain in both compression and tensile samples.

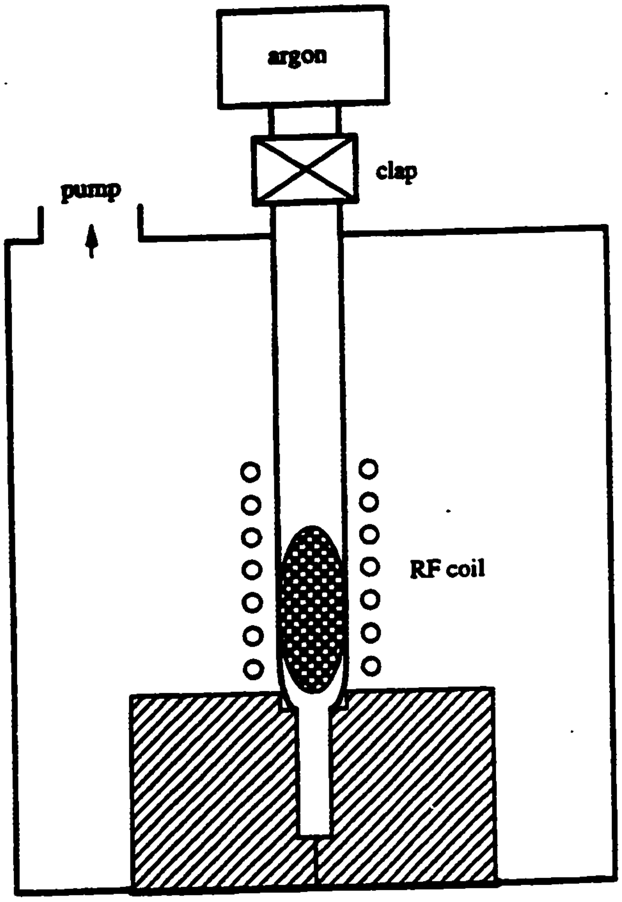

Figure 2.1 Schematic of the mold-casting apparatus.

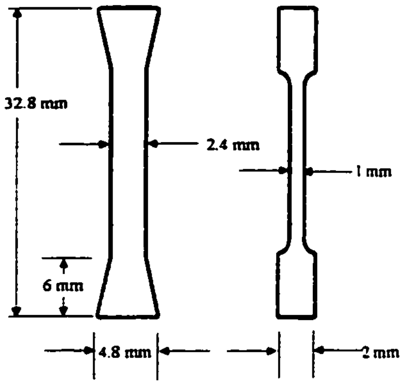

Figure 2.2 Dogbone specimen used for tensile tests

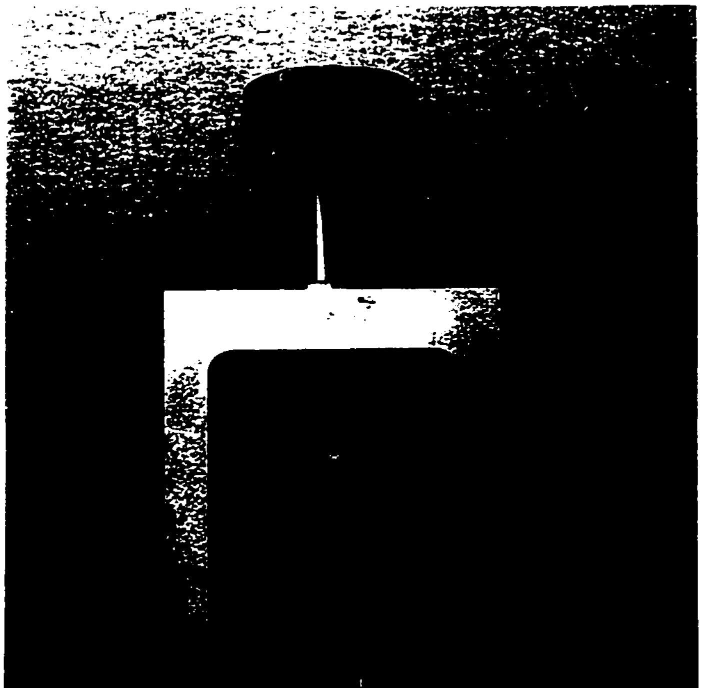

Figure 2.3 Compression test fixture.

The fracture surfaces of the tested samples were examined using scanning electron microscopy (SEM). Light microscopy was used to view general particulate distribution.

The thermal expansion coefficient of Vitreloy® 106 was measured using a Perkin-Elmer Series 7 thermomechanical analyzer. Elastic constants were measured using a Parametrics Model 5052UA ultrasonic analyzer connected to an oscilloscope for data analysis. Density was measured using the hydrostatic weighing technique[5].

2.3 Results and Discussion

2.3.1 Processing

Many particle sizes and volume fractions were fabricated, as shown in Table 2.2. Large particle sizes were more amenable to making high volume fraction (V_f) composites. Fine particles tended to agglomerate and proved to be difficult to wet, thus composites using these reinforcements typically had $V_f < 15\%$.

Figures 2.4a and 2.4b are optical micrographs of a 3 mm Vitreloy® 106/15% V_f WC composite rod, taken at 50X and 400X magnification, respectively. Photograph 2.4a shows an even distribution of the WC phase. This kind of even distribution is typical of that of all the composite samples. More details are visible in Figure 2.4b. There are a few very small pits visible, particularly next to WC particles, although the total porosity in the sample is minimal. The glass phase appears to be uniform, with no obvious crystals. The matrix/particle interface is smooth, indicating a shallow interface layer.

Figure 2.5a is a X-ray diffraction pattern of Vitreloy® 106. It shows the features typical of glass: one large, relatively broad diffraction peak, followed by shallower yet broader second peak. Figure 2.5b is the diffraction pattern of a 5% V_f WC/Vitreloy® 106 matrix composite, with the diffraction pattern of WC superimposed on the same graph. Note that the composite has diffraction peaks in the locations of the WC peaks; outside of

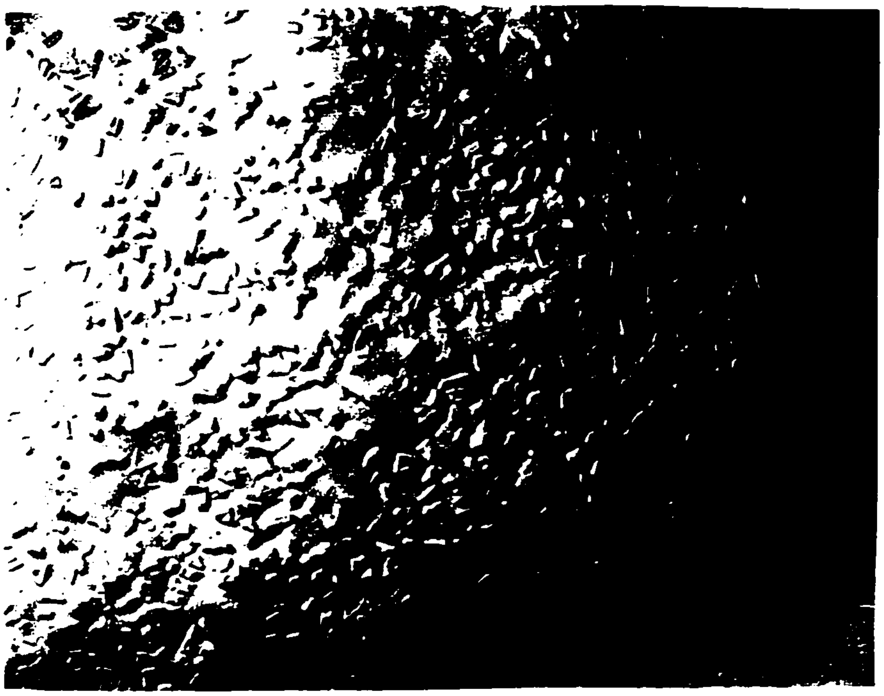

Figure 2.4a Optical micrograph of 15% V_f WC/Vitreloy® 106 composite (50X).

Figure 2.4b Optical micrograph of 15% WC/ Vitreloy® 106 composite. A few small pits are visible, though there is no noticeable reaction layer (400X).

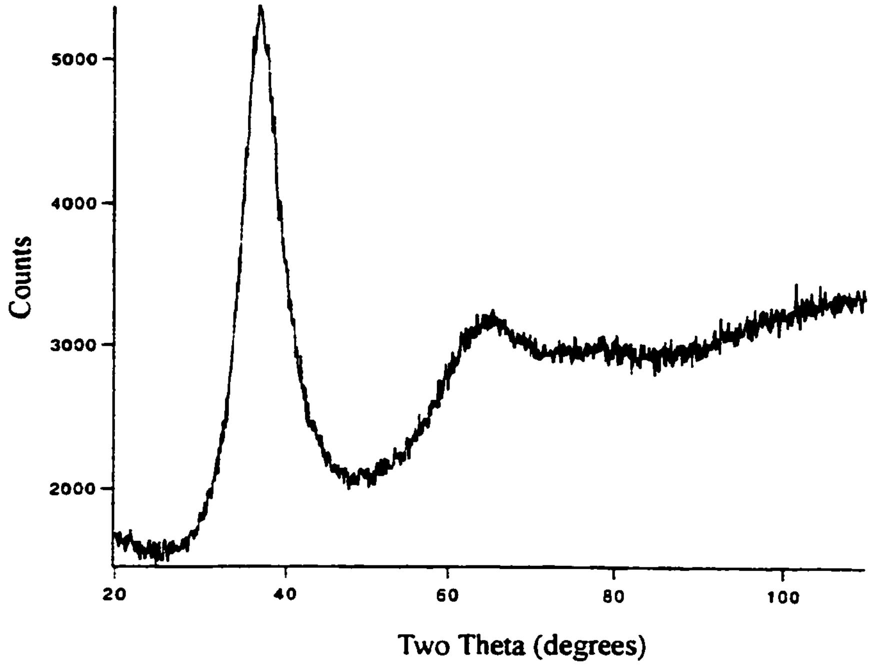

Figure 2.5a X-ray diffraction pattern of Vitreloy® 106.

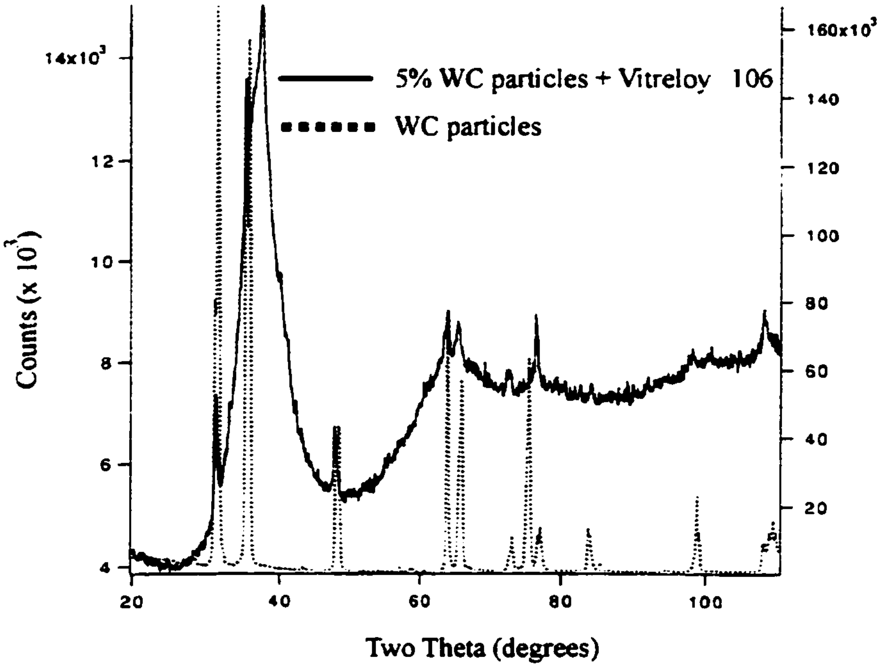

Figure 2.5b X-ray diffraction pattern of WC particles and WC/Vitreloy® 106 composite.

these areas it retains the expected glass diffraction pattern. This indicates that the matrix remains amorphous during processing. X-ray analysis showed that all of the composites tested retained an amorphous matrix.

2.3.2 Elastic Modulus

Elastic modulus of unreinforced Vitreloy® 106 was measured from the slope of the stress-strain curve, Figure 2.6, and also by ultrasonics. The elastic moduli in tension and compression are 83 GPa and 85 GPa, respectively.

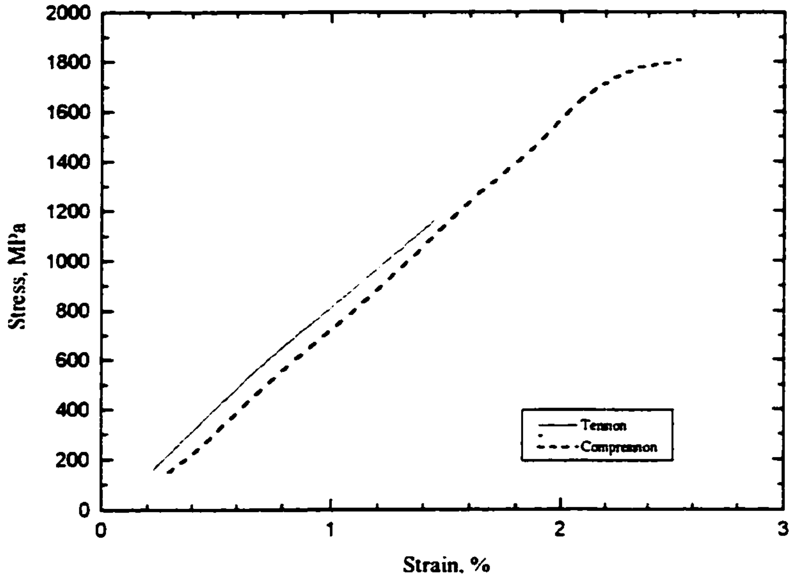

Figure 2.6 Compression and tension stress-strain curves from which the elastic moduli of Vitreloy® 106 were obtained.

In the ultrasonic method dilatation and shear waves (c_L and $c_{S,}$, respectively) are generated by attaching two tranducers to the surface of the sample. The time required for the wave to travel across the specimen and return was recorded on the oscilloscope. Dividing the sample thickness by 1/2 the time gives the corresponding wave speed.

The elastic properties can be calculated from the measured wave speeds and density using the following equations[6]:

$$c_S = \sqrt{\frac{\mu}{\rho}}$$

$$c_L = \sqrt{\frac{\lambda + 2\mu}{\rho}}$$

where μ is the shear modulus (G), λ is Lame's constant, and ρ is the density. The elastic properties are then used to calculate Young's modulus, .$E = \frac{\mu(3\lambda + 2\mu)}{\lambda + \mu}$, and Poisson's ratio, $\nu = \frac{\lambda}{2(\lambda + \mu)}$.

For Vitreloy® 106 metallic glass, $c_S = 2128$ m/s, $c_L = 4769$ m/s, and $\rho = 6.8$ g/cm^3. The elastic properties are:

$$\mu = 30.8 \text{ GPa}$$

$$E = 84.7 \text{ GPa}$$

$$\nu = 0.376$$

and are listed in Table 2.1. The value for elastic modulus as measured by the ultrasonic technique is in good agreement with that obtained from mechanical tests.

The elastic moduli of the composite samples was taken from the slope of the stress-strain curves. Figure 2.7 is a graph of the measured elastic moduli versus those calculated using Eshelby's equivalent inclusion method[7], as described in Chapter 1. The figure shows generally excellent agreement between measurement and theory.

As a second comparison, the measured elastic moduli for tungsten and silicon carbide reinforced particulate composites are plotted in Figure 2.8, along with the Voigt model (or rule of mixtures) as the upper bound, and the Reuss model (for transverse loading) as the lower bound. Silicon carbide is included because it has the same elastic modulus as tungsten. Despite the scatter in the results, the measurements generally fall within these bounds.

There is some variation in Young's modulus at 5% V_f tungsten particles. However, if elastic modulus is dependent upon particle size, this would imply that the moduli fall in ascending or descending order with particle size. This is not the case with

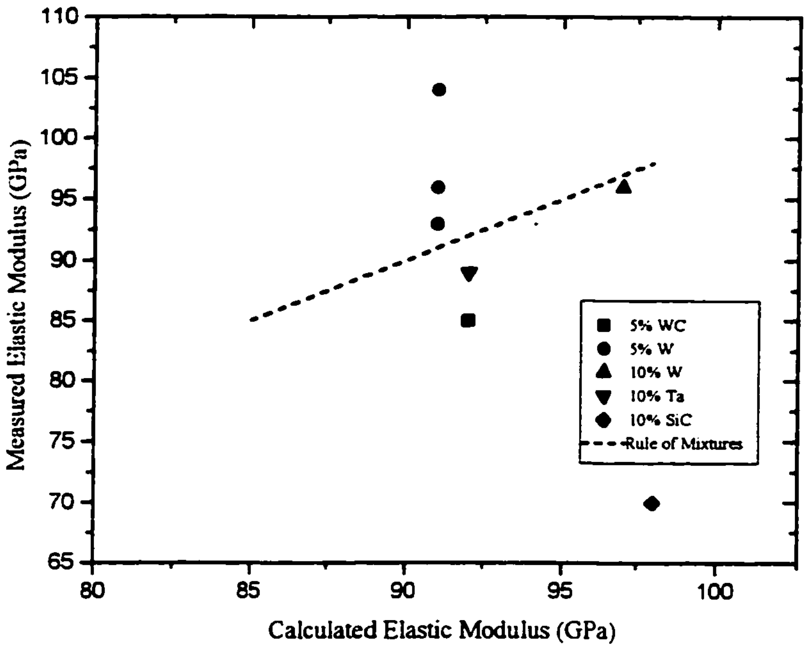

Figure 2.7 Calculated versus measured elastic modulus for Vitreloy® 106 composites

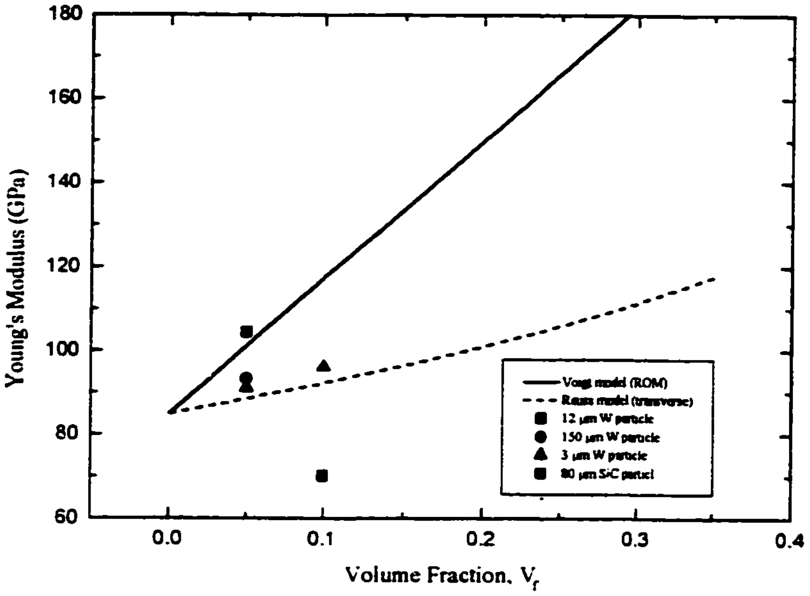

Figure 2.8 Measured elastic moduli plotted with the Voigt model (equal strain) and the Reuss model (equal stress).

the data shown. According to Hasselman and Fulrath, dispersion shape has little or no effect on Young's modulus in a two phase system (when the modulus of the inclusion is greater than that of the matrix)[8]. If one interprets dispersion shape to include size, this is consistent with the results of the Vitreloy® 106/particulate composite system.

2.3.3 Compression Tests

Compression tests were performed on particulate composites containing tungsten, tungsten carbide, tantalum and silicon carbide. As illustrated in Figure 2.6, unreinforced Vitreloy® 106 shows no inelastic deformation in tension, and only ~ 0.5% inelastic deformation in compression. This is in agreement with the work done by Bruck, et al., on Vitreloy® 1, a metallic glass with the composition $Zr_{41.25}Ti_{13.75}Cu_{12.5}Ni_{10}Be_{22.5}$[9]. The results of the compression tests are listed in Table 2.2, along with Δα, the difference in thermal

	$\Delta\alpha$ $(\alpha_p-\alpha_m)$ $\times 10^{-6}/^{\circ}C$	**Particle residual stress (MPa)**	**Matrix residual stress (MPa)**	**Failure stress (GPa)**	**Plastic Strain to failure**
5% WC	-4.28	-182	9.6	1.82-1.92	5%
10% WC	-4.28	-170	18.9	1.96	2.5%
5% W (150 μm)	-4.1	-172	9	1.38	0.5%
10% W (150 μm)	-4.1	-162	18	1.92	8%
15% W (150 μm)	-4.1	-151	26.7	1.86	7%
5% W (3 μm)	-4.1	-172	9	1.75	0
10% W (3 μm)	-4.1	-162	18	1.92	0
10% Ta (20<μm<40)	-2.2	-80	8.9	1.83	3%
10% SiC (37 μm)	-2.2	-81	9	0.6	0
10% SiC (80 μm)	-2.2	-81	9	1.9	0
20% SiC (80 μm)	-2.2	-71	17.8	0.8	0
Vitreloy® 106				1.82	~ 0 - 0.5%

Table 2.2 The difference in thermal expansion $(\alpha_p-\alpha_m)$, calculated average particle and matrix stress, and measured compressive failure stress and plastic strain to failure for Vitreloy® 106/particulate composites.

expansion between the particle and the matrix (α_p-α_m), and the average residual stresses, calculated using the Eshelby equivalent inclusion method. The thermal strain, $\varepsilon_T = \Delta\alpha\Delta T$, was computed assuming the temperature change, $\Delta T = -400$ °C. This is approximately the difference between the measured glass transition temperature[10], $T_g = 420$ °C and room temperature, $T \sim 20$ °C.

The difference in thermal expansion, $\Delta\alpha$, is negative in all the composites tested. This has the effect of placing the particle in compression, and the matrix in tension. As a result of the residual tensile matrix stresses, cracks are directed toward the particles. The particles then act to retard crack (or shear band) propagation.

The strength of the metallic glass composites was essentially the same as that of the unreinforced metallic glass. The ultimate strength of Vitreloy® 106 in compression tests is 1.82 GPa, while that of the strongest composite sample was 1.96 GPa, an increase of just over 7%. The matrix is under a residual tensile stress in the composites; for this 10% WC sample, the residual tensile stress is 18.9 MPa (as calculated using Eshelby's equivalent inclusion method), or about 1% the compressive strength of the unreinforced metallic glass. This tensile stress would have to be overcome before actual compression of the matrix would take place, but cannot, in itself, account for the increase in compressive strength of the composite. Also, theory does not support the contention that residual stresses cause a difference in tensile and compressive strength in *particulate* composites. Whether this small difference is the result of the inclusion, or just scatter in the experimental results would require more study to determine.

Substantial inelasticity was shown by samples made from W, WC and Ta. Of these, W showed the greatest amount of (perfectly) plastic behavior (~ 7%). Tantalum and WC showed comparable amounts (~ 3%, Figure 2.9). The compression samples made from SiC particles and 3 μm W particles showed no plastic behavior (Figure 2.10).

It is notable that the samples reinforced with W had similar strength regardless of particle size; 10% V_f W made with 150 μm particles had a (compressive) strength of 1.92 GPa, the same as that of samples with the same volume fraction of W reinforcement made from 3 μm particles. This is consistent with the findings of Troczynski, et al., who found strength of Al reinforced soda-lime-glass in bending to be independent of inclusion size[11].

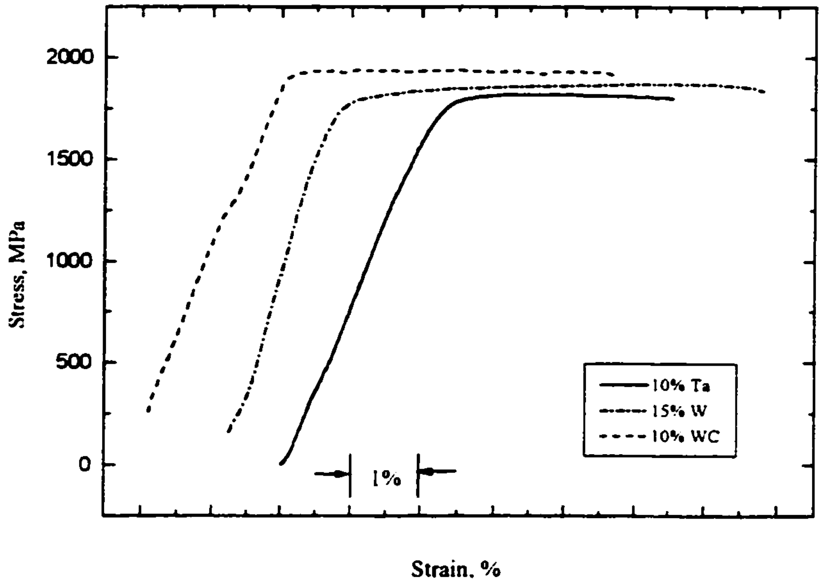

Figure 2.9 Quasi-static compression tests on Vitreloy® 106 composites reinforced with Ta, W, and WC. A 15% V_f W provided the greatest strain to failure.

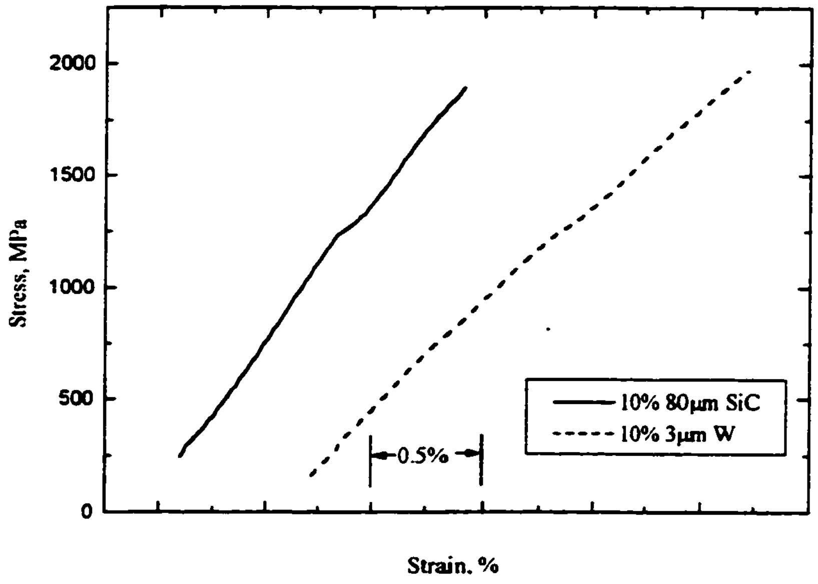

Figure 2.10 Quasi-static compression of Vitreloy® 106 composites reinforced with SiC and 3 μm W particles. These show no inelastic deformation.

The toughening of brittle materials with the addition of ductile particles is generally attributed to the particle applying a closure traction to the advancing crack front, or to crack deflection[12]. In compression, however, there is no crack opening. The toughening in the metallic glass systems in compression is because the particles resist shear loading, and hence retard shear band propagation in the material. Because the matrix experiences an average tensile stress when $\alpha_p<\alpha_m$, cracks (or shear bands) are directed toward the particles. As the load on the specimen increases, shear bands form and begin to propagate, until encountering a shear resistant particle. The stresses, which are relieved during shear band propagation, begin to build up again, generating additional shear bands in the sample. Multiple shear band formation in a compression sample can be seen in

Figure 2.11, an SEM photograph of the side of a WC compression sample. Eventually the particle will fail, and the shear band will continue to propagate.

This behavior of the shear band slowing when encountering a particle, followed by fast fracture when overcoming the obstacle, is visible in Figure 2.12, an SEM photograph of a W inclusion surrounded by a metallic glass matrix. Much has been written regarding the "veinous" pattern in the fracture surface of a metallic glass[13]. In the photograph, one can see clearly that the flow is from upper left to lower right; the particle is partially covered with the metallic glass, which appears to have flowed as a very viscous liquid across a portion of the particle when the shear band reinitiated. The area to the upper left, which is characterized by a the veinous dimples, is the area where the shear band would be

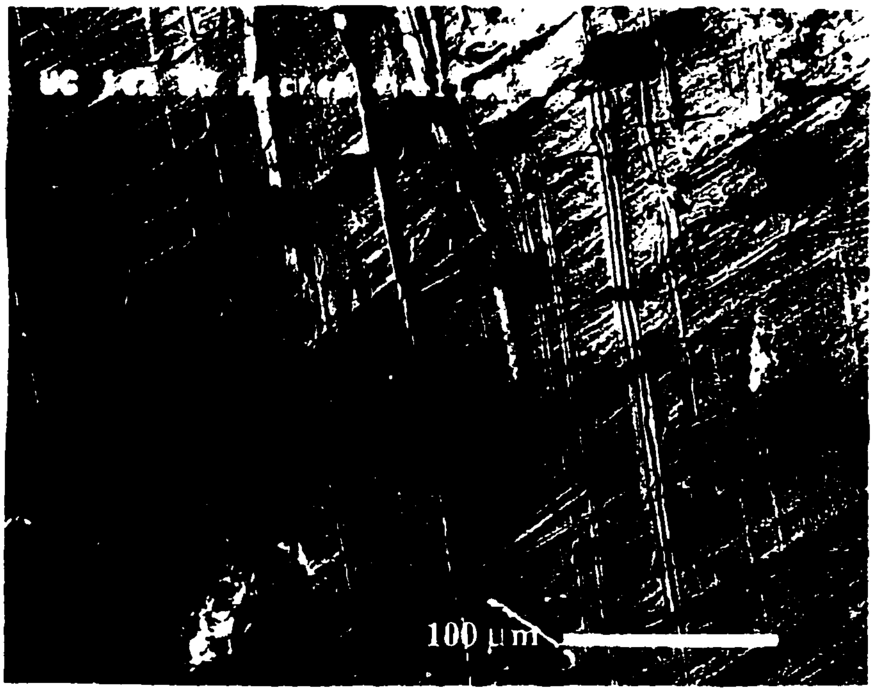

Figure 2.11 Multiple shear band formation in a WC/Vitreloy® 106 composite compression sample.

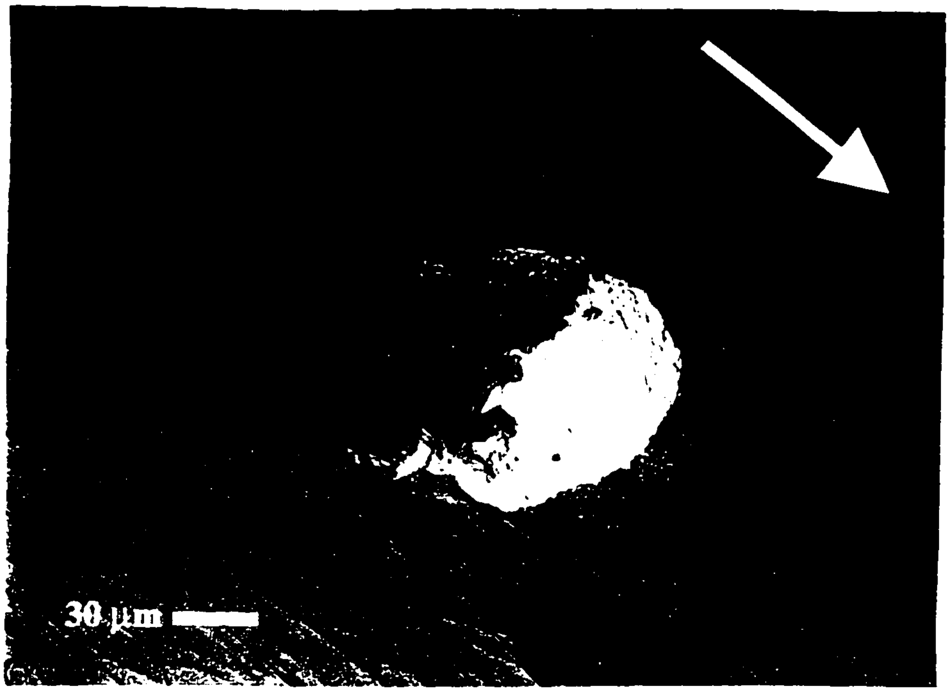

Figure 2.12 Fracture surface of a W/Vitreloy® 106 composite compression sample. Arrow indicates direction of shear band propagation.

most impeded. The area to the sides and in front of the particle are smooth; this is interpreted as an area of fast fracture, when the shear band over comes the impediment of the particle. This is consistent with the findings of Fortwood and Forty, who studied the interaction of cleavage cracks with inhomogeneities in NaCl crystals[14].

Examination of Figure 2.12 also reveals that the W failed in a brittle manner: the surface shows no microvoids or other evidence of ductile fracture. In the composite the particle is in a state of residual compression, and highly constrained by the matrix. Particles tend to fracture rather than deform because of this constraint. As can be seen in Figure 2.13, the compression samples eventually fail along shear bands oriented at 45 degrees to the axial loading direction.

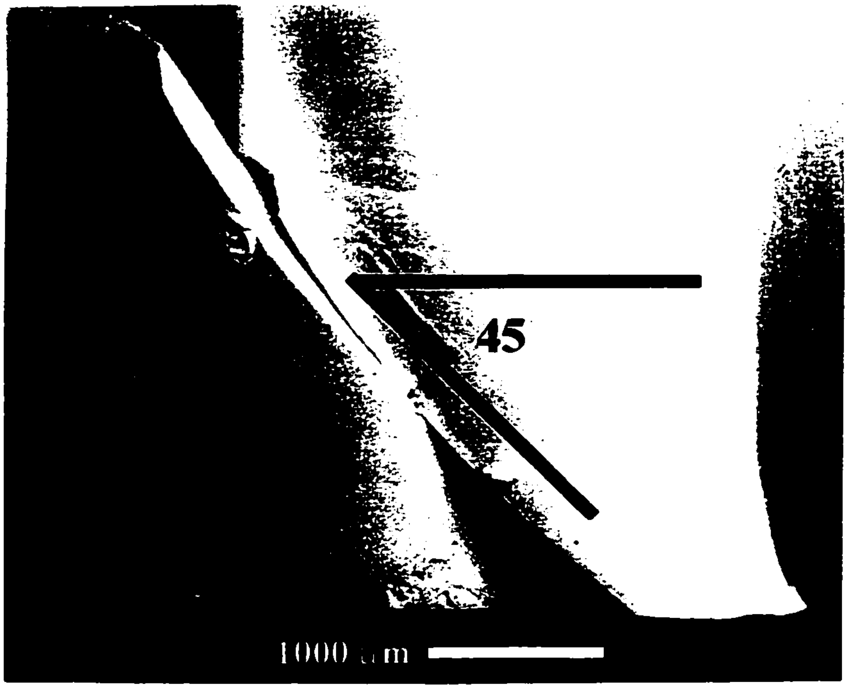

Figure 2.13 Vitreloy® 106 compression sample, which shows the 45 degree shear band failure typical of metallic glass.

2.3.4 Tensile Tests

Tensile tests were performed on dogbone-shaped specimens as shown in Figure 2.2. Strain was measured using a calibrated extensometer. As may be seen in Figure 2.6, the unreinforced Vitreloy® 106 tested had a tensile strength of 1.2 GPa, which is 33% less than the compressive strength. This difference indicates that the yield behavior of Vitreloy® 106 is anisotropic.

Tensile tests were performed on composites of Vitreloy® 106 and tungsten, tungsten carbide and silicon carbide. The quasi-static tensile stress-strain curves are shown in Figures 2.14 and 2.15. The stress-strain curves for the W composite samples show noticeable nonlinearity when compared to the essentially linear behavior of unreinforced Vitreloy® 106. The nonlinearity of the samples reinforced with WC and SiC is not as pronounced.

The strength of the composites reinforced with W is greater than that of unreinforced Vitreloy® 106, while the strength of composites containing WC and SiC is less. However, because there is considerable scatter in the mechanical behavior of metal matrix composites, it is premature to draw any conclusions. From simple strength models, e.g., the rule of mixtures,

$$\sigma_c = f\sigma_p + (1 - f)\sigma_m$$

one would expect the strength of composites using WC and SiC to be less than the unreinforced matrix. The yield strength of W is substantially higher than that of the

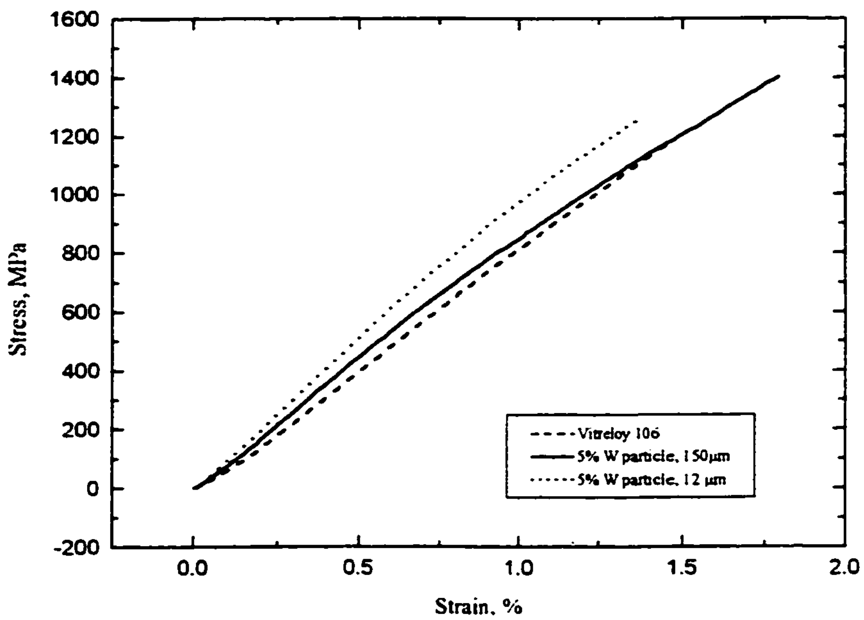

Figure 2.14 Quasi-static tensile stress curves for Vitreloy® 106 and W/ Vitreloy® 106 composites.

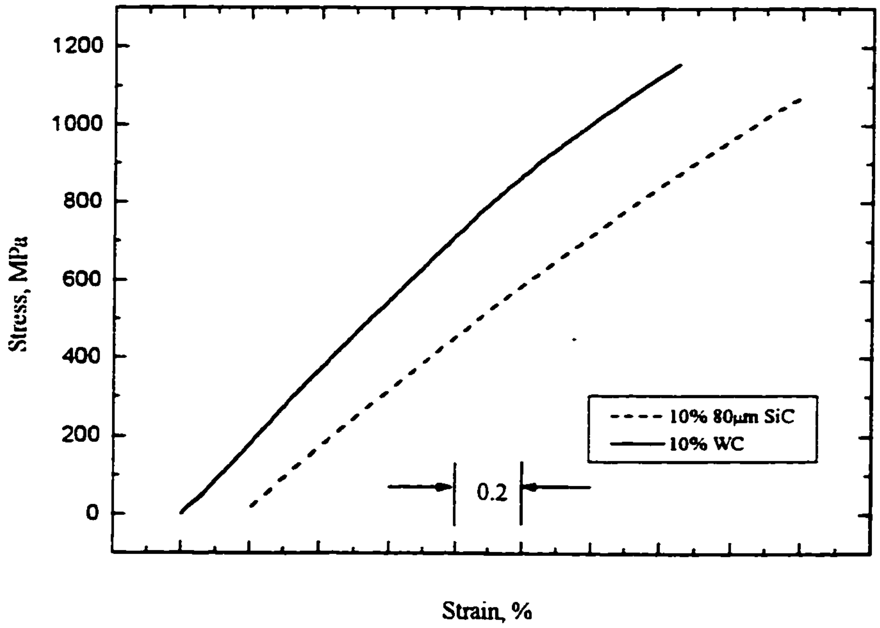

Figure 2.15 Quasi-static tensile stress curves for Vitreloy® 106 reinforced with SiC and WC.

ceramic particles, and the constraint imposed by the matrix on the particle due to residual thermal stress delays the onset of plastic deformation of the particle.

The energy per unit volume required to cause material failure may be determined by integrating the stress-strain curve:

$$\frac{J}{m^3} = \int \sigma(\varepsilon)d\varepsilon$$

Numerical integration of the tensile stress-strain curves gives an specific energy for failure of Vitreloy® 106 of 873 MJ/m^3. The specific energy for failure of the composite reinforced with 5% W (150 μm particles) is 1329 MJ/m^3, an increase of 52%. The ceramic particle reinforcements did not provide any significant increase in toughness.

Silicon carbide reinforced metallic glass showed an increase in area under the stress/strain curve of 5%, while the WC composite was substantially less.

Figure 2.16 is an SEM photograph of the unreinforced Vitreloy® 106 tensile test specimen. Although the fracture surface undulates some, and is not perfectly shear, it does propagate at the ~ 45 degree angle typical of metallic glass. The fracture surface along the lower right edge is shown in figure 2.17. It is relatively smooth along the edge, becoming more veinous as it propagates inward, then followed by another smooth area. This seems to be the pattern in metallic glass fracture surfaces: areas of fast fracture, characterized by a relatively smooth surface, connected by areas of slower crack growth, indicated by a heavier veinous pattern. This fast/slow, smooth/rough pattern repeats itself across the fracture surface.

Now examine Figure 2.18, an SEM photograph of the fracture surface of a 5% W reinforced tensile specimen. It is characterized by what appear to be shear lips on both edges of the sample, where the shear band undergoes a sharp change in direction. Shear lips are never present on unreinforced metallic glass. The center section on the left hand side of the sample appears flat and smooth, but the right hand side is very coarse, with many protrusions. Figure 2.19 is a micrograph of the shear lip at the bottom right of the specimen, where the crack changes direction. In other (i.e. oxide) glasses, fracture initiation is characterized by a very smooth, shiny mirror area, which transitions to areas of increased roughness, called mist and hackle[19]. If this fracture behavior is assumed in metallic glass, then the fracture begins in the smooth central region of the composite tensile sample, with the area in the shear lips being the last to fracture.

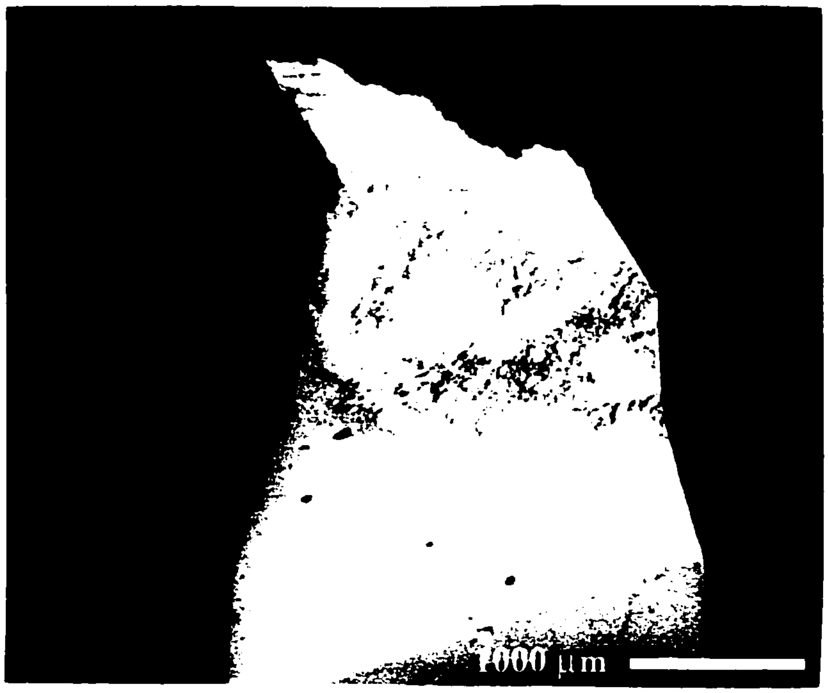

Figure 2.16 Tensile fracture surface of unreinforced Vitreloy® 106.

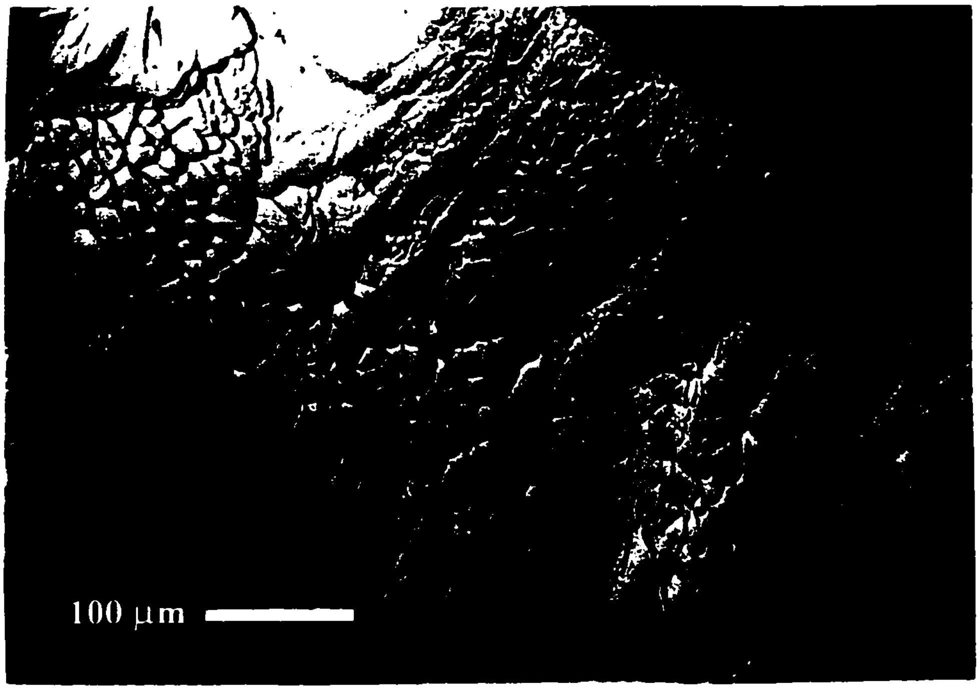

Figure 2.17 Close up of tensile fracture surface of Vitreloy® 106 sample shown in figure 2.16.

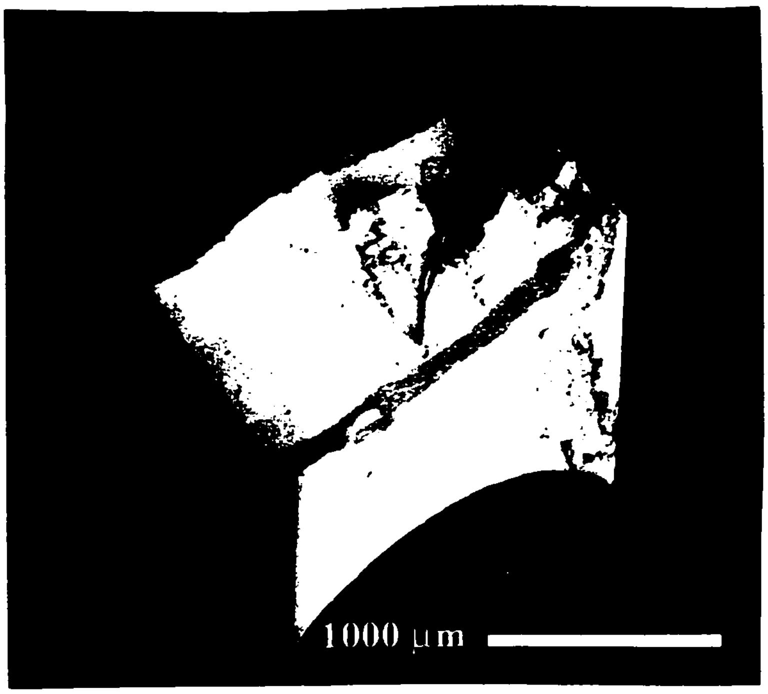

Figure 2.18 Tensile fracture surface of 5% V_f W/Vitreloy® 106 composite.

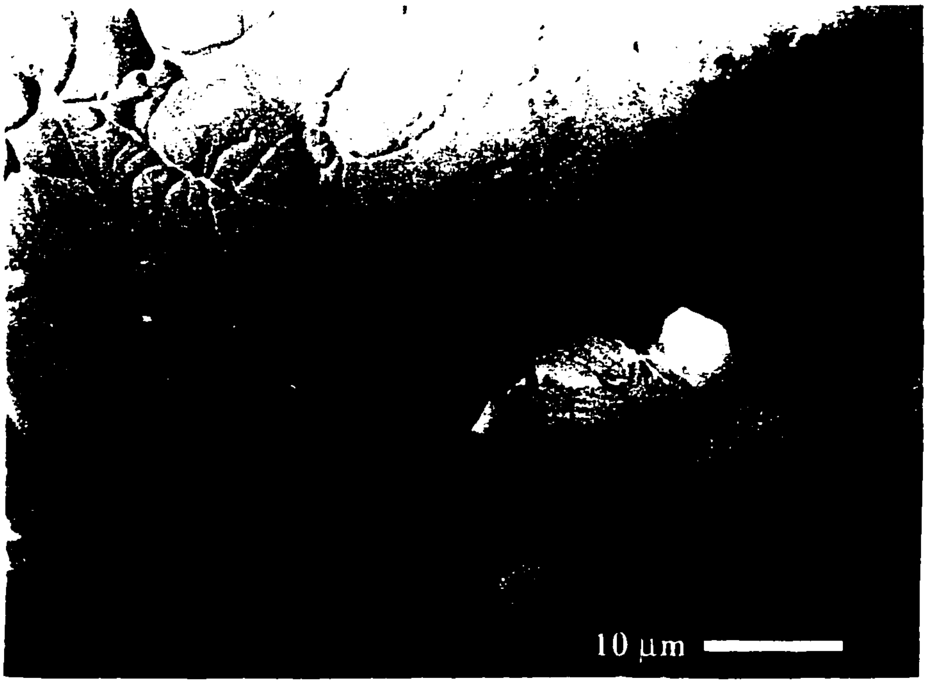

Figure 2.19 SEM photograph of area around shear lip of 5% V_f W/ Vitreloy® 106 tensile sample in figure 2.18. Note the fractured W particle in the shear lip.

The crack bisected the W particles. The particles appear to have fractured, because their fracture surfaces look flat, as if the result of cleavage, rather than ductile failure by microvoid coalescence. It appears that the particles slowed initial crack propagation. Figure 2.20 is a SEM micrograph taken from the rough section in the right center of the sample; Figure 2.21 is the same area at higher magnification. The particles in this area either pulled out, as can be seen by some of the dimples in Figure 2.20, or were retained in the matrix and fractured, as is visible in Figure 2.21. The fracture appears to have progressed from right to left in the photograph, judging by the way the metallic glass matrix covers some of the particles in the lower right hand portion of Figure 2.21.

The toughening in this case is attributed to two factors: the restriction the particles place on the propagating shear band, causing it to slow and change direction, and also increase in the surface area over which the fracture occurs. In their paper on the fracture behavior of laminated metal-metallic glass composites, Leng and Courtney describe two factors that explain toughening in these systems[15]. First, that the critical stress for shear band formation in the composite is larger than the monolithic glass because the particle/matrix interaction provides an additional restraint to shear band deformation. Second, that, if the shear stress remains constant and equal to that of the monolithic glass, the energy increment required to fracture a composite, due to the additional surface area, is on the order of 50 percent higher than that of the monolithic glass. This value is consistent with the results of the tensile experiment.

Figure 2.20 Rough section of fracture surface in 5% W/ Vitreloy® 106 tensile sample shown in Figure 18. Note that particles either pull out or fracture.

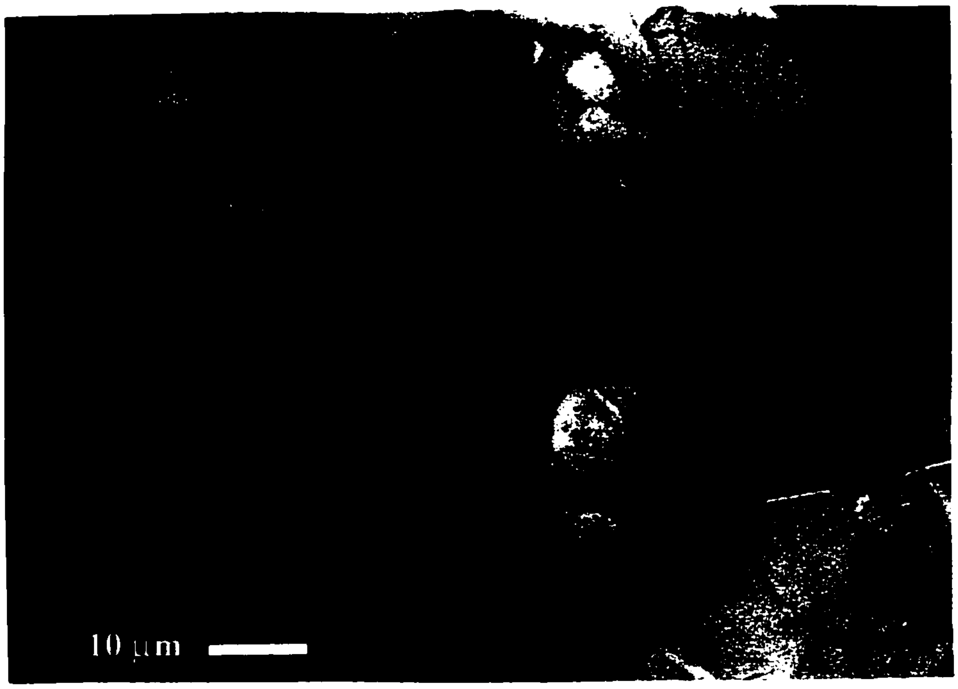

Figure 2.21 Higher magnification SEM photograph of Figure 2.20. Particles show no ductile failure behavior.

2.4 Conclusions

1. Composites using ceramic and refractory (ductile) metal particles and having a metallic glass matrix can be fabricated successfully.
2. The matrix remains glassy with processing.
3. The elastic modulus of the composites falls within the values predicted by theory.
4. The compressive strength of the composite samples is approximately the same as that of the unreinforced metallic glass.
5. The addition of ductile particles increases the strain to failure of compression samples. The large plastic strain results from the formation of numerous shear bands.
6. The tensile strength of unreinforced Vitreloy® 106 and composites using it as the matrix material is approximately 2/3 of the compressive strength.
7. Ductile particles increase the toughness of the metallic glass in tension by obstructing shear band propagation, and by generating additional fracture surface area.

2.5 Acknowledgments

I would like to thank Haein Choi-Yim for her contribution to this investigation. She prepared the metallic glass composite samples used in these tests, and performed the x-ray analysis and the microscopy.

Bibliography

Chapter 2

1. Green, D.J., Nicholson, P.S., and Embury, D.J., Journal of Materials Science, **14**, 1413, (1979).
2. Krstic, V.V, Nicholson, P.S., and Hoagland, R.G., Journal of the American Ceramic Society, **64** [9], 499, (1981).
3. Baran, G., Degrange, M., Roques-Carmes, C., and Wehbi, D., Journal of Materials Science, **25**, 4211, (1990).
4. Vaidya, R.U., and Subramanian, K.N., SAMPE Journal, **29** [4], 26, (1993).
5. Lin, X. and Choi-Yim, H., unpublished results.
6. Malvern, L.E., Introduction to the Mechanics of a Continuous Medium, Prentice-Hall Inc., Englewood Cliffs, N.J. (1969).
7. Warwick, C.M., and Clyne, T.W., Journal of Materials Science, **26**, 3817, (1991).
8. Hasselman, D.P.H., and Fulrath, R.M., Journal of the American Ceramics Society, **48** [10], 548, (1965).
9. Bruck, H.A., Ph.D. Thesis, California Institute of Technology, (1995).
10. Lin, X., Ph.D. Thesis, California Institute of Technology, (1997).
11. Troczynski, T.B., Nicholson, P.S., and Rucker, C.E., Journal of the American Ceramics Society, **71** [5], C-276, (1988).
12. Sigl, L.S., Mataga, P.A., Dalgleish, B.J., McMeeking, R.M., and Evans, A.G., Acta Metallurgica, **36** [4], 945, (1988).
13. Pampillo, C.A., and Reimschuessel, A.C., Journal of Materials Science, **9**, 718, (1974).

14. Forwood, C.T., Forty, A.J., Philosophical Magazine, **11** [113], 1067, (1965).

15. Leng, Y. and Courtney, T.H., Metallurgical Transactions A, **21A**, 2159, (1990).

16. Shackelord, J. and Alexander, W., eds., The CRC Materials Science and Engineering Handbook, CRC Press, Boca Raton, FL., (1992).

17. Miner, D.F., and Seastone, J.B., eds., Handbook of Engineering Materials. 1st ed., John Wiley & Sons, N.Y., (1995).

18. Boyer, H.E. and Gall, T.L., eds., Metals Handbook, Desk Edition, American Society for Metals, Metals Park, Ohio, (1985).

19. Mecholsky, J.J., Jr., and Powell, S.R., Jr., eds., Fractography of ceramic and Metal Failures, ASTM STP 827, 7, Philadelphia, (1982).

CHAPTER 3

CONTINUOUS FIBER COMPOSITES

3.1 Introduction

In 1993 a class of bulk glass forming metals was developed at Caltech by Peker and Johnson[1]. These alloys may be fabricated with minimum dimensions in centimeters, which allows valid mechanical tests to be performed on these materials. Some basic physical and mechanical properties have been measured on a specific beryllium bearing bulk metallic glass with a nominal composition of $Zr_{41.25}Ti_{13.75}Cu_{12.5}Ni_{10}Be_{22.5}$[2,3]. The properties physical properties of this bulk metallic glass, which has the trademarked name Vitreloy® 1, are listed in Table 3.1.

Despite the remarkable properties of bulk metallic glasses such as Vitreloy® 1, all metallic glasses fail by localized shear bands which lead to catastrophic failure. Early studies on metallic glasses showed that samples which are in a state of plane stress fail on one dominate shear band[4] and showed little macroscopic inelastic behavior while those in constrained geometries fail with multiple shear bands in an elastic-perfectly plastic manner[5].

Various researchers reported the feasibility of making metallic glass reinforced composites, which would result in improved mechanical properties and high structural efficiency and cost effectiveness[6]. Vaidya, et al., demonstrated that metallic glass ribbons could be incorporated in an oxide glass matrix to improve the toughness of the matrix via fiber debonding, pullout and fracture[7]. Leng and Courtney[8-10] have done extensive work combining metallic glass ribbons (e.g. $Ni_{91}B_2Si_7$) with ductile metals (e.g. brass) in layered composites. They have found that the constraint imposed by the ductile metal allowed for the formation of multiple shear bands in the metallic glass, which promoted stable crack growth and extended strain to failure of the composite. Thus it was demonstrated that metallic glass ribbons could be incorporated as the reinforcement in a ductile metal matrix to obtain a composite with enhanced properties.

This leads to the work reported in this chapter. If the properties of metallic glass ribbons can be improved by incorporation in ductile metal matrix, can ductile metal fibers be used to increase the toughness of a bulk metallic glass? In this chapter I report the result of our efforts to fabricate continuous ductile fibers into a metallic glass matrix of Vitreloy® 1.

Two kinds of metal fibers were chosen in this effort: tungsten and 1080 steel (music) wire. Initially a large number of materials were evaluated, including Ni, carbon fibers, SiC, Ta, Cu, W and steel. Tungsten was chosen because of its high melting temperature; at the processing temperature it showed no adverse reactivity with the metallic glass matrix. It also has a coefficient of thermal expansion (CTE) of $4.5 \times 10^{-6}/°C$, significantly lower than that of the glass, which is nominally $8.5 \times 10^{-6}/°C$. Steel was chosen because it also seemed little affected by the processing and did not promote extensive crystallization of the matrix. The $13 \times 10^{-6}/°C$ CTE of steel provided a nice contrast to the very low CTE of tungsten. The remaining reinforcement materials were not used for one of two reasons: either they reacted significantly with the matrix material, or they did not wet well enough to make samples with good mechanical integrity.

Property	Vitreloy® 1	Tungsten	Music Wire
Young's Modulus GPA	96	410	207
Shear Modulus GPA	34.3	160.5	77.9
Poisson's ratio	0.36	0.28	0.29
Tensile yield strength, MPa	1900	1600	2100
Tensile strain to failure	2%	2%	1.7
Plane strain fracture toughness, K_{IC}, $MPa\sqrt{m}$	55	12-14	20-28
Hardness (Vickers) kg/mm^2	534	~650	~670
Thermal expansion coefficient, x $10^{-6}/°C$	8.5	4.5	13
Density (g/cm^3)	6.1	19.3	7.9

Table 3.1 Physical properties of Vitreloy® 1 and the selected reinforcements, tungsten and 1080 steel (music) wire.

3.2 Composite Sample Preparation

The focus of this study was continuous-fiber, ductile-metal reinforced composites. The wires were 254 μm diameter tungsten and 1080 steel (music) wire. The matrix material was a bulk metallic glass with the composition $Zr_{41.25}Ti_{13.75}Cu_{12.5}Ni_{10}Be_{22.5}$; this alloy has the trade name Vitreloy® 1.

We first prepared ingots of Vitreloy® 1 by combining the constitutive elements in an induction furnace under a titanium-gettered argon atmosphere. The starting metals were high-purity (99.5% metals basis or better) research grade material.

The wire was straightened and cut to 5 cm lengths. The tungsten was ultrasonically cleaned in acetone, followed by ethanol. A 50/50 solution of phosphoric acid and water was used to remove surface rust from the music wire, followed by ultrasonic cleaning.

The composite samples were cast in the apparatus shown by the schematic in Figure 3.1. The reinforcement material was placed in the sealed end of a 7 mm i.d. quartz-glass tube. A neck was formed in the tube about 1 cm above the reinforcement, and then ingots of the matrix material were inserted into the tube. The constriction helped to minimize premature contact and thus excessive reaction between the melt and the reinforcement. The open end of the quartz tube was then connected to a three-way switching valve; the tube could thus be evacuated with a roughing pump or pressurized with argon.

Prior to processing, the tube was evacuated and then purged with argon; this cycle was repeated several (~ 4) times. Following the final purging process, the tube was evacuated for a minimum of one hour in an effort to remove any trapped gas.

The sample tube was heated in a resistive tube furnace with temperature feedback control. The initial heating stage was at 1228 K+/- 20 K. The variation in temperature comes primarily from the temperature profile in the furnace. The sample was held at this temperature for 15 minutes. The temperature was then lowered to 1078 K +/- 5 K. When the furnace reached this target temperature, a positive pressure of 207 kPa argon was applied above the melt. These conditions were held for 30 minutes to allow infiltration of the molten matrix material into the reinforcement. Then the sample was quickly removed from the furnace and quenched in brine (8 wt% NaCl/H_2O solution).

Samples were made with volume fractions of fibers of 10, 15, 20, 40, 60, and 80%. The castings were cut to length (~ 5 cm) then centerless ground to the desired diameter

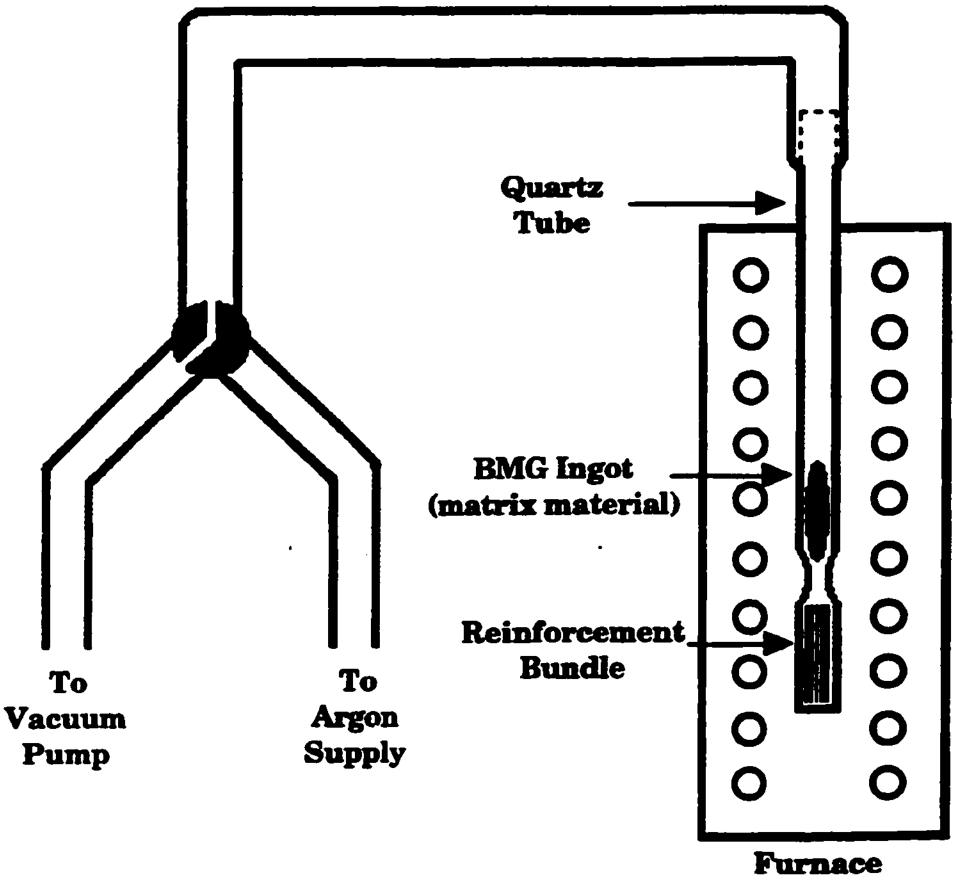

Figure 3.1 Schematic of the apparatus used to cast Vitreloy® 1 matrix composites.

(nominally 6.25 mm). Compression samples were cut to a length that provided an aspect ratio of 1.5 to 2. Each compression specimen was mounted in a collet holder which was clamped into a V-block, and the ends were ground flat and perpendicular to the loading axis. The final lapping was done using 600 grit SiC wet-dry sand paper. A gage length of ~20 mm length and 3 mm diameter was ground into each tensile specimen, along with the threads on each end. Figure 3.2 is a photograph of the as prepared compression and tension samples.

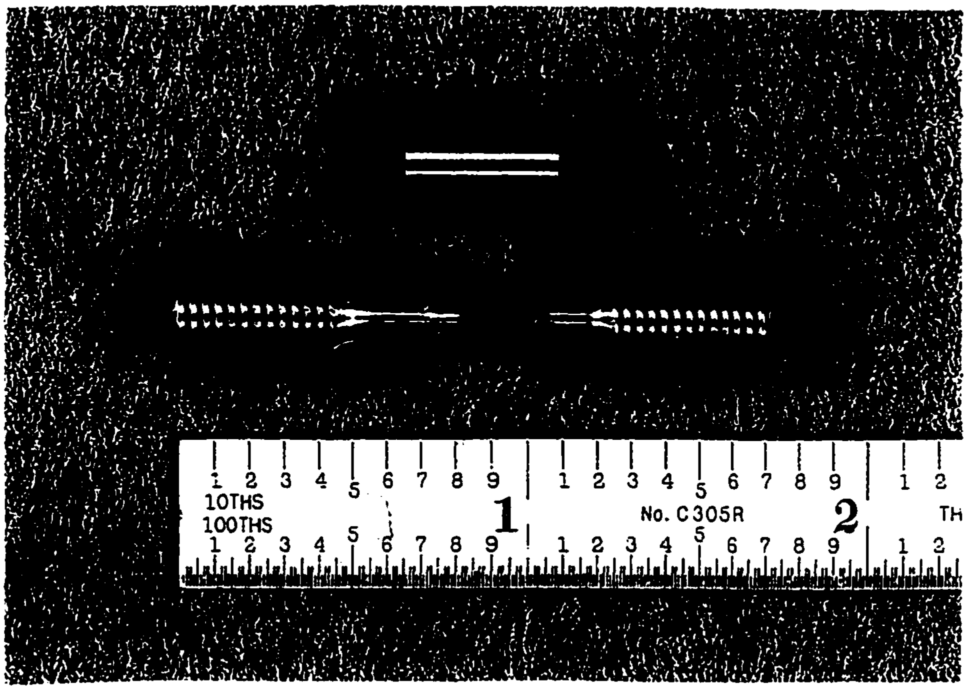

Figure 3.2 As prepared Vitreloy® 1 composite compression and tension samples.

In the process of making samples, it was found that a substantial amount of gas was evolved from the specimens reinforced with music wire. We determined that the gas was hydrogen that was absorbed in the rust removal process. To remove the hydrogen, the wires were baked at 973 K for 2 hours prior to fabricating composite specimens.

Although this baking temperature is less than the 1063 K annealing temperature of 1080 steel[11], it is still 47% of the melting temperature, and recovery, recrystallization and some grain growth are expected, and should produce changes in the as drawn mechanical properties of the music wire. In addition, the processing temperatures are in the austenitizing range for 1080 steel; the elevated temperature followed by quenching effectively heat treats the steel wire.

By contrast, the properties of the tungsten are not affected by the fabrication temperature. The peak processing temperature, at 1198 K, is substantially less than the 3683 K melting temperature of pure tungsten, and no significant recrystallization or grain growth is expected.

3.3 Experimental Procedure

The porosity of the prepared samples was evaluated in two ways. First, it was found using hydrostatic weighing combined with knowledge of the fiber volume fraction measured by analyzing backscatter SEM micrographs. It was also ascertained using a microscopic analysis in which porosity of a sample cross section is measured, then extrapolated assuming homogeneity as outlined in the Annual book of ASTM standards[12].

The composite samples were sliced normal to the fiber orientation. We obtained x-ray diffraction patterns of the slices using an Inel diffractometer with a position sensitive detector and Co Kα radiation (wavelength = 0.1790 nm). The cut surface was then polished and analyzed with scanning electron microscopy (SEM).

Tensile tests were performed on the as received reinforcing wires using an Instron 4204 load frame and a displacement rate of 0.02 inches per minute. The wires were held between soft metal pads which were clamped in tensile test jaws. The tensile test jaws were attached to the load frame via universal joints to guarantee axial loading. Strain was measured using a calibrated extensometer.

The temperatures at which the samples were fabricated was high enough to affect the properties of the steel wire. To evaluate the change in the microstructure of the steel wire, steel reinforced samples were sectioned perpendicular to the fiber axis, mounted in an epoxy mount and polished, followed by an etch using Nitol (2% nitric acid/ethanol solution). The samples were then analyzed using microscopy, and Vickers microhardness was measured.

An Instron 4204 load frame was used to perform quasi-static tensile tests, and compression tests were performed on an MTS 319.25 axial-torsional load frame. Both tensile and compressive strain was measured using a calibrated extensometer. The tensile strain rate was 0.02 inches per minute, and the compressive strain rate was 0.01 inches per minute. The compression samples were held between two WC platens in a loading fixture designed to guarantee axial loading. The ends of the compression samples were lubricated to prevent "barreling" of the sample. The tensile specimens were held in threaded grips; the grips are fitted with a universal joint at their point of attachment to insure axial loading.

Following testing, fractured samples were examined using scanning electron microscopy (SEM).

3.4 Experimental Results and Discussion

3.4.1. Wire Tensile Tests

Tensile tests were performed on the as received steel and tungsten wires, and are shown in Figure 3.3. The wires failed (repeatedly) at the point at which they entered the grips. As already discussed, the steel undergoes microstructural changes at the processing temperatures, and the mechanical properties of the music wire following processing undoubtedly differ from that measured in the tensile tests. The strength of the music wire prior to processing is 2.5 GPa; following processing it decreases to 1.8 GPa (extrapolated from hardness data).

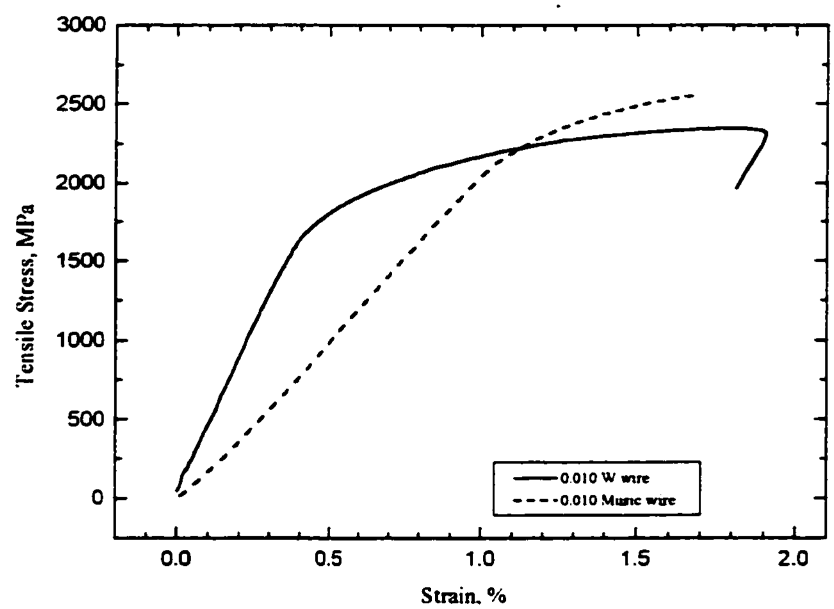

Figure 3.3 Tensile stress-strain curves for 254 μm (0.010 in.) tungsten wire and 1080 steel (music) wire.

3.4.2 Properties of the As Processed Steel Wire

Vickers hardness tests were performed on the steel wire in the composite. The Vickers hardness is H_v=530, which corresponds to a Rockwell C scale hardness, R_c=51. Using tables in Metals Handbook[11], the strength was estimated to be 1825 MPa. Figure 3.4 is an optical micrograph of the steel wire, at 400X. The microstructure was determined to be predominately bainite, with a small amount of martensite; this is confirmed by data in Metals Handbook.

3.4.3 Porosity Measurement

The quality of the composite samples varied with the type and amount of reinforcement. The tungsten wire wet better than the steel wire, and high fiber volume

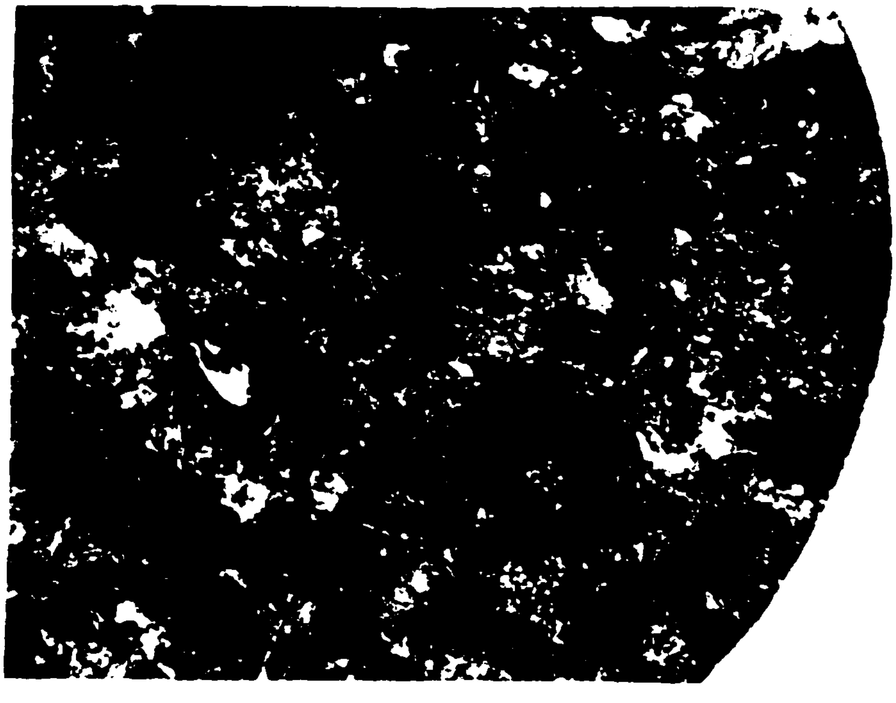

Figure 3.4 Micrograph of as processed 1080 steel wire embedded in Vitreloy® 1 matrix. Microstructure is bainite with some martensite. (400X, Nitol etch)

fractions seemed to infiltrate better than low volume fractions, particularly with respect to samples reinforced with music wire.

Porosity was measured on tungsten reinforced composites with volume fractions of 60% and 80%. The apparent porosity determined by SEM micrographs was less than 1%. The porosity obtained by hydrostatic weighing combined with measurement of V_f by microscopy was 3% ± 1%.

3.4.4 Fiber-Matrix Interface Analysis

X-ray diffraction patterns of the composite samples is shown in Figure 3.5, along with the pattern from the unreinforced matrix material (Vitreloy® 1). The Vitreloy® 1 shows the broad diffraction peak typical of a fully amorphous structure. At low fiber volume fractions this amorphous diffraction pattern is superimposed with the bcc peaks of the reinforcing wire. The amorphous diffraction pattern is obscured by the fiber peaks at high volume fractions. Some small crystalline peaks are visible at low fiber volume fractions.

The interfacial region of the tungsten and steel reinforced composites are shown in Figures 3.6 and 3.7, respectively. Note the presence of small crystals (the angular areas of dark contrast) next to the wires. There was typically 1% to 5% V_f crystalline material in the matrix, depending on the sample. Crystals in the steel samples tended to be carbides, which formed next to the wire. The details of the crystals in the tungsten samples has not yet been determined. The thickness of the interface layer on both types of reinforcement is approximately 250 nm.

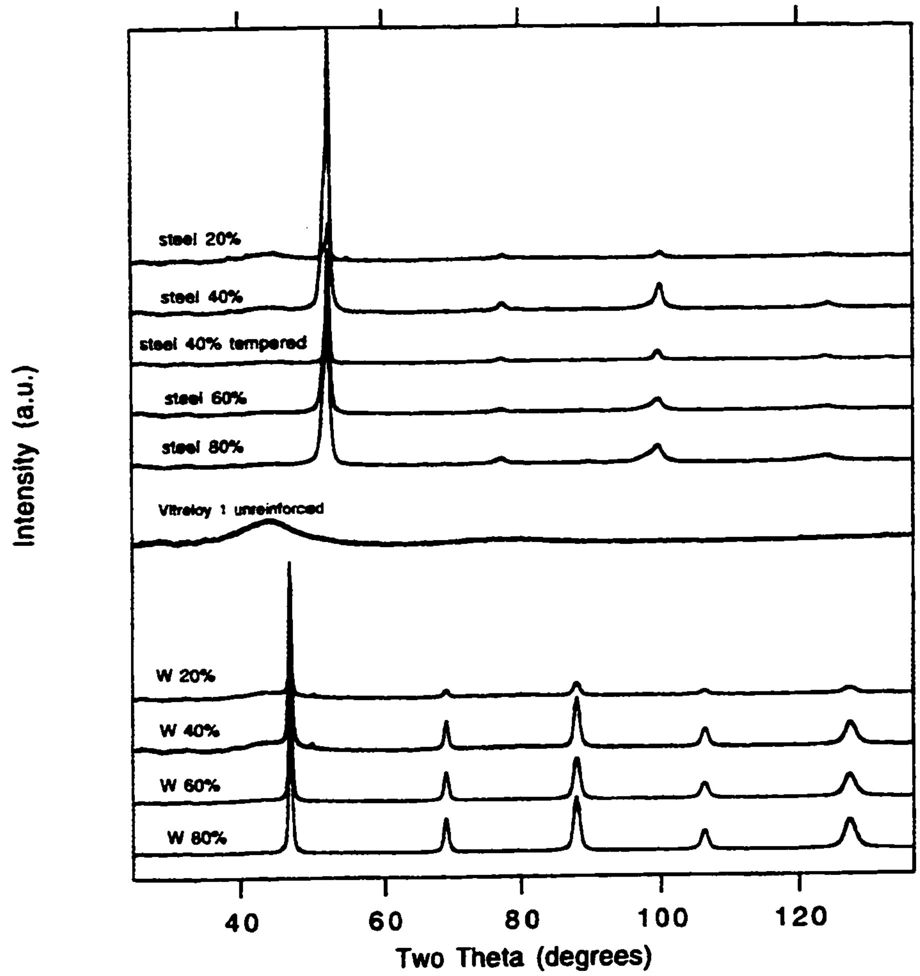

Figure 3.5 X-ray diffraction pattern for uniaxially reinforced bulk metallic glass matrix composites. Co Kα radiation (l = 0.17902 nm) was used. Percentages are volume fraction of reinforcement.

3.4.5 Residual Stresses Analysis

Metallic glass metal matrix composites (MMC) are fabricated at a high temperature (800 ^{0}C) then cooled to room temperature. This temperature difference, ΔT, is equal to: $\Delta T = T_f - T_i$, where T_i and T_f are the initial and final temperatures, respectively. Vitreloy® 1 becomes too viscous to flow below the glass transition.

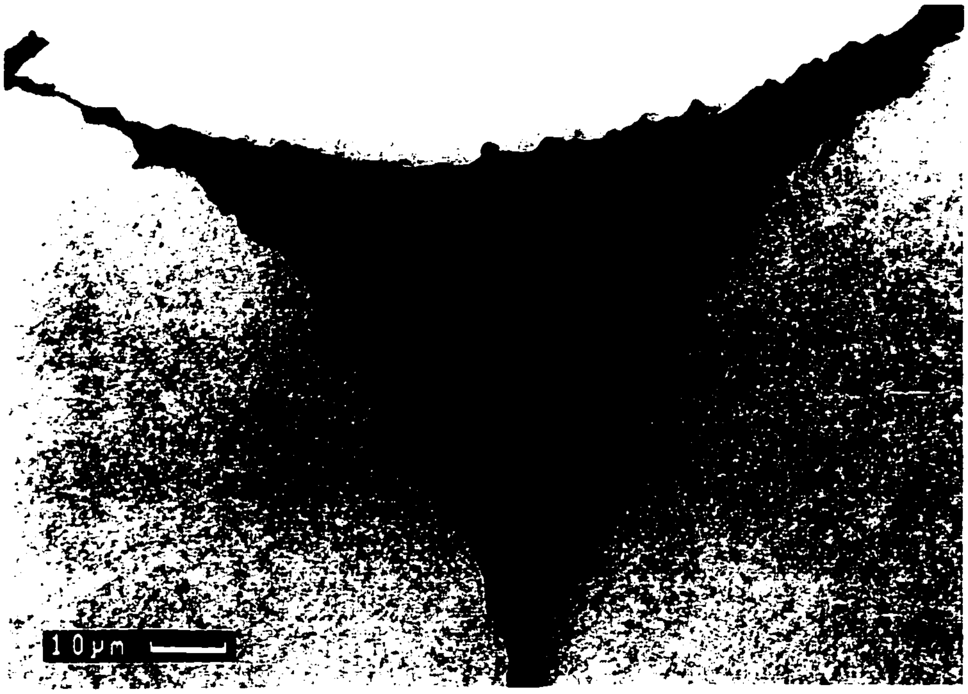

Figure 3.6 SEM micrograph in backscatter mode. Sample is 80% V_f W wire in Vitreloy® 1 matrix. Lighter regions are W wire, darker region is matrix. Very dark crystals are visible in the matrix.

Figure 3.7 SEM micrograph of 60% V_f steel-wire-reinforced Vitreloy® 1 matrix composite, taken in backscatter mode. Dark circular areas are steel wires. Small angular dark area next to wire is carbide crystal.

temperature, $T_g = 680\ ^0C$. Therefore, $\Delta T = 300\ ^0C - 680\ ^0C$, or $-380\ ^0C$. The coefficient of thermal expansion (CTE) of the matrix is denoted α_m, and that of the fiber is α_f. If $\alpha_m \neq \alpha_f$, residual strains (and hence stresses) equal to: $\varepsilon_t = \Delta\alpha\Delta T$ build upon cooling. These residual stresses typically lower tensile yield and ultimate strengths[13], as well as reduce fracture toughness[14]

The residual stress in the matrix affects the path of crack propagation. If $\Delta\alpha$ is negative (α_f-$\alpha_m < 0$, e.g., tungsten wire), then the residual hoop and axial stress in the matrix is tensile, while the radial stresses in the matrix and fiber, and the axial and hoop stresses in the fiber, are compressive. This tensile matrix hoop stress encourages cracks to propagate toward the reinforcing fibers[17]. On the other hand, if $\Delta\alpha$ is positive, (α_f-$\alpha_m > 0$, e.g., music wire), the residual hoop and axial stresses in the matrix are compressive, while the residual hoop and axial stress in the fiber, as well as the radial stresses in the fiber and the matrix, are tensile. Compressive hoop stress in the matrix deflects cracks away from the fibers, typically toward the fiber/matrix interface[18]. This will encourage delamination and fiber pull out because the fiber is not as tightly gripped by the matrix as when $\Delta\alpha$ is negative. Cracks will propagate perpendicular to the fiber axis in both cases, since the loading axis is parallel to the fiber.

The coaxial cylinder model was used to calculate the residual stress due to cooling in a metallic matrix composite. Mathcad® was used to assemble the equations provided in references[15, 16]. The sequence of equations used in the calculations is listed in Appendix I. Figures 3.8 and 3.9 show the results of the calculations.

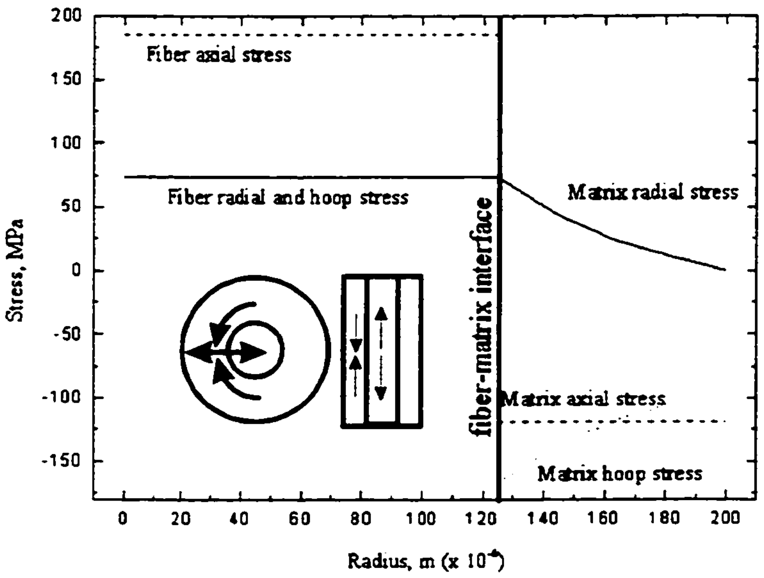

Figure 3.8 Residual cooling stresses in a music wire/Vitreloy® 1 composite calculated using the coaxial cylinder model.

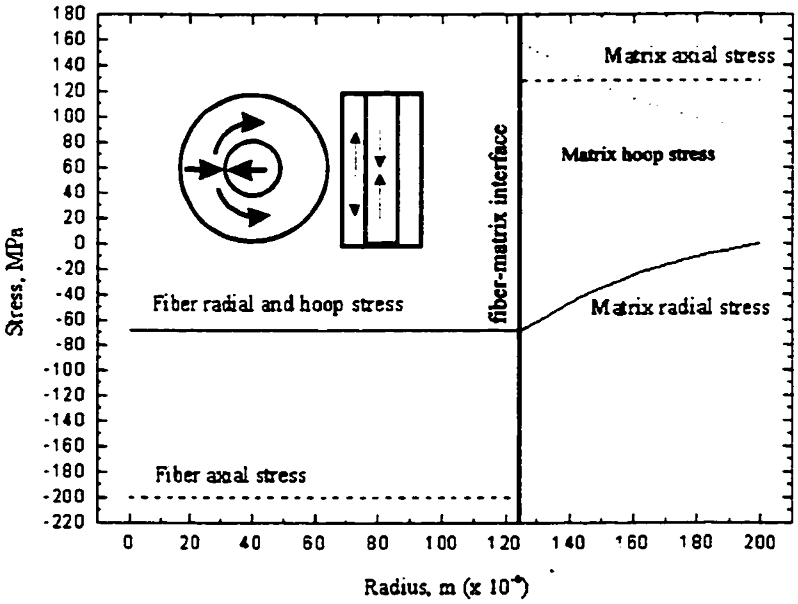

Figure 3.9 Residual cooling stresses in a tungsten/Vitreloy® 1 composite calculated using the coaxial cylinder model.

To calculate the stresses due to an applied (compressive or tensile) applied load, in addition to those from thermal contraction, the Eshelby equivalent inclusion method was used. The appropriate equations for this method were also assembled on Mathcad®, and are included in Appendix II.

Unlike other MMC matrix materials (e.g. aluminum), metallic glasses do not have dislocations, and cannot undergo extensive plastic deformation. The wires, however, have limited ductility. It is assumed that yielding (in tension or compression) begins when the von Mises stresses on the wires reached the wire yield strength. The appropriate equations were included to calculate the von Mises stresses on the wires. The load was varied and the fiber von Mises stresses were evaluated until the fiber yield stress was reached. This method was used to determine the load at which inelastic deformation begins.

3.4.6 Elastic Modulus

The slope of the stress-strain curve provided the elastic modulus, E, for each composite. Figures 3.10 and 3.11 show the measured elastic modulus for the tungsten and music wire composites, along with the modulus calculated using the rule of mixtures. The rule of mixtures is a simple weighted average of the elastic moduli of each component:

$$E_c = V_f E_f + (1-V_f)E_m$$

where the subscripts c, f and m represent the composite, fiber and matrix, respectively, and V_f is the fiber volume fraction.

The tungsten composites shows remarkably good agreement with the rule of mixtures calculations, and the error bars, which represent a standard deviation, are very narrow. There is more scatter in the results of the music wire composites. The music wire does not wet quite as well as the tungsten, and as a result, more of the samples have small voids, which affect the measurement. There is also no way to insure that the fiber volume fraction of the *finish machined samples* is the same as the *as fabricated ingots*, because the fiber distribution is not always uniform. The 40% V_f music wire/ Vitreloy® 1 sample has the largest difference between measured and calculated elastic modulus, but this difference is still less than 10%, which is well within reasonable experimental variation.

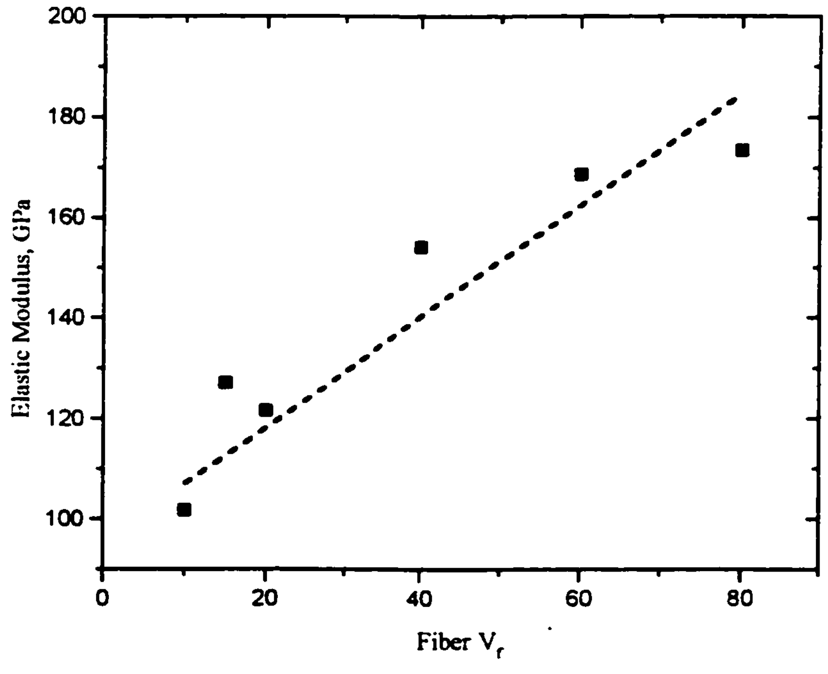

Figure 3.10 Elastic modulus of music wire/Vitreloy® 1 composites versus fiber volume fraction. The dashed line is the modulus calculated using the rule of mixtures method.

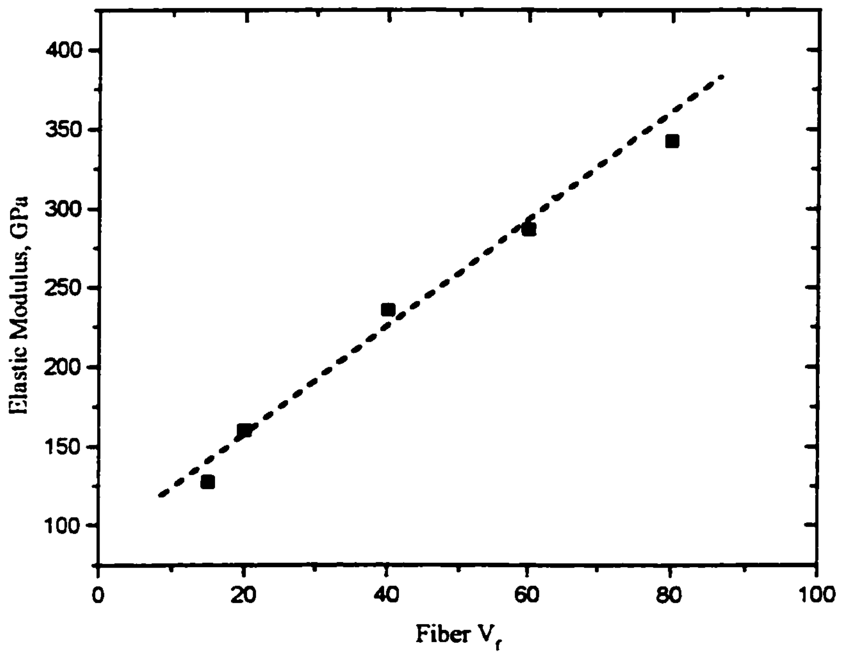

Figure 3.11 Elastic modulus of tungsten/Vitreloy® 1 composites versus fiber volume fraction. The dashed line is the modulus calculated using the rule of mixtures method.

3.4.7 Compression Tests

Quasi-static compression tests were performed on all samples. Figures 3.12 and 3.13 are stress-strain curves of tungsten and music-wire reinforced composites in compression.

All of the tungsten composites show elastic-perfectly plastic stress-strain behavior, with strains of up to 19%. The maximum strength of the composites covers a narrow range; increasing fiber volume fraction does not increase the ultimate strength of the composite. Examination of the stress-strain curve shows a pronounced change in the slope of the tungsten composites (a noticeable "dog leg"), which varies with fiber volume fraction. This indicates the point at which the fiber reinforcement first yields.

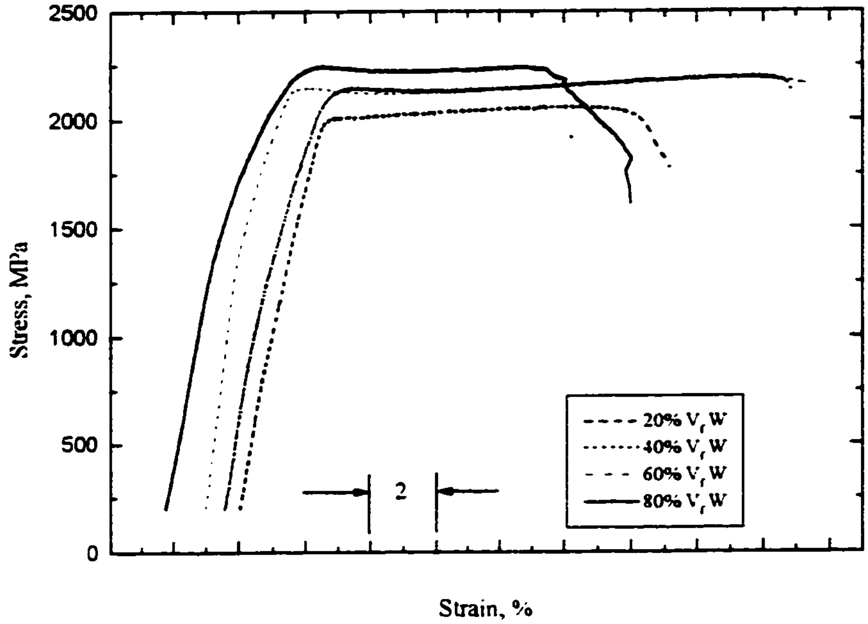

Figure 3.12 Compressive stress-strain for tungsten/Vitreloy® 1 composite.

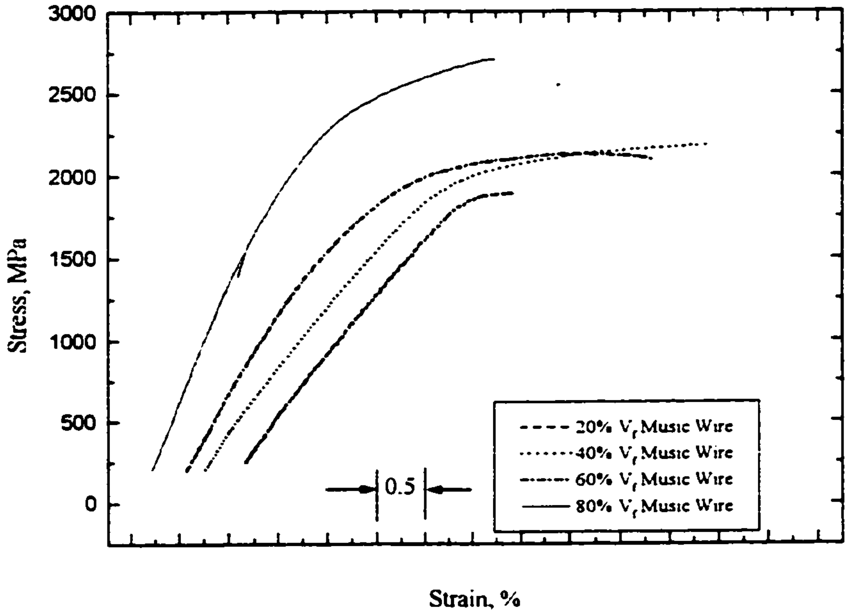

Figure 3.13 Compressive stress-strain curve for music wire/Vitreloy® 1 composite.

The stress at which yield occurs for each fiber volume fraction is listed in table 3.2. Calculations to determine the macroscopic stress at which the fibers yield were performed using the Eshelby equivalent inclusion method, as described in section 3.4.5. The calculated yield strength is also listed in table 3.2. The measured yield stress is in good agreement with that predicted from calculations.

The stress-strain curves for the music-wire reinforced composite are shown in figure 3.13. Unlike the tungsten reinforced composite, the music wire composite does not show a distinct fiber yield point in compression. Nor does it show as much plastic deformation, with a strain to failure of 6% for the 40% V_f sample. Unlike the tungsten composite, the inelastic portion of the stress-strain curve for the music-wire-reinforced composite shows some work hardening, rather than perfectly plastic behavior.

Although the strain-to-failure differed between the composites, the ultimate strength in compression was strikingly similar. Figures 3.14-3.17 are stress-strain curves for music-wire composites, along with the tungsten reinforced composite of the same volume fraction. The ultimate strength for all except the 80% V_f music wire sample are virtually the same. This indicates that the ultimate strength of the composite is governed by the strength of the matrix rather than the strength of the fiber.

The failure mode changed with fiber type and volume fraction. Figure 3.18 is a photograph of an unreinforced Vitreloy® 1 sample which was tested in compression. Although this sample did not fracture in a single plane, as did those of Bruck, et al., it did cleave on multiple 45 degree planes, leaving smooth areas that indicate fast fracture, as well as the characteristic "veinous" patterns typical of metallic glasses.

Volume Fraction, V_f %	Measured Yield Stress, σ_y MPa	Calculated Yield Stress, σ_y MPa
20	775	708
40	1050	974
60	1300	1240
80	1400	1500

Table 3.2 Tungsten compressive yield stress versus fiber volume fraction.

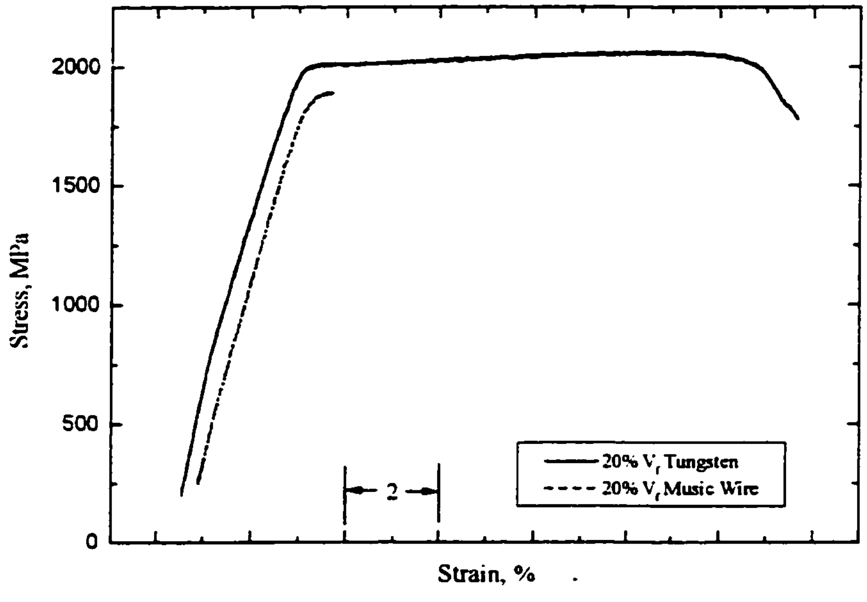

Figure 3.14 Compressive stress-strain for 20% V_f tungsten and music wire composites.

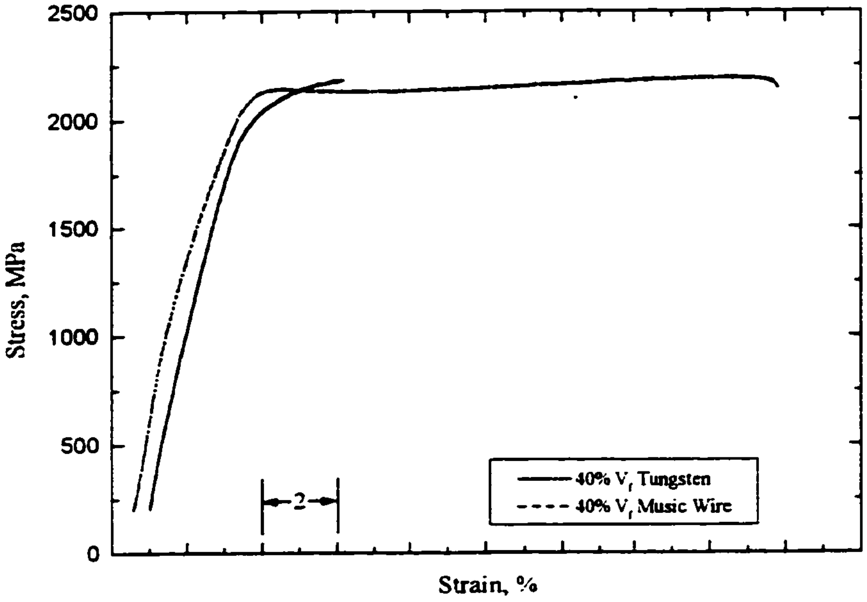

Figure 3.15 Compressive stress-strain for 40% V_f tungsten and music wire composites.

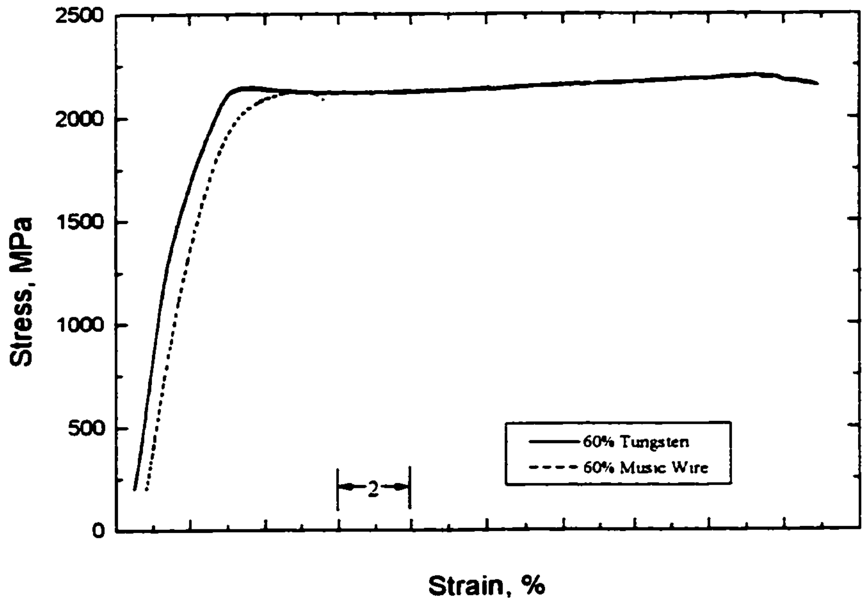

Figure 3.16 Compressive stress-strain for 60% V_f tungsten and music wire composites.

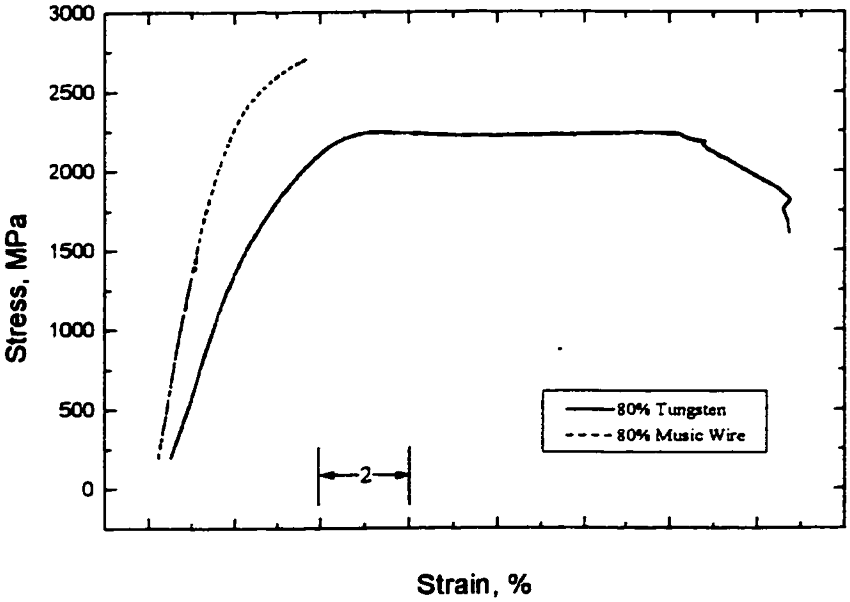

Figure 3.17 Compressive stress-strain for 80% V_f tungsten and music wire composites.

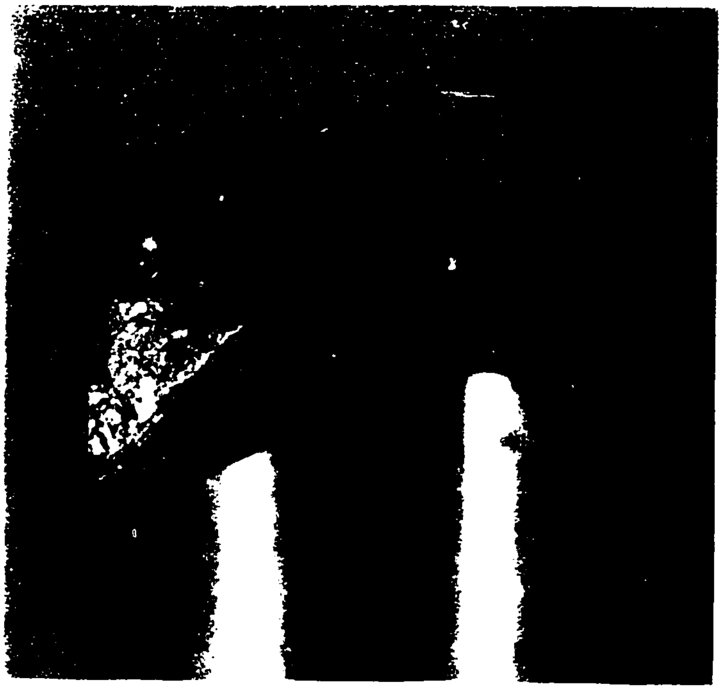

Figure 3.18 Profile of Vitreloy® 1 compression sample. Note the 45 degree angle characteristic of shear band failure in metallic glass.

A tungsten reinforced Vitreloy® 1 composite compression sample is shown in figure 3.19. The failure mode changes from the 45 degree shear bands as illustrated in figure 3.18 to localized fiber buckling and tilting.

Figure 3.20 is a fracture surface of a 20% music-wire reinforced composite. Low fiber volume fractions show a mixed mode of failure, with areas that sheared at ~45 degrees, along with areas of vertical delamination. As the fiber volume fraction increased, failure mode shifted from shear to vertical splitting and buckling. An 80% V_f tungsten compression specimen is illustrated in figure 3.21. Note that the cracks on the compression face run toward and through the tungsten wires, as would be expected with the tungsten composite, because cooling leaves the matrix in a state

Figure 3.19 60% V_f Tungsten wire/Vitreloy® 1 composite compression sample. Failure mode changed from shear bands (Fig. 3.18) to fiber buckling and tilting.

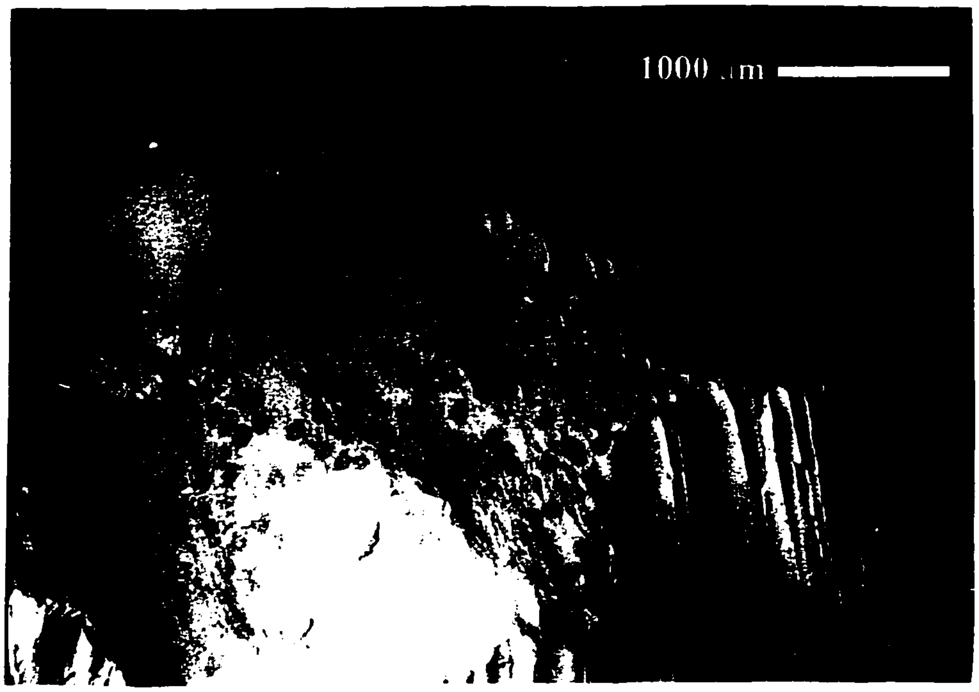

Figure 3.20 Compressive fracture surface of 20% V_f music wire/Vitreloy® 1 composite.

Figure 3.21 Compressive failure of 80% tungsten/Vitreloy® 1 composite. Note that at the top cracks run from fiber to fiber, and longitudinal splitting and buckling occurs in fibers.

of residual tension. The side view shows clearly that the fibers split longitudinally and buckled. It is proposed that the fibers first yield, followed by axial shear cracking, which makes the fibers unstable and unable to prevent buckling in the composite. This failure mode is consistent with work on titanium reinforced with monofilament SiC performed by Spowart and Clyne [19]. The onset of buckling may be seen on the compression stress-strain curve (figure 3.17), as the point when the 80% V_f tungsten sample work-softens.

Between the first compression failure event, when the fibers yield, and the last, when the sample fails by either mixed mode or longitudinal fiber tearing and buckling, is a region of perfectly-plastic deformation. In this region multiple shear bands are generated throughout the sample. Elastic-perfectly plastic behavior has been seen in metallic glasses with aspect ratios less than 1.5, as in the work by Bruck, et.al., [2] and Pampillo and Chen [20]. The low aspect ratio results in a plane strain state in the compression sample, which acts as a constraint to shear crack propagation. Multiple shear bands in these samples are revealed in microscopy. Leng and Courtney found multiple shear band formation in ductile metal matrix composites laminated with metallic glass[10]. According to their work, multiple shear bands may be localized or uniformly distributed. Localized shear banding is predicted when initial slip displacements are large (as, for example, when V_f is low), while uniform banding is expected when the initial slip displacement is small. When the fiber volume fraction is high, the matrix is highly constrained, and slip displacement is small. Stress concentrations build up at the tip of a propagating shear band; when the shear band meets an obstacle, this stress concentration triggers another shear band to form, typically at right angles to the first.

The nature of multiple shear band formation may be seen in figure 3.22, an SEM photograph of the side of a 60% V_f composite compression sample. The shear bands are plainly visible, making a chevron pattern on the side of the sample. There are several interesting aspects of shear band propagation revealed by this photograph. Using the rule that propagating cracks will stop when reaching an existing crack (as outlined in Metals Handbook), one may see the order in which shear bands formed.

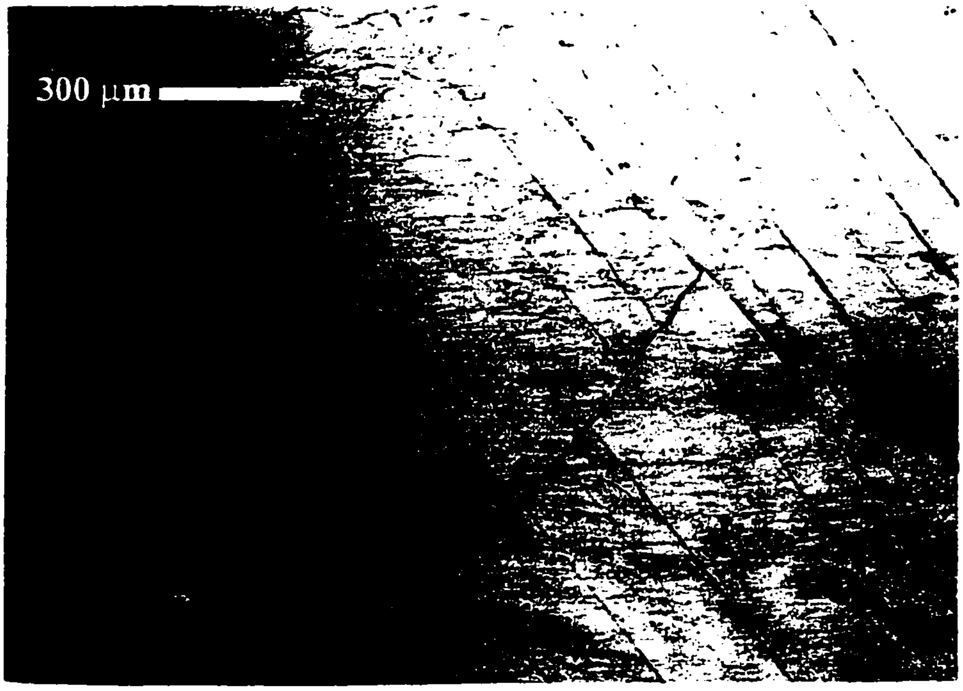

Figure 3.22 Multiple shear bands form a chevron pattern in a 60% V_f tungsten/ Vitreloy® 1 composite. Note that shear bands with a particular +/-45 degree orientation form in clusters.

By examining the photograph, it appears that the first group of shear bands formed in the top right quadrant, with an orientation of -45 degrees. The next dominate shear bands appear in the left side of the photograph. These have a +45 degree orientation and terminate upon reaching the first set. This is followed by a third set of shear bands, which have smaller dimensions and a -45 degree orientation. The pattern then repeats itself.

Thus multiple shear bands with a +45 degree orientation form over one area, followed by formation of shear bands with a -45 degree orientation in an adjacent area. The large region of perfectly plastic deformation shown in the tungsten composite stress strain curve reflects the stage during which multiple shear bands are being formed in the sample. The shear bands in the photograph are uniformly spaced; presumably, the spacing would decrease as the fiber volume fraction increases, up to the point at which the failure mode changes to longitudinal shear cracking. This assumption is reinforced by the fact that strain to failure increased as fiber volume fraction increased, up to 60% V_f. If the shear band spacing is closer, then more shear bands can be accommodated, which will allow greater strain before failure.

The compression samples reinforced with steel did not sustain as much inelastic deformation as those reinforced with tungsten, and did not fail in as gentle a manner: they literally burst apart; the only pieces that could be found were shards of wire with bits of matrix material attached. This may be understood as follows. The tensile radial stress which forms upon processing, combined with the reaction products at the fiber-matrix interface, results in a weak interfacial bond between the steel wire and the matrix.. By comparison, the compressive radial stress in the tungsten composite serves to enhance the fiber-matrix bond strength. Although the interface bond strength between the tungsten/Vitreloy® 1 composite differs from that of the music wire/Vitreloy® 1 composite, even if it were equal, the tungsten would be more tightly bound to the matrix because it is in compression. The compressive normal force acts to hold the tungsten in place through friction, which is not present in the music wire composite. The magnitude of these normal forces are illustrated in figures 3.8 and 3.9. The steel also has a much higher yield strength than the tungsten. While the calculated load necessary to produce yield in the 40% V_f tungsten composite (in compression) is 974 MPa, the calculated load necessary to reach the 2.2 GPa stress required for music wire yielding is 1560 GPa, which is 60% greater than that of the tungsten. This high load is why an isolated yield event was not visible on compression tests of the music wire reinforced samples. This higher load means a substantial amount of energy is stored in the wires, which is released as shear bands begin to propagate in the sample. The wires, rather than acting to constrain the shear bands, drive their propagation, resulting in the disintegration of the sample.

Figure 3.23 is an SEM photograph of the fracture surface of a tungsten/Vitreloy® 1 composite which failed in shear. There are several interesting surface features in this photograph. There are areas which are very smooth, areas which show the veinous pattern typical of unreinforced metallic glasses, and areas that resemble microvoid coalescence. The smooth areas are understood to be areas of fast fracture, while rough areas indicate a slower, more ductile failure. The shear event propagated from the upper left to the lower right; evidence for this comes from at least two places. First, the matrix material is spread across the wires in this direction. It seems that the temperatures in the shear band become high enough for the matrix to experience some viscous flow. Matrix material becoming viscous and flowing within the shear band has been proposed in the past as a possible explanation of the veinous pattern of metallic glass fracture surfaces[21]. Second, the orientation of the microvoids, with the closed end pointing toward the source of the fracture, as it is with fracture of ductile metals. By calling these features microvoids, I am merely describing their appearance, and not implying that their formation is the same as microvoid formation in ductile metals. It is suggested that fracture does not begin at an isolated point and proceed in a linear fashion; rather, it could occur in several isolated points in the interior of the sample, as depicted by the areas of fast fracture, which releases heat, softening the adjacent metal, which ruptures in a slower, more ductile manner. This would be in rough agreement with other glasses (e.g. oxide glass) have shiny, smooth areas surrounding points of crack initiation, called mirror regions, which transition to mist and hackle regions, where surface roughness increases[22].

Figure 3.23 Compressive fracture surface of 60% V_f tungsten/ Vitreloy® 1 composite. The shear band propagated from top to bottom, as shown by the way the matrix flowed over the wire, and the alignment of what appear to be microvoids adjacent to the wires.

3.4.8 Tensile Tests

Tensile experiments were performed on at least four samples of tungsten and music wire reinforced metallic glass with fiber volume fractions of 20, 40, 60, and 80%, as well as one experiment of each at V_f of 10 and 15%. The stress-strain curves are shown in Figures 3.24 and 3.25. There was substantial scatter in the data; many of the samples, those with low fiber volume fractions and particularly those reinforced with music wire contained voids, and fiber distribution was often uneven. However, enough tensile tests were performed on each type of composite to give confidence in the test results.

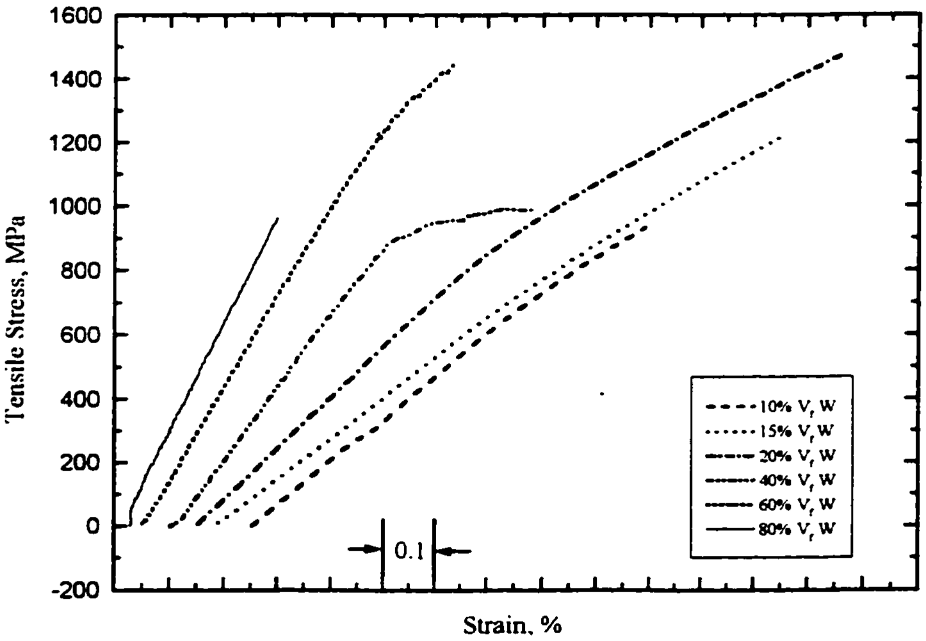

Figure 3.24 Tensile stress-strain curves for tungsten reinforced Vitreloy® 1 composites.

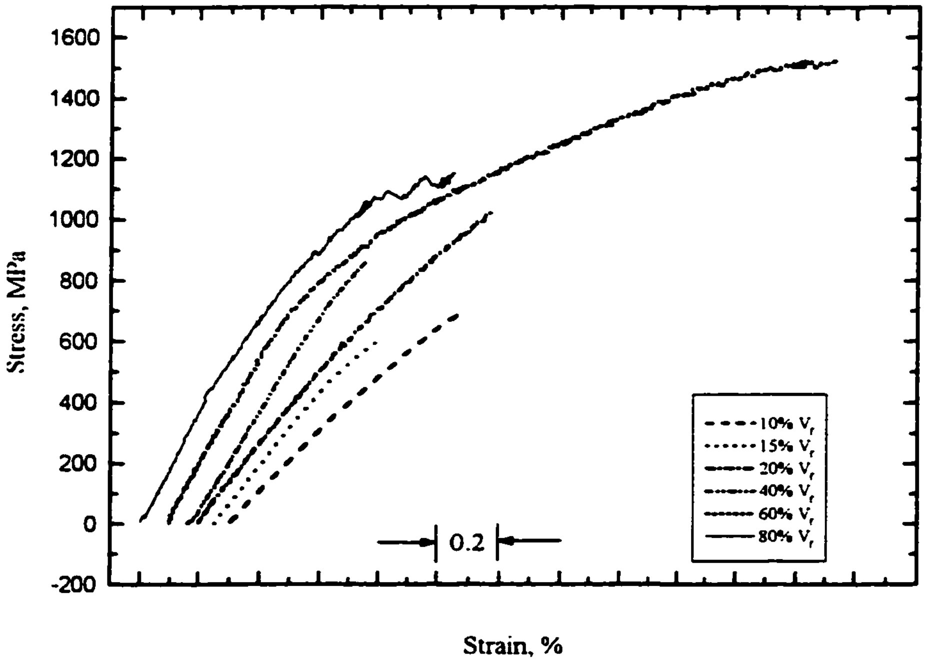

Figure 3.25 Tensile stress-strain curves for music wire reinforced Vitreloy® 1 composites.

The maximum strength of each of the composites was lower than that of unreinforced Vitreloy® 1 and, in every case except one, the strain to failure was also significantly lower. The most favorable results of each reinforcement, in terms of maximum strength and strain to failure, are plotted in Figure 3.26 along with the stress-strain curve for unreinforced Vitreloy® 1 . Numerical integration of the area under the stress-strain curve gives the energy per unit volume (J/m^3) to break the material:

$$\frac{J}{m^3} = \int_0^{\varepsilon_m} \sigma(\varepsilon)\, d\varepsilon$$

Performing this calculation for the Vitreloy® 1 and 60% music wire/Vitreloy® 1 composite reveals the composite needs 18% more energy to reach failure, while the 20% tungsten reinforced composite requires 49% less.

Both of the above samples show an elastic range (in which the modulus is in excellent agreement with the rule of mixtures) followed by a yielding event, and a work hardening range, in which the matrix remains elastic while the reinforcing fibers undergo plastic deformation. These regions are described in the literature[23] as stage I and stage II, respectively. The metallic glass composites do not display a stage III region, which is described as plastic deformation of both matrix and fiber, because the metallic glass matrix remains elastic until failure. The superposition of tungsten wire and Vitreloy® 1 stress-

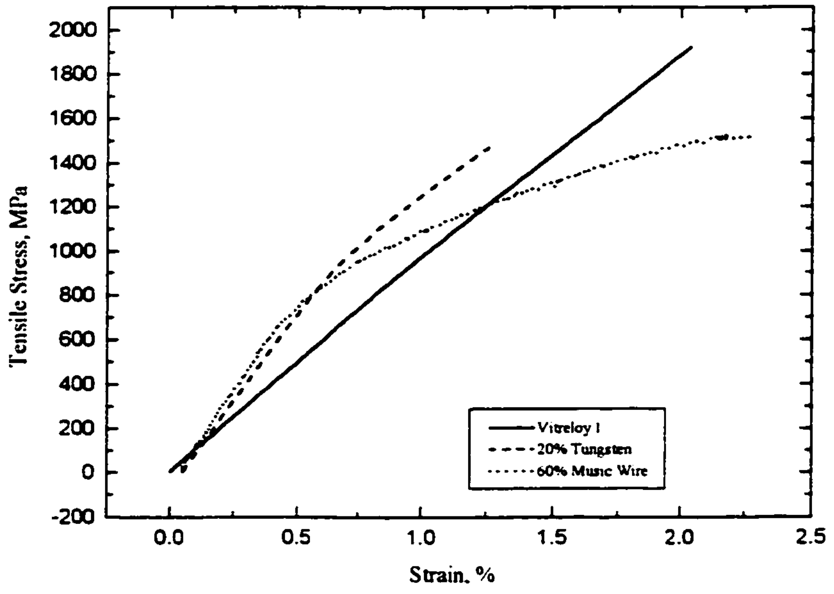

Figure 3.26 Tensile stress-strain curves of the music wire and tungsten reinforced Vitreloy® 1 composites that showed the most favorable results, in terms of ultimate strength and strain to failure, along with unreinforced Vitreloy® 1.

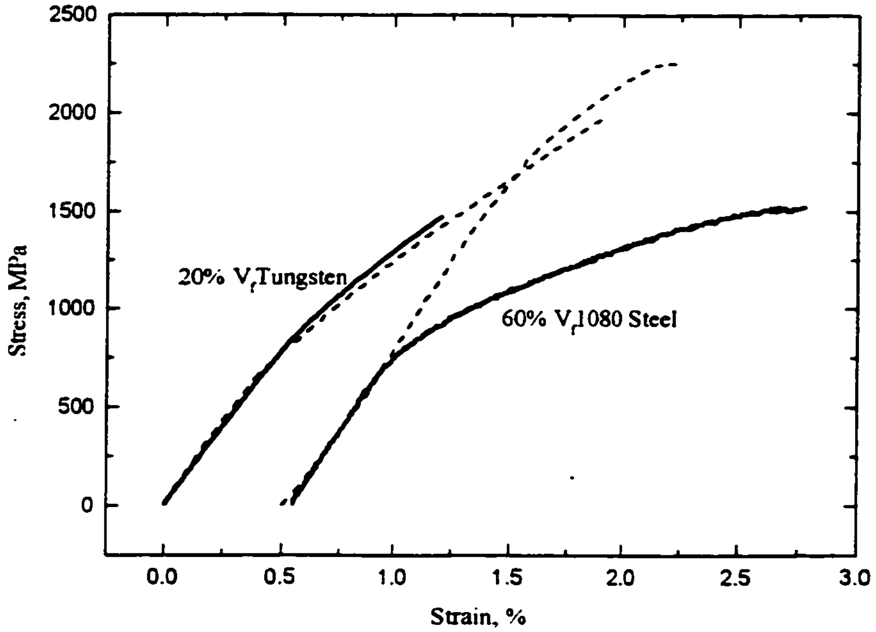

Figure 3.27 Tensile stress-strain curves for tungsten and music wire reinforced composites. Dashed lines are the curves predicted by the rule of mixtures.

strain curves using the rule of mixtures is in remarkably good agreement with that measured in tensile tests, as illustrated in figure 3.27. The music wire reinforced composite, however, yields substantially before the point predicted by calculation.

This kind of yield behavior, in which the tungsten reinforced samples agree well with predictions and the steel reinforced samples do not, occurs independent of fiber volume fraction. The tensile yield strength was calculated using the Eshelby equivalent inclusion method for each reinforcement, and these results are listed in Table 3.3, along with the measured yield strength of each. The measured yield strength was taken to be the stress at which the sample transitioned from stage I to stage II, and not at 0.2% offset strain. The yield point for the 80% V_f tungsten/Vitreloy® 1 composite is substantially below the predicted stress because the tungsten fails in tension prior to reaching this value.

V_f, %	Tungsten		Music Wire	
	Calculated σ_y, MPa	Measured σ_y, MPa	Calculated σ_y, MPa	Measured σ_y, MPa
20	856	800	1238	657
40	975	1000	1455	582
60	1230	1225	1672	875
80	1480	1200	1887	800

Table 3.3 Measured and calculated yield strengths of Vitreloy® 1 composites reinforced with tungsten and music wire.

Yield strength increases with fiber volume fraction in both the tungsten and music wire reinforced samples, as shown in Figure 3.28, a graph of tungsten yield strength versus fiber volume fraction.

The difference in yield behavior between the samples reinforced with tungsten and steel wires is due to the relative strength of the fiber-matrix interface, the residual thermal stresses, and the effect of Poisson contractions between the fiber and the matrix.

As has been illustrated, the tungsten wire is in a state of residual compression, while the steel wire is in state of tension. When the tensile load is applied, the matrix material, which has a higher Poisson ratio than the reinforcement, contracts around the wires, holding them more tightly. This adds to the compressed state of the tungsten; there is no slip between the wire and matrix at the interface, and the strains on the wire and matrix are truly identical. Tensile loads also serve to relieve the compressive axial stress on the tungsten, at least initially, which contributes to the wires flowing with the matrix

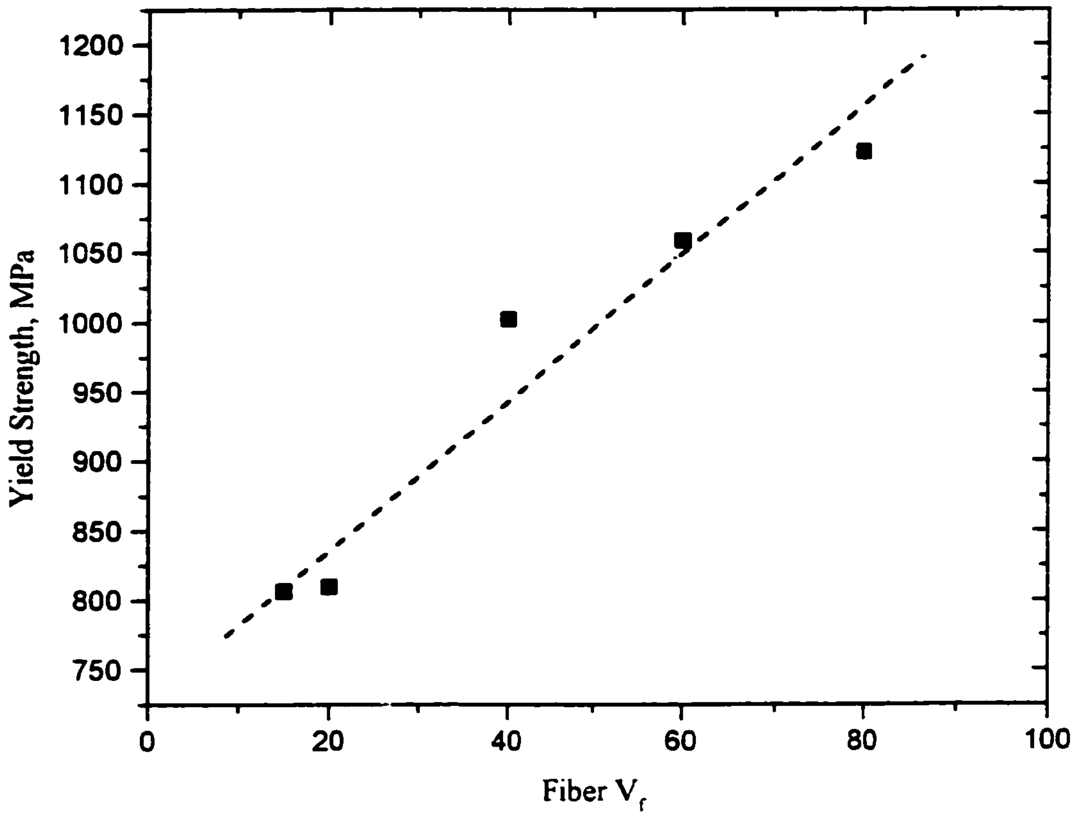

Figure 3.28 Average tungsten/Vitreloy® 1 composite tensile yield stress versus fiber volume fraction.

material. The music wire, on the other hand, is in a state of radial and axial tensile stress. Its resistance to axial strain builds quickly, and the radial tensile stress does not allow the matrix to as tightly grip the wire, even with the addition of the Poisson contractions. Figure 3.29 is a graph of a the stresses present in a 40% steel/Vitreloy® 1 composite which includes the residual thermal stress and a 1000 MPa axial load. From this graph one can see that there is still a 66 MPa tensile radial stress at the fiber/matrix interface. By contrast, Figure 3.30 is a 40% tungsten/Vitreloy® 1 composite with the same applied axial load. In this case the radial stress at the fiber matrix interface is -97 MPa in compression. Referring to figures 3.8 and 3.9 in section 3.4.5, one can see that the thermal radial stress at the fiber/matrix interface is 72 MPa and -70 MPa for the steel and tungsten composites, respectively. The lack of interface strength in the steel samples allows the fibers to debond and slide within the matrix, hence the apparent yield strength is substantially below that predicted by theory.

How strong is the interface? A standard method for determining interface strength is a fiber push-out test; these tests are well documented in the literature[24-26]. Push-out tests were not performed on the composite samples, but a fortunate event allowed for estimation of the interface strength of the music wire reinforced samples. Examining figure 3.25, the stress-strain curves for the music wire reinforced composite, one can see an erratic roughness in the curve for the 80% V_f sample at a stress of approximately 1100 MPa. This jump, and the subsequent jumps, are of the wire being pulled free of the matrix material. Figure 3.31 is a photograph of an 80% V_f music wire sample. The threaded end of the test specimen has a change in cross section, from the nominal thread size to the gage size of the test specimen. At 80% V_f the wires are essentially close packed. As one can see from the photograph, at a load below the failure load for the fibers the matrix and fibers debonded, and the core of fibers the diameter of the gage section pulled out of the threaded end. The fibers pulled out in a hexagon bundle which was 14.5 mm long with 2.5 mm across each flat, for a surface area of 217.5 mm^2. The load at initial failure (delamination) for this sample was 9820 N; the corresponding shear stress at the interface

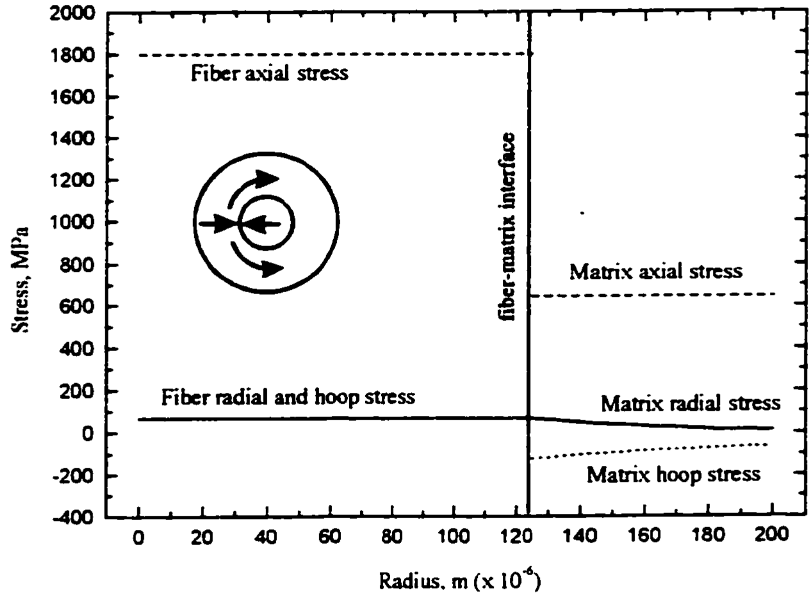

Figure 3.29 Matrix and fiber stress distributions for a 40% V_f music wire/Vitreloy® 1 composite, including thermal residual stresses and a 1000 MPa axial load.

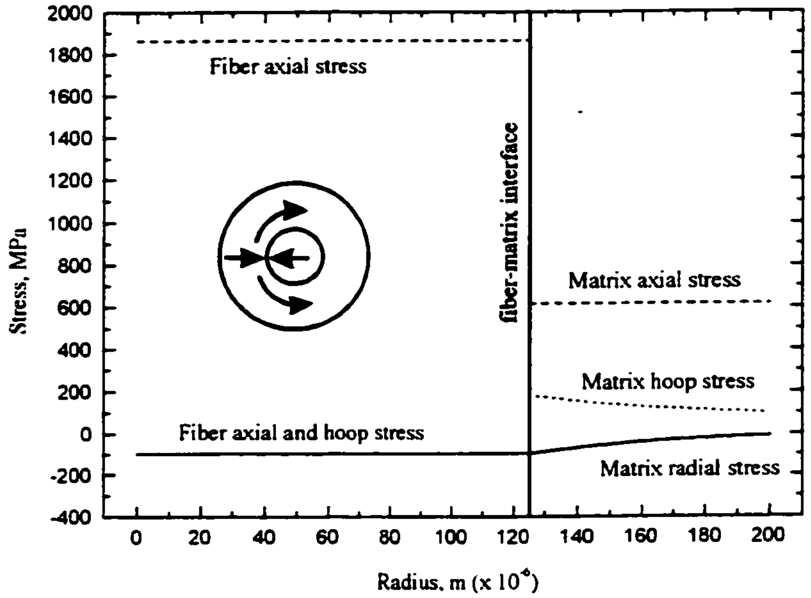

Figure 3.30 Matrix and fiber stress distributions for a 40% V_f tungsten wire/Vitreloy® 1 composite, including thermal residual stresses and a 1000 MPa axial load.

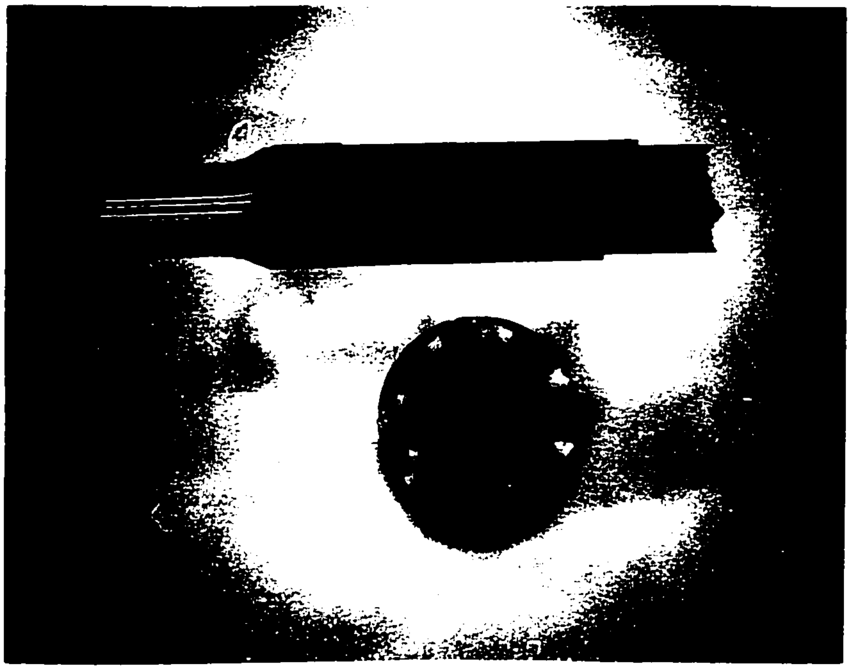

Figure 3.31 Fiber pullout of 80% music wire/Vitreloy® 1 composite tensile sample. Center portion of tensile test sample (top) was pulled away from threaded end (bottom).

was $\tau = 45.1$ MPa. All of the tensile samples reinforced with 80% music wire failed in this manner at a comparable shear stress.

The tensile strength of the composites increased with volume fraction, up to 60% V_f, then dropped. Graphs of the tensile strength versus volume fraction are shown in figures 3.32 and 3.33. As has been discussed, the sample reinforced with 80% music wire failed by fiber pull out from the threaded section. The 80% tungsten reinforced samples did not fail by pull out; as with all of the tungsten samples, it failed in a brittle manner. Figure 3.34 is an SEM photograph of the fracture surface of a 40% V_f tungsten/Vitreloy® 1 composite. The wires are highly constrained and in a triaxial stress state. The plane

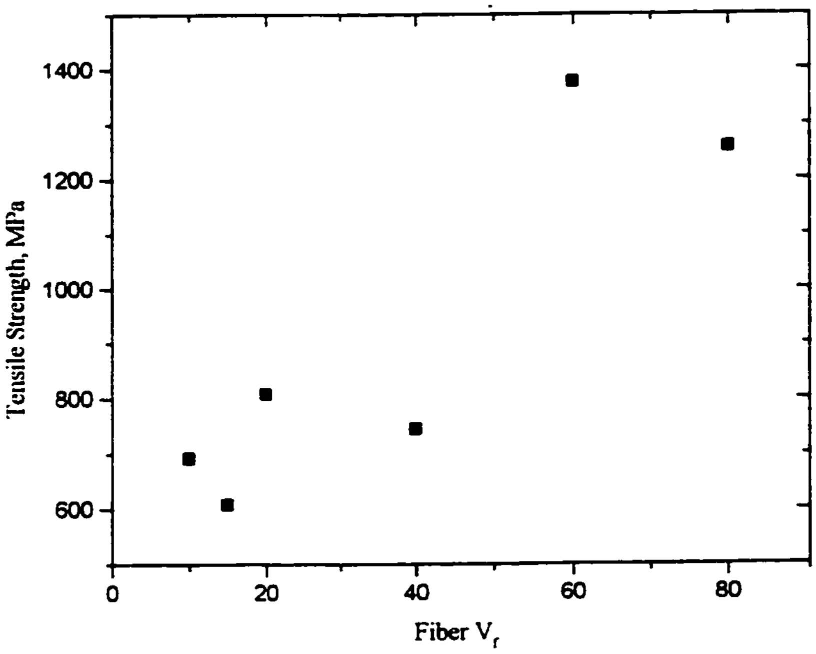

Figure 3.32 Average music wire/Vitreloy® 1 composite tensile strength versus fiber volume fraction.

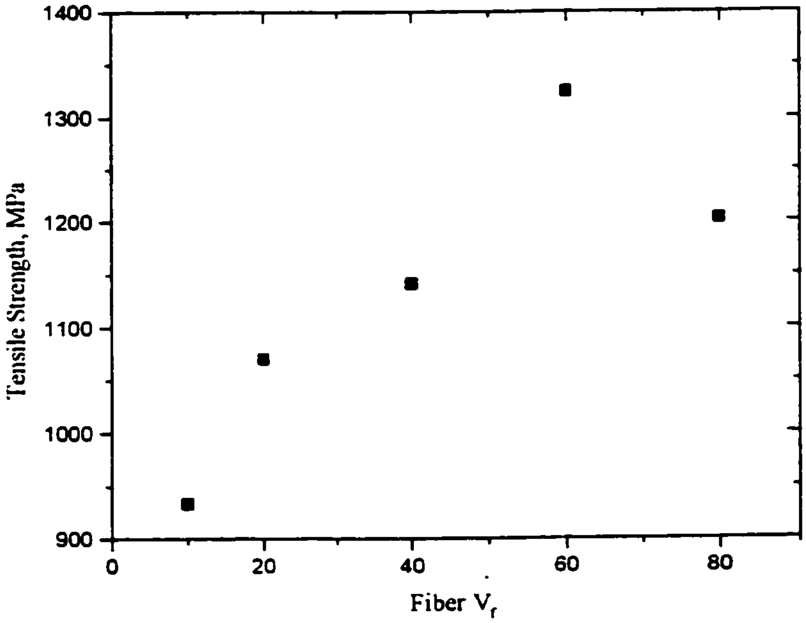

Figure 3.33 Average tungsten/ Vitreloy® 1 composite tensile strength versus fiber volume fraction.

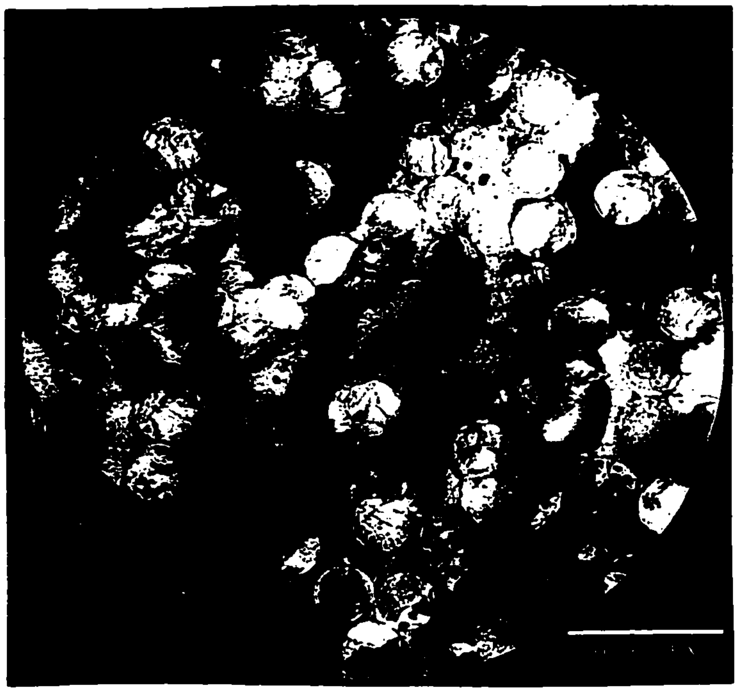

Figure 3.34 Tensile fracture surface of a 40% V_f tungsten/ Vitreloy® 1 composite. Fibers failed in brittle mode. Fracture surface was perpendicular to axis, with virtually no fiber pull out. Jelly bean shaped pit is visible in ~ 4 o'clock position.

strain fracture toughness of tungsten is 12-14 MPa√m[27]. Ashby, et al., have shown that highly constrained wires provided the least amount of toughening for a brittle matrix composite[28]. What is needed is interface debonding and ductile fiber rupture. As can be seen from the photograph, the tungsten wires failed in an entirely brittle manner, with smooth areas of fast fracture in the adjacent matrix. The fracture surface in all the tungsten composites tested was perpendicular to the axis of load.

The steel samples did not show the same failure behavior. Voids caused considerable scatter in samples with low fiber volume fractions, and fiber pull out resulted in the failure of the 80% V_f specimens. However, the samples reinforced with 60% V_f music wire fibers showed promising results, in terms of strength and strain to failure.

There was relatively little scatter in the experimental results. A martensitic high carbon steel (0.78-0.88 %C) has a plane strain fracture toughness, K_{IC}, of 20-28 $MPa\sqrt{m}$[29]. However, unlike the tungsten, these wires were not severely constrained by the matrix. Initially, the wires are in tension and the matrix is in compression due to residual stresses. As the sample is loaded the wires begin to debond, allowing some slippage of the matrix. When the wires begin to break they are not confined to a single plane, but break at various lengths, as shown in Figure 3.35, an SEM photograph of the fracture surface of a 60% V_f music wire/Vitreloy® 1 tensile sample. Cracks through the matrix do not proceed across a flat surface; rather there is also mode II cracking at the fiber/matrix interface and fiber pull out. All of these additional failure mechanisms contribute to energy dissipation and enhancing the toughness of the composite.

Figure 3.35 Backscatter SEM photograph of 60% music wire/Vitreloy® 1 composite tensile fracture surface. Note that the sample contains large variation in fiber length, and vertical delamination of fiber and matrix.

3.5 Conclusions

1. Continuous fiber metallic glass matrix composites may be successfully fabricated.
2. The rule of mixtures model accurately predicts elastic behavior.
3. Compressive failure is controlled by the matrix material.
4. Tightly bonded ductile fibers provide the largest increase in compressive strain to failure.
5. Tightly bonded ductile fiber reinforcement changes the compressive failure mode from the 45 degree shear bands to localized fiber buckling and tilting.
6. Tensile failure is controlled by the reinforcement.
7. Weakly bonded ductile fibers provide the largest increase in tensile strain to failure.
8. Tungsten forms a strong bond with Vitreloy® 1 metallic glass.
9. Shear strength of the steel wire/ Vitreloy® 1 metallic glass bond is ~45 MPa.
10. Viscous flow of the metallic glass matrix material occurs in shear bands.

Bibliography

Chapter 3

1. Peker, A., and Johnson, W.L., Applied Physics Letters, **63**, 2342, (1993).
2. Bruck, H.A., Christman, T., Rosakis, A.J., and Johnson, W.L., Scripta Metallurgica et Materialia, **30**, 429, (1994).
3. He, Y., Schwarz, R.B., Mandrus, D. And Jacobson, L., Journal of Non-Crystalline Solids, **205-207**, 602, (1996)
4. Davis, L.A. and Kavesh, S., Journal of Materials Science, **10**, 453, (1975).
5. Pampillo, C.A., Scripta Metallurgica, **6**, 915, (1972).
6. Cytron, S.J., Journal of Materials Science Letters, **1**, 211, (1982).
7. Vaidya, R.U., and Subramanian, K.N., SAMPE Journal, **29** [4], (1993).
8. Leng, Y. and Courtney, T.H., Metallurgical Transactions A, **21A**, 2159, (1990).
9. Leng, Y., and Courtney, T.H., Journal of Materials Science, **24**, 2006, (1989).
10. Leng, Y., and Courtney, T.H., Journal of Materials Science, **26**, 588, (1991).
11. Boyer, H.E. and Gall, T.L., eds., Metals Handbook, Desk Edition, American Society for Metals, Metals Park, Ohio, (1985).
12. Annual Book of ASTM Standards, **02.05**, ASTM, Philadelphia, (1991).
13. Arsenault, R.J., and Taya, M., Acta Metallurgica, **35** [3], 651, (1987).
14. Delannay, F., Colin, C., Marchal, Y., Tao, L., Boland, F., Cobzaru, P., Lips, B., and Dellis, M.A., Journal de Physique IV, **3**, 1675, (1993).
15. Mikata, Y., and Taya, M., Journal of Composite Materials, **19**, 554, (1985).
16. Warwick, C.M., and Clyne, T.W., Journal of Materials Science, **26**, 3817, (1991).

17. Jessen, T.L., Mecholsky, J.J., and Moore, R.H., American Ceramic Society Bulletin, **65** [2], 377, (1986).

18. Krstic, V.V., Nicholson, P.S., and Hoagland, R.G., Journal of the American Ceramic Society, **64** [9], (1981).

19. Spowart, J.E. and Clyne, T.W., Key Engineering Materials, **127-131**, 833, (1997)

20. Pampillo, C.A. and Chen, H.S., Materials Science and Engineering, **13**, 181, (1974).

21. Pampillo, C.A. and Reimschuessel, A.C., Journal of Materials Science, **9**, 718, (1974).

22. Mecholsky, J.J., Jr., and Powell, S.R., Jr., eds., Fractography of Ceramic and Metal Failures, ASTM STP 827, 7, Philadelphia, (1982).

23. Clyne, T.W. and Withers, P.J., An Introduction to Metal Matrix Composites, Cambridge University Presss, 109, Cambridge, (1995).

24. Warren, P.D., Mackin, T.J. and Evans, A.G., Acta Metallurgica et Materielia , **40** [6], 1243, (1992).

25. Eldridge, J.I., and Brindley, P.K., Journal of Materials Science Letters, **8**, 1451, (1989).

26. Herrera-Franco, P.J., and Drzal, L.T., Composites, **23** [1], 2, (1992).

27. Mutoh, Y., Ichikawa, K. Nagata, K. And Takeuchi, M., Journal of Materials Science, **30** [3], 770, (1995)

28. Ashby, M.F., Blunt, F.J. and Bannister, M., Acta Metallurgica, **37** [7], 1847, (1989).

29. Crane, L.W. and Bigg, A.P., Materials Science and Technology, **6** [10], 993, (1990).

CHAPTER 4

FRACTURE TOUGHNESS DETERMINATION FOR A BERYLLIUM BEARING BULK METALLIC GLASS AND TUNGSTEN WIRE REINFORCED METALLIC GLASS COMPOSITE

4.1 Introduction

A class of beryllium bearing bulk metallic glass alloys has recently been developed at the California Institute of Technology (1993)[1]. These alloys can be fabricated in the form of large ingots with minimum dimensions on the order of centimeters, which allows valid mechanical tests to be performed on these materials. Such tests were not formerly possible given the small dimensions of earlier metallic glass specimens. Some basic physical and mechanical properties have been measured on a specific beryllium bearing bulk metallic glass with a nominal composition of $Zr_{41.25}Ti_{13.75}Cu_{12.5}Ni_{10}Be_{22.5}$[2]. The results of these measurements are listed in Table 3.1. Though possessing remarkably high strength and large elastic strain, this bulk metallic glass (as all metallic glasses) fails in a sudden and catastrophic manner by the propagation of localized shear bands.

Fracture toughness measurements have been performed on Fe and Ni base metallic glass[3,4]. Ribbons of these as-quenched glasses exhibit plane strain fracture toughness (K_{IC}) of about 10 MPa√m. Thickness of these ribbons is limited to ~25 μm, which restricts the type of mechanical tests which may be performed.

In 1995 a concerted effort began at Caltech to fabricate composites using bulk metallic glass as the matrix material. Research has shown that the toughness of brittle materials can be improved through the incorporation of ductile materials[5-7]. The inclusion of ductile metal fibers in metallic glass is hoped to allow the metallic glass to fail in a more predictable and less unfavorable manner.

The purpose of this chapter is twofold: first, to report on the first ever direct measurement of the fracture toughness of any bulk metallic glass system, and second, to describe the preliminary results of fracture toughness measurements of a tungsten reinforced bulk metallic glass composite.

4.2 Sample Preparation

Metallic glass ingots of Vitreloy® 1, the trademark name of the commercial grade beryllium bearing metallic glass with the composition of $Zr_{41.25}Ti_{13.75}Cu_{12.5}Ni_{10}Be_{22.5}$, were obtained from Amorphous Technologies International, located in Laguna Niguel, California. The Vitreloy® is not made with laboratory grade materials, and, as a result, contains a higher percentage of impurities than the metallic glass prepared using laboratory grade materials. It is believed that the impurities, particularly the oxides, act as nucleation sites for a small fraction of crystalline phase to form in the glass. The effect of the small percentage of crystalline phase on the toughness of the metallic glass is unknown. The specimens were machined to the dimensions shown in Table 4.1.

The tungsten reinforced Vitreloy® 1 matrix composite was fabricated using the infiltration casting technique described in Chapter 3. A 50% volume fraction (V_f) of cleaned and straightened tungsten wire was placed in a 25 mm diameter quartz tube. A neck was formed in the tube above the wires, and commercial Vitreloy® 1 ingots were added. The remaining casting procedure was as previously described. Following casting, the ingot was sliced using electrical discharge machining to provide 3-point bend test specimens with the dimensions shown in table 4.1. The tungsten wires were oriented along the length of the sample, perpendicular to the notch.

4.3 Experimental Procedure

The Mode-I fracture toughness of the unreinforced metallic glass was measured by simultaneous use of two independent techniques. The optical method of CGS[8] and boundary value measurement. The sample used in conjunction with CGS measurement was ground optically flat and polished to a highly reflective finish.

The Mode-I fracture toughness of the 50% V_f tungsten/Vitreloy® 1 matrix composite was taken using boundary value measurement in 3-point bend configuration. It is recognized that, because this is a composite material, the method of calculating K_{IC} differs from that used for an isotropic material, and the value reported here is in error. However, the result of interest here is the change in the mode of failure, rather than the value of K_{IC}. Further experiments will be performed to refine the measured fracture toughness.

4.3.1 Boundary Value Measurements

Mode I fracture toughness, K_{IC}, was determined using boundary measurements taken from specimen loading in 3-point bending configuration. Specimens were loaded until failure, and the corresponding K_{IC} value was calculated from[9]

$$K_I = \frac{P}{B\sqrt{W}} \frac{3\frac{S}{W}\sqrt{\frac{a}{W}}}{2\left(1+2\frac{a}{W}\right)\left(1-\frac{a}{W}\right)^{\frac{3}{2}}} \left[1.99 - \frac{a}{W}\left(1-\frac{a}{W}\right)\left\{2.15 - 3.93\left(\frac{a}{W}\right) + 2.7\left(\frac{a}{W}\right)^2\right\}\right] \quad (1)$$

The applied load is P, and dimensions a, W, B and S are defined in Table 4.1.

Dimension (mm)	**Boundary-value sample**	**CGS sample**
Length, L	50.8	112
Width, W	12.6	40.8
Thickness, B	2.2	4.8
Notch length, a	3	11.6
Loading span, S	46	104.2

Table 4.1 Fracture sample dimensions

Figure 4.1 illustrates the typical variation of K_I with load point displacement δ for unreinforced Vitreloy® 1, which has a peak value, K_{IC} = 59.5 MPa√m. It is interesting to note that the loading curve remains approximately linear up until failure, suggesting limited inelasticity. At failure, the crack propagation is unstable, indicated by the instantaneous unloading of the specimen. Results obtained from experiments conducted on 3 samples gave consistent K_{IC} values of 55, 57 and 59.5 MPa√m. For valid plane strain fracture toughness testing, the specimen thickness must be greater than $2.5(K_{IC}/\sigma_o)^2$, where σ_o is the yield stress. Typical values for the metallic glass of K_{IC}~57 MPa√m and σ_o~2 GPa, requires that the specimen thickness be greater than ~1.6 mm for plane strain conditions. Specimens used in the present study were at least 2.2 mm thick and therefore the results reported represent the plane strain fracture toughness of the metallic glass.

Five composite specimens were tested in the 3-point bend configuration. The results are depicted in Figure 4.2. There was substantial scatter in the results; the high value was 38 MPa√m, and the low was 18 MPa√m. Three specimens failed at the average

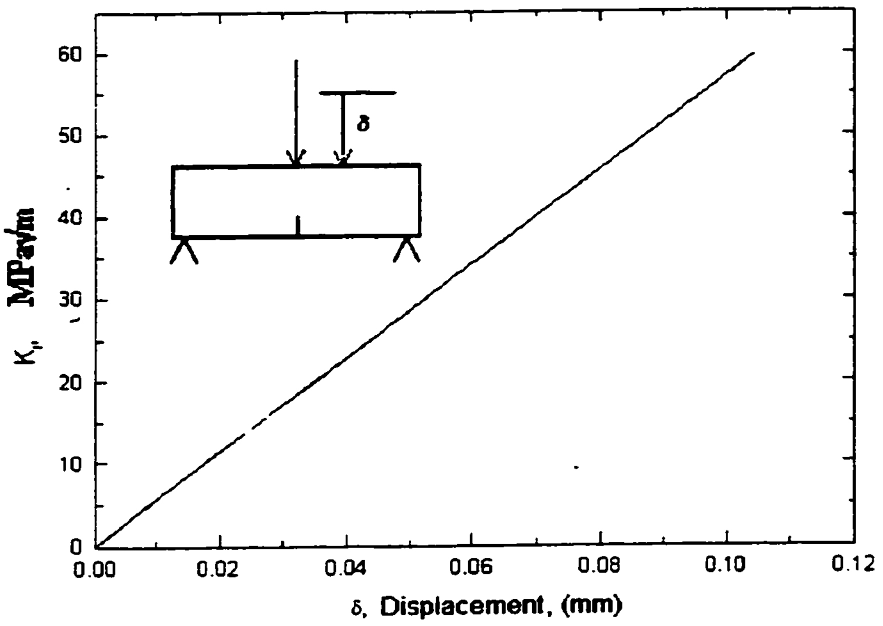

Figure 4.1 The variation of K_I with load point displacement for an unreinforced Vitreloy® 1 specimen loaded quasi-statically in a three point bend configuration.

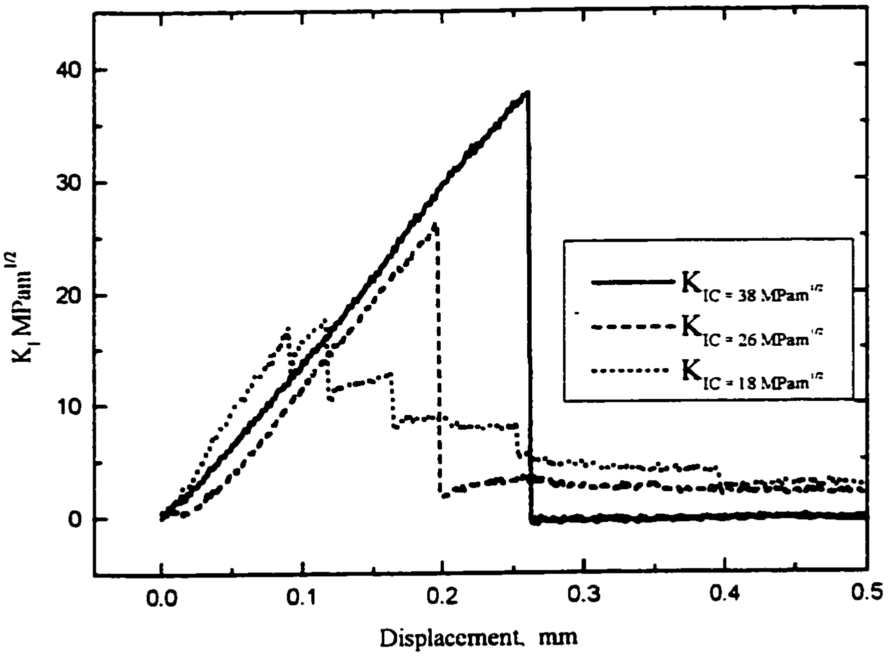

Figure 4.2 K_I versus displacement of 50% V_f tungsten/Vitreloy® 1 matrix composite.

K_{IC} value of 26 MPa√m. Even though the calculated values are in error in the composite material, these values are still significantly lower than those of the unreinforced metallic glass. The K_I value for the sample that failed at the highest load (K_{IC} = 38) instantly dropped to zero, indicating unstable crack growth. By comparison, the sample that failed at K_{IC} = 18 continued to sustain a load after initial failure. Despite a difference in excess of 50% in K_{IC} between these two curves, the area under the curves differs by less than 5% (as determined by numerical integration).

4.3.2 Coherent Gradient Sensing (CGS)

CGS is a full field, lateral shearing interferometric technique with an on-line spatial filter. In the reflection mode the technique measures out-of-plane displacement gradients (surface slopes). When the sample is loaded the surface deforms in the region near the crack tip, causing nonuniform spatial gradients in the optical path when light is reflected from its surface. The changes in the optical path are related to gradients in the stress state which are induced when loads are applied to the boundary of the initially undeformed specimen.

The schematic of the experimental setup used for reflective CGS is shown in Figure 4.3. An optically flat, highly reflective plate specimen is illuminated by collimated coherent laser light. The reflected beam is then incident on a pair of gratings (40 lines/mm), G_1 and G_2, separated by a distance Δ. The field distribution on the G_2 plane is spatially filtered by the filtering lens L_1 and its frequency content is displayed on its back focal plane. By locating a filtering aperture around either the ±1 diffraction orders, information regarding the stress gradients is obtained on the image plane of the lens L_2. Complete details of the technique are given elsewhere[8].

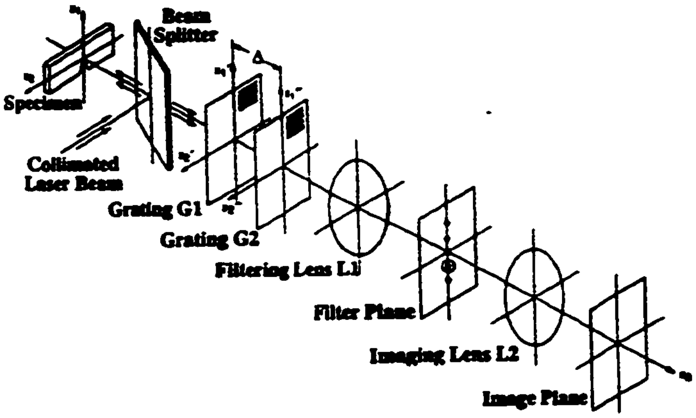

Figure 4.3 Schematic illustration of the experimental configuration for coherent gradient sensing (CGS) in reflection.

Figure 4.4 is a photograph of CGS interference fringes on the Vitreloy sample immediately prior to failure. The individual fringes in Fig. 4.4 represent contours of $\partial u_3 / \partial x_1$. By measuring the values of the local polar coordinates r and ϕ for a specific fringe order, the out of plane deformations, and hence K_I, may be calculated from:

$$\frac{\partial u_3}{\partial x_1} = \frac{v h}{2E} \frac{K_1}{\sqrt{2\pi}} r^{-\frac{3}{2}} \cos\left(\frac{3}{2}\phi\right) = \frac{mp}{2\Delta} \qquad (2)$$

where u_3 is the deformation normal to the plane of the specimen, x_1 is the in-plane direction aligned with the crack, v is Poissons ratio, h is the plate thickness, E is Young's modulus, m represents the fringe order, p is the diffraction grating pitch and Δ is the grating spacing. Measurements taken from Fig. 4.4 provided a fracture toughness of

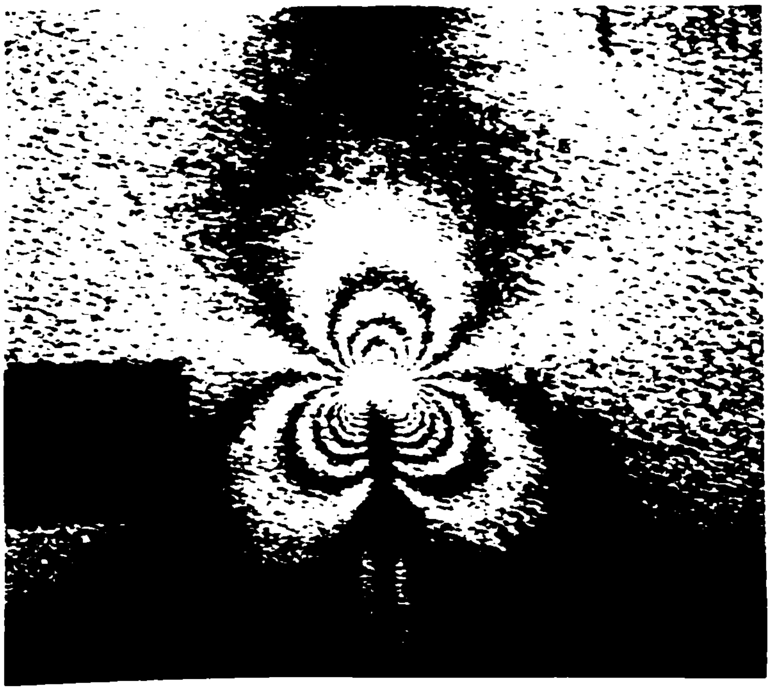

Figure 4.4 CGS pattern recorded from a metallic glass specimen loaded in three point bend.

$K_{IC} = 55\ MPa\sqrt{m}$. Figure 4.5 is a plot of K_I calculated from boundary measurements versus K_I measured from CGS. Note that these values are in agreement within 10%.

4.4 Results and Discussion

4.4.1 Unreinforced $Zr_{41.25}Ti_{13.75}Cu_{12.5}Ni_{10}Be_{22.5}$ Bulk Metallic Glass

Given the extremely high yield stress and failure strength of Vitreloy® 1, one might have expected the fracture toughness to be comparable to that of brittle ceramic materials. Such brittle solids have fracture toughness' typically less than 10 $MPa\sqrt{m}$ and, as shown in Table 4.2, compare very unfavorably to structural metals (e.g. steels, aluminum, titanium) whose toughness' exceed 30 $MPa\sqrt{m}$. The Vitreloy, however, exhibits toughness comparable to many high strength steels and approaches that of some titanium alloys.

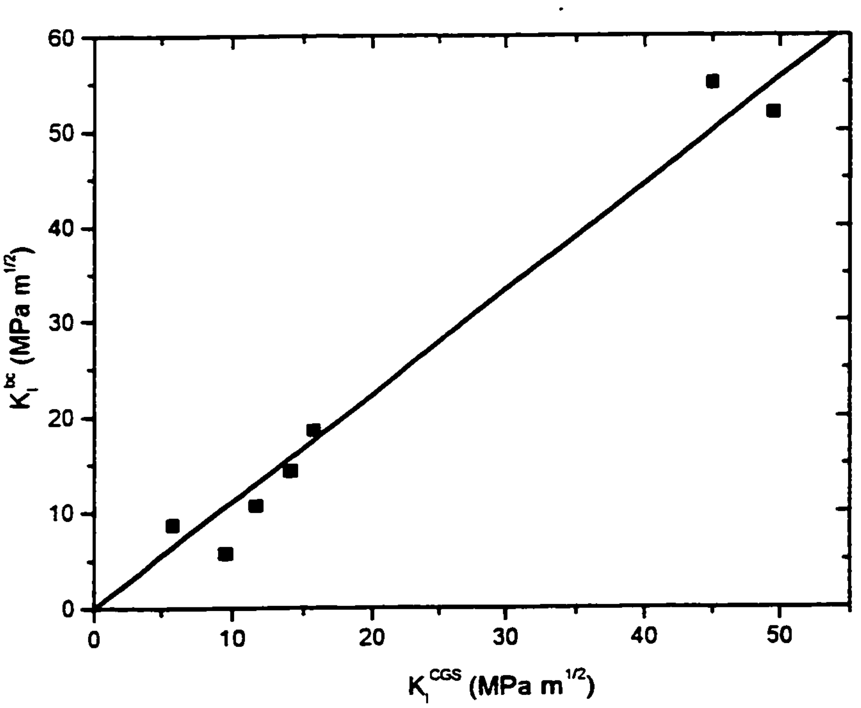

Figure 4.5 Comparison of the stress intensity factor determined from boundary value measurements with that determined using CGS.

Material	Fracture Toughness, MPa$\sqrt{m}$
Vitreloy 1® ($Zr_{41.25}Ti_{13.75}Cu_{12.5}Ni_{10}Be_{22.5}$) bulk metallic glass	55-59
Ti 6Al-4V (mill anneal plate)	123
Polycarbonate	2.75-3.3
C300 maraging steel	60
2024 aluminum, T351	31-44
Al_2O_3	3-5.5
SiN_4	4.2-5.2
Electrical porcelain ceramics	1.03-1.25

Table 4.2 Fracture toughness of selected engineering materials[10].

The high fracture toughness of unreinforced Vitreloy® 1 points toward some microscopic toughening mechanisms. In ideally brittle fracture, the critical energy release rate under plane strain conditions, $G_{IC} = (1-v^2)K_{IC}^2/E$ simply equals the energy to create two free surfaces, $2\gamma_s$. Assuming brittle fracture, the apparent surface energy of the metallic glass can be estimated. Using K_{IC}~57 MPa√m, E = 96 GPa and ν = 0.36, the calculated apparent surface energy is almost 30,000 Jm^{-2}. This apparent surface energy for the metallic glass is exceedingly high in comparison to measured surface energies of ceramics and pure metals which are typically 0.5-10 Jm^{-2}. This high apparent value of the surface energy may suggest the operation of other mechanisms in addition to surface creation that would contribute to a high net energy release rate.

Optical and scanning electron microscopy were used to investigate the microstructural processes associated with fracture in the metallic glass. Figure 4.6 shows a scanning electron micrograph of the fracture surface of a metallic glass specimen. The relatively smooth area on the left of the micrograph is the surface of the initial notch, whereas as the rougher region on the right side of micrograph is the fracture surface. In Fig. 4.6 there is no evidence of macroscopic shear lips adjacent to the plate specimen surfaces. The local roughness on the fracture surface is on the order of 50-150 μm. Figure 4.7 shows a optical micrograph of the crack profile of the mating half of the specimen shown in Fig. 4.6. The initial notch is located on the left of the micrograph. The small bright regions in the micrograph are crystalline particles which are embedded in the bulk metallic glass. Most crystallites in the region near the initial notch and adjacent to the crack path contain microcracks in the direction parallel to macroscopic crack growth (perpendicular to the direction of tensile loads induced by the crack). In some cases, crystallites located in the vicinity of the crack path were also surrounded by apparent

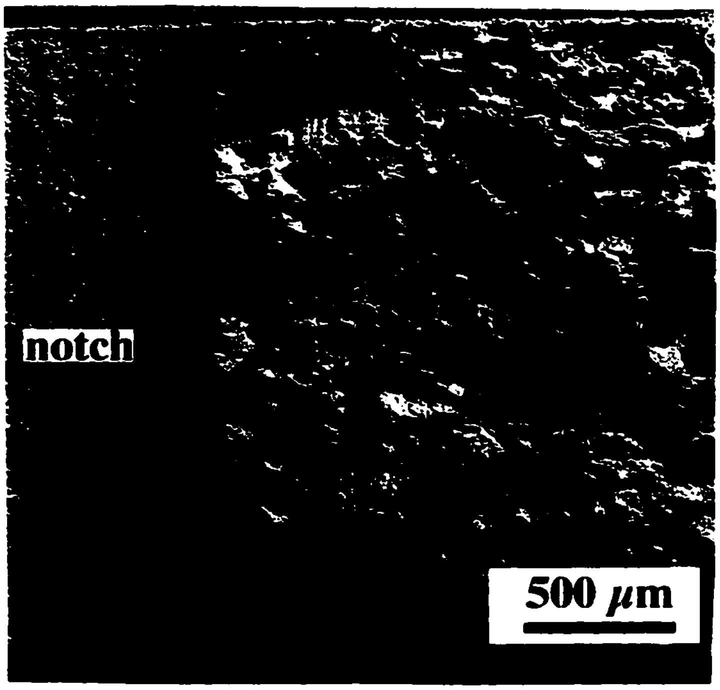

Figure 4.6 Scanning electron micrograph of the fracture surface of a metallic glass specimen. The initial notch is located to the left of the image.

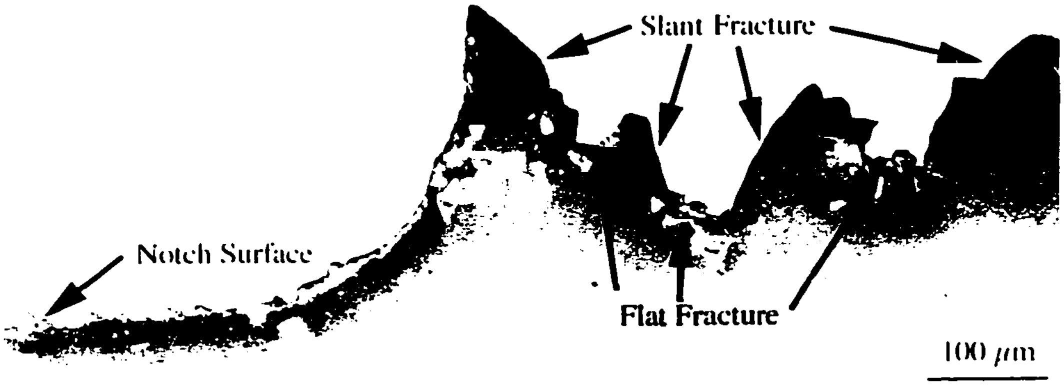

Figure 4.7 Optical micrograph of the crack profile from the mating half of metallic glass specimen shown in Fig. 4.6. Regions of both slant fracture and flat fracture are observed. The initial notch is on the left of the micrograph.

microvoids. As illustrated in Fig. 4.7, the crack path exhibits essentially flat regions parallel to the macroscopic crack path and surfaces angled at 45° with respect to the crack path. Inspection of these regions along the entire length of the fracture surface indicated that the flat regions were often associated with the presence of fractured crystallites, whereas the ligaments in the region between the crystallites angled at 45° are reminiscent of void sheet formation in ductile metals. The maximum extent of the plane strain plastic zone size, r_p, was estimated using the following relation

$$r_p\left(\frac{\pi}{2}\right) = \frac{1}{4\pi}\left(\frac{K_{IC}}{\sigma_o}\right)^2\left[(1-2\nu)^2 + \frac{3}{2}\right] \approx 0.126\left(\frac{K_{IC}}{\sigma_o}\right)^2 \qquad (3)$$

which resulted in a value of r_p=102 μm. The calculated plastic zone size is approximately equivalent in size to the fracture surface roughness shown in Fig. 4.6.

4.4.2 Tungsten Reinforced Vitreloy® 1 Matrix Composite

The tungsten reinforced metallic glass composite failed at a substantially lower K$_{IC}$ value than the unreinforced material. As may be seen from figure 4.2, the sample with the highest K$_{IC}$ value failed in an unstable manner, while failure of the sample with the lowest K$_{IC}$ value was less catastrophic. Because the displacement of the sample with the highest K$_{IC}$ value (~0.27 mm) was 3 times larger than that of the sample for which K$_{IC}$ = 18 MPa√m , far more elastic energy was available to propagate the crack.

There are two primary mechanisms for toughening a brittle material: ductile deformation of the fibers, and fiber pullout. Neither of these mechanisms are present in the tungsten reinforced composite. Figure 4.8 is an SEM micrograph of the fracture surface around the notch in the specimen. The plane strain fracture toughness of tungsten is only 12-14 MPa√m, and the brittle manner in which the fibers failed is evident by the relatively smooth fracture surface of the wires. Tungsten has a lower CTE than the metallic glass matrix, resulting in significant compressive stress on the wire upon cooling. Tungsten also wets well and bonds tightly to the metallic glass matrix. As a result there is no fiber pullout to dissipate energy. The high density of brittle wires along the edge of the notch also lowered the load at which fracture initiated.

Figure 4.8 Fracture surface of 50% V_f tungsten/Vitreloy® 1 matrix composite. Region on left is the notch. Note the brittle fracture of the wires, and the lack of fiber pullout.

Despite the lack of toughness of the composite material compared to the unreinforced metallic glass, the presence of wires did arrest crack propagation. Figure 4.9

is a photograph of a composite 3-point bend specimen. The unreinforced metallic glass broke cleanly into two pieces when it fractured. The crack in the composite, however, was arrested by the metal wires. This reinforces the idea that the proper choice of ductile reinforcement and control of the interface bond strength can result in a metallic glass matrix composite which has enhanced fracture properties compared to the unreinforced material.

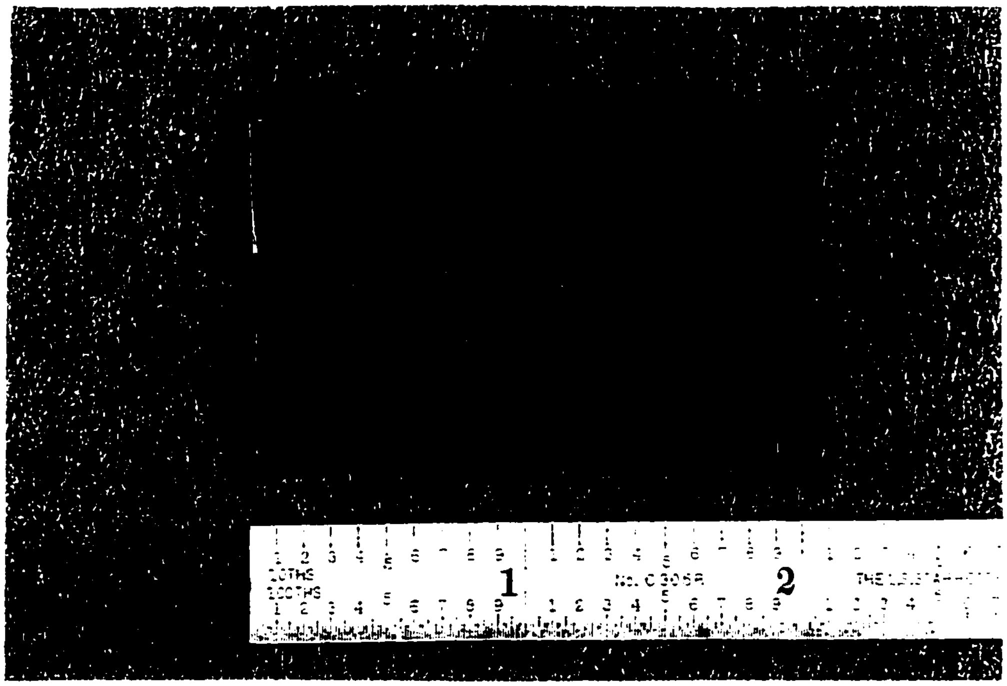

Figure 4.9 Photograph of composite 3-point bend specimens. Crack in bottom specimen was arrested by the reinforcing tungsten wires.

4.5 Conclusions

1. Coherent Gradient Sensing may be accurately used to evaluate the toughness of bulk metallic glass.
2. The plane strain fracture toughness of Vitreloy® 1 bulk metallic glass is 55 MPa√m.

3. Crack growth in Vitreloy® 1 is unstable.
4. Ductile reinforcement will arrest crack growth in bulk metallic glass matrix composites.

Bibliography

Chapter 4

1. Peker, A and Johnson, W. L., Applied Physics Letters, **63**, 2342, (1993).
2. Bruck, H. A., Christman, T., Rosakis, A. J., Johnson, W. L., Scripta Metallurgica et Materialia, **30**, 429, (1994).
3. Davis, L.A., Metallurgical Transactions A, **10A**, 235, (1972).
4. Ocelik, V., Diko, P., Hajko, V., Jr., Miskuf, J., and Duhaj, P., Journal of Materials Science, **22**, 2305, (1987).
5. Bannister, M., Shercliff, H., Bao, G., Zok, F., and Ashby, M.F., Acta Metallurgica et Materialia, **40** [7], 1531, (1992).
6. Baran, G., Degrange, M., Roques-Carmes, C., and Wehbi, D., Journal of Materials Science, **25**, 4211, (1990).
7. Lee, T.K. and Subramanian, K.N., Journal of Materials Science, **30**, 2401, (1995).
8. Rosakis, A. J., in Experimental Techniques in Fracture, (J.S. Epstein, ed.), 327, VCH Publishers, New York, (1993).
9. Anderson, T. L., Fracture Mechanics, Fundamentals and Applications, 713, CRC Press, Inc., Boca Raton, (1991).
10. Hertzberg, R. W., Deformation and Fracture Mechanics of Engineering Materials, 3rd ed., John Wiley & Sons, New York, (1988).

APPENDIX I

COAXIAL CYLINDER MODEL
FOR THE
CALCULATION OF FIBER COMPOSITE STRESS

This is a program to calculate matrix and fiber stress in a continuous fiber composite using the coaxial cylinder model.

$Ef = 410\cdot 10^{9}$ **Fiber Elastic Modulus**

$\nu_1 = 0.28$ **Fiber Poisson Ratio**

$\alpha_1 = 4.5\cdot 10^{-6}$ **Fiber CTE**

$Em = 96\cdot 10^{9}$ **Matrix Elastic Modulus**

$\nu_2 = 0.36$ **Matrix Poisson Ratio**

$\alpha_2 = 8.5\cdot 10^{-6}$ **Matrix CTE**

$\Delta T = -350$ **Temperature Change, (Tf - Ti)**

$\kappa_1 = \left[1-\left(\nu_1\right)^2\right]^2-\left[\nu_1+\left(\nu_1\right)^2\right]^2$

The following lines calculate the elastic constants for the fiber and matrix stiffness matricies, Cf and Cm, respectively

$\kappa_1 = 0.721$

$\kappa_2 = \left[1-\left(\nu_2\right)^2\right]^2-\left[\nu_2+\left(\nu_2\right)^2\right]^2$

$\kappa_2 = 0.518$

$$Cf_{11} = \frac{Ef\cdot\left[1-\left(\nu_1\right)^2\right]}{\kappa_1}$$

$Cf_{33} = Cf_{11}$

$$Cf_{12} = \frac{Ef\cdot\nu_1\cdot\left(1+\nu_1\right)}{\kappa_1}$$

$Cf_{13} = Cf_{12}$

$$Cm_{11} = \frac{Em\cdot\left[1-\left(\nu_2\right)^2\right]}{\kappa_2}$$

$Cm_{33} = Cm_{11}$

$$Cm_{12} = \frac{Em\cdot\nu_2\cdot\left(1+\nu_2\right)}{\kappa_2}$$

$Cm_{13} = Cm_{12}$

$r_1 = 125\cdot 10^{-6}$ $r_2 = 200\cdot 10^{-6}$ **These are the fiber and matrix radius, respectively**

The following "aii" and "bii"constants are used in calculating the equations of elasticity

$a_{11} = r_1$

$a_{12} = -r_1$

$a_{13} = -\frac{1}{r_1}$

$a_{21} = 0$

$a_{22} = Cm_{11} + Cm_{12}$

$a_{23} = \frac{Cm_{12} - Cm_{11}}{(r_2)^2}$

$a_{24} = Cm_{13}$

$a_{31} = Cf_{11} + Cf_{12}$

$a_{32} = -(Cm_{11} + Cm_{12})$

$a_{33} = -\frac{Cm_{12} - Cm_{11}}{(r_1)^2}$

$a_{34} = (Cf_{13} - Cm_{13})$

$a_{41} = 2 \cdot Cf_{13} \cdot (r_1)^2$

$a_{42} = 2 \cdot Cm_{13} \cdot \left[(r_2)^2 - (r_1)^2 \right]$

$a_{43} = 0$

$a_{44} = Cf_{33} \cdot (r_1)^2 + Cm_{33} \cdot \left[(r_2)^2 - (r_1)^2 \right]$

$\beta_1 = (2 \cdot Cf_{12} + Cf_{11}) \cdot \alpha_1$

$\beta_2 = (2 \cdot Cm_{12} + Cm_{11}) \cdot \alpha_2$

$\sigma_{01} = 0$ $\sigma_{03} = 0$

These are initial stresses in the radial (01) and axial (03) directions

$b_1 = 0$

$b_2 = \sigma_{01} + \beta_2 \cdot \Delta T$

$b_3 = \Delta T \cdot (\beta_1 - \beta_2)$

$b_4 = \sigma_{03} \cdot (r_2)^2 + \Delta T \cdot \left[\beta_1 \cdot (r_1)^2 + \beta_2 \cdot \left[(r_2)^2 - (r_1)^2 \right] \right]$

$$Y := \begin{bmatrix} a_{11} & a_{12} & a_{13} & a_{14} \\ a_{21} & a_{22} & a_{23} & a_{24} \\ a_{31} & a_{32} & a_{33} & a_{34} \\ a_{41} & a_{42} & a_{43} & a_{44} \end{bmatrix}$$

$$Y = \begin{bmatrix} 1.25\cdot 10^{-4} & -1.25\cdot 10^{-4} & -8\cdot 10^{3} & 0 \\ 0 & 2.521\cdot 10^{11} & -1.765\cdot 10^{18} & 9.076\cdot 10^{10} \\ 7.28\cdot 10^{11} & -2.521\cdot 10^{11} & 4.518\cdot 10^{18} & 1.131\cdot 10^{11} \\ 6.37\cdot 10^{3} & 4.424\cdot 10^{3} & 0 & 1.212\cdot 10^{4} \end{bmatrix}$$

$$Z := \begin{bmatrix} b_1 \\ b_2 \\ b_3 \\ b_4 \end{bmatrix}$$

$$Z = \begin{bmatrix} 0 \\ -1.02\cdot 10^{9} \\ -4.476\cdot 10^{8} \\ -47.794 \end{bmatrix}$$

$$X := Y^{-1}\cdot Z$$

Using the a's and b's to solve for the unknown X

$$X = \begin{bmatrix} -0.002 \\ -0.003 \\ 2.504\cdot 10^{-11} \\ -0.002 \end{bmatrix}$$

Assigning values to the X's to solve the stress equations

$A_1 := X_0$

$A_2 := X_1$

$B_2 := X_2$ $\qquad B_1 := 0$

$E := X_3$

$r := 25 \cdot 10^{-6}, 50 \cdot 10^{-6} .. 125 \cdot 10^{-6}$

This set solves for the radial, hoop and axial stress in the fiber

$$\sigma rr(r) := Cf_{11} \cdot \left(A_1 - \frac{B_1}{r^2}\right) + Cf_{12} \cdot \left(A_1 + \frac{B_1}{r^2}\right) + Cf_{13} \cdot E - \beta_1 \cdot \Delta T$$

These are the radial stresses in the fiber, beginning at the center and progressing outward.

$\sigma rr(r)$
$-6.893 \cdot 10^{7}$
$-6.893 \cdot 10^{7}$
$-6.893 \cdot 10^{7}$
$-6.893 \cdot 10^{7}$
$-6.893 \cdot 10^{7}$

$$\sigma \theta \theta(r) := Cf_{11} \cdot \left(A_1 + \frac{B_1}{r^2}\right) + Cf_{12} \cdot \left(A_1 - \frac{B_1}{r^2}\right) + Cf_{13} \cdot E - \beta_1 \cdot \Delta T$$

These are the hoop stresses in the fiber, beginning at the center and progressing outward.

$\sigma \theta \theta(r)$
$-6.893 \cdot 10^{7}$
$-6.893 \cdot 10^{7}$
$-6.893 \cdot 10^{7}$
$-6.893 \cdot 10^{7}$
$-6.893 \cdot 10^{7}$

$$\sigma zz(r) := 2 \cdot Cf_{13} \cdot A_1 + Cf_{33} \cdot E - \beta_1 \cdot \Delta T$$

These are the axial stresses in the fiber, beginning at the center and progressing outward.

$\sigma zz(r)$
$-2.002 \cdot 10^{8}$
$-2.002 \cdot 10^{8}$
$-2.002 \cdot 10^{8}$
$-2.002 \cdot 10^{8}$
$-2.002 \cdot 10^{8}$

Finally, we can use the calculated stresses to compute the Von Mises stresses:

$$\sigma vmf := \sqrt{\frac{(\sigma rr(1) - \sigma \theta \theta(1))^2 + (\sigma \theta \theta(1) - \sigma zz(1))^2 + (\sigma zz(1) - \sigma rr(1))^2}{2}}$$

$\sigma vmf = 1.313 \cdot 10^{8}$

$2.2\cdot 10^{9} - \sigma vmf = 2.069\cdot 10^{9}$

This is how far below yield the fiber is. If it is negative, the fiber has reached yield. The yield strength of the fiber is, in this case, taken to be 2.2 GPa.

$r := 125\cdot 10^{-6}, 143.75\cdot 10^{-6} .. 200\cdot 10^{-6}$

This is the radius of the matrix surrounding the fiber

$$\sigma rr(r) := Cm_{11}\cdot\left(A_2 - \frac{B_2}{r^2}\right) + Cm_{12}\cdot\left(A_2 + \frac{B_2}{r^2}\right) + Cm_{13}\cdot E - \beta_2\cdot\Delta T$$

$\sigma rr(r)$
$-6.893\cdot 10^{7}$
$-4.135\cdot 10^{7}$
$-2.275\cdot 10^{7}$
$-9.615\cdot 10^{6}$
$-1.192\cdot 10^{-7}$

This is the matrix radial stress, beginning at the fiber and progressing outward.

$$\sigma\theta\theta(r) := Cm_{11}\cdot\left(A_2 + \frac{B_2}{r^2}\right) + Cm_{12}\cdot\left(A_2 - \frac{B_2}{r^2}\right) + Cm_{13}\cdot E - \beta_2\cdot\Delta T$$

$\sigma\theta\theta(r)$
$1.573\cdot 10^{8}$
$1.297\cdot 10^{8}$
$1.111\cdot 10^{8}$
$9.799\cdot 10^{7}$
$8.837\cdot 10^{7}$

These are the hoop stresses in the matrix as a result of cooling; they begin at the fiber and progress outward.

$$\sigma zz(r) := 2\cdot Cm_{13}\cdot A_2 + Cm_{33}\cdot E - \beta_2\cdot\Delta T$$

$\sigma zz(r)$
$1.284\cdot 10^{8}$
$1.284\cdot 10^{8}$
$1.284\cdot 10^{8}$
$1.284\cdot 10^{8}$
$1.284\cdot 10^{8}$

These are the axial stresses in the matrix, beginning at the fiber and progressing outward.

$$\sigma rrave := \frac{\sigma rr\left(125\cdot 10^{-6}\right) + \sigma rr\left(150\cdot 10^{-6}\right) + \sigma rr\left(175\cdot 10^{-6}\right) + \sigma rr\left(200\cdot 10^{-6}\right) + \sigma rr\left(225\cdot 10^{-6}\right)}{5}$$

$\sigma rrave = -2.151 \cdot 10^{7}$ **This is the average radial stress in the matrix**

$$\sigma\theta\theta ave = \frac{\sigma\theta\theta(125 \cdot 10^{-6}) + \sigma\theta\theta(150 \cdot 10^{-6}) + \sigma\theta\theta(175 \cdot 10^{-6}) + \sigma\theta\theta(200 \cdot 10^{-6}) + \sigma\theta\theta(225 \cdot 10^{-6})}{5}$$

$\sigma\theta\theta ave = 1.099 \cdot 10^{8}$ **This is the average hoop stress in the matrix**

$\sigma zz(1) = 1.284 \cdot 10^{8}$ **This is the average longitudinal stress in the matrix**

This is the Von Mises stress for the matrix:

$$\sigma vmm = \sqrt{\frac{(\sigma rrave - \sigma\theta\theta ave)^{2} + (\sigma\theta\theta ave - \sigma zz(1))^{2} + (\sigma zz(1) - \sigma rrave)^{2}}{2}}$$

$\sigma vmm = 1.415 \cdot 10^{8}$

APPENDIX II

ESHELBY EQUIVALENT INCLUSION METHOD

FOR THE

CALCULATION OF PARTICULATE COMPOSITE STRESS

This is a program to calculate the stresses in a particulate composite using Eshelby's method.

First, enter the material constants;

$\mathrm{Em} := 96\cdot 10^{9}$ **Youngs modulus for the matrix**

$\mathrm{Ef} := 410\cdot 10^{9}$ **Fiber modulus**

$\mathrm{vm} := .36$ **Matrix and fiber poisson ratio**

$\mathrm{vf} := 0.28$

$\alpha\mathrm{m} := 8.5\cdot 10^{-6}$ **Matrix and fiber thermal expansion, per degree C**

$\alpha\mathrm{f} := 4.5\cdot 10^{-6}$

$\Delta\mathrm{T} := -350$ **Temperature through which cooling occurs, below Tg**

$\varepsilon\mathrm{tstar} := (\alpha\mathrm{f} - \alpha\mathrm{m})\cdot\Delta\mathrm{T}$ **This is thermal strain resulting from cooling**

$$\mathrm{Etstar} := \begin{bmatrix} \varepsilon\mathrm{tstar} \\ \varepsilon\mathrm{tstar} \\ \varepsilon\mathrm{tstar} \\ 0 \\ 0 \\ 0 \end{bmatrix} \qquad \mathrm{Etstar} = \begin{bmatrix} 0.001 \\ 0.001 \\ 0.001 \\ 0 \\ 0 \\ 0 \end{bmatrix}$$

This is the thermal strain vector

Now, define compliance matricies for the matrix and reinforcement

$\mathrm{I} := \mathrm{identity}(6) \qquad \mathrm{Cm} := \mathrm{identity}(6) \qquad \mathrm{Cf} := \mathrm{identity}(6)$

$$\mathrm{Cm}_{1,1} := \mathrm{Em}\cdot\frac{1 - \mathrm{vm}}{(1 - 2\cdot\mathrm{vm})\cdot(1 + \mathrm{vm})}$$

$\mathrm{Cm}_{2,2} := \mathrm{Cm}_{1,1} \qquad \mathrm{Cm}_{3,3} := \mathrm{Cm}_{1,1}$

$$\mathrm{Cm}_{4,4} := \frac{\mathrm{Em}}{2\cdot(1 + \mathrm{vm})}$$

$\mathrm{Cm}_{5,5} := \mathrm{Cm}_{4,4} \qquad \mathrm{Cm}_{6,6} := \mathrm{Cm}_{4,4}$

$$\mathrm{Cm}_{1,2} := \mathrm{Em}\cdot\frac{\mathrm{vm}}{(1 - 2\cdot\mathrm{vm})\cdot(1 + \mathrm{vm})}$$

$\mathrm{Cm}_{1,3} := \mathrm{Cm}_{1,2} \qquad \mathrm{Cm}_{2,1} := \mathrm{Cm}_{1,2} \qquad \mathrm{Cm}_{2,3} := \mathrm{Cm}_{1,2} \qquad \mathrm{Cm}_{3,1} := \mathrm{Cm}_{1,2} \qquad \mathrm{Cm}_{3,2} := \mathrm{Cm}_{1,2}$

$$\mathrm{Cf}_{1,1} := \mathrm{Ef}\cdot\frac{1 - \mathrm{vf}}{(1 - 2\cdot\mathrm{vf})\cdot(1 + \mathrm{vf})}$$

$\mathrm{Cf}_{2,2} := \mathrm{Cf}_{1,1} \qquad \mathrm{Cf}_{3,3} := \mathrm{Cf}_{1,1}$

$$Cf_{4,4} = \frac{Ef}{2 \cdot (1 + vf)}$$

$$Cf_{5,5} = Cf_{4,4} \qquad Cf_{6,6} = Cf_{4,4}$$

$$Cf_{1,2} = Ef \cdot \frac{vf}{(1 - 2 \cdot vf) \cdot (1 + vf)}$$

$$Cf_{1,3} = Cf_{1,2} \qquad Cf_{2,1} = Cf_{1,2} \qquad Cf_{2,3} = Cf_{1,2} \qquad Cf_{3,1} = Cf_{1,2} \qquad Cf_{3,2} = Cf_{1,2}$$

$$I = \begin{bmatrix} 1 & 0 & 0 & 0 & 0 & 0 \\ 0 & 1 & 0 & 0 & 0 & 0 \\ 0 & 0 & 1 & 0 & 0 & 0 \\ 0 & 0 & 0 & 1 & 0 & 0 \\ 0 & 0 & 0 & 0 & 1 & 0 \\ 0 & 0 & 0 & 0 & 0 & 1 \end{bmatrix}$$

$$Cm = \begin{bmatrix} 1.613 \cdot 10^{11} & 9.076 \cdot 10^{10} & 9.076 \cdot 10^{10} & 0 & 0 & 0 \\ 9.076 \cdot 10^{10} & 1.613 \cdot 10^{11} & 9.076 \cdot 10^{10} & 0 & 0 & 0 \\ 9.076 \cdot 10^{10} & 9.076 \cdot 10^{10} & 1.613 \cdot 10^{11} & 0 & 0 & 0 \\ 0 & 0 & 0 & 3.529 \cdot 10^{10} & 0 & 0 \\ 0 & 0 & 0 & 0 & 3.529 \cdot 10^{10} & 0 \\ 0 & 0 & 0 & 0 & 0 & 3.529 \cdot 10^{10} \end{bmatrix}$$

$$Cf = \begin{bmatrix} 5.241 \cdot 10^{11} & 2.038 \cdot 10^{11} & 2.038 \cdot 10^{11} & 0 & 0 & 0 \\ 2.038 \cdot 10^{11} & 5.241 \cdot 10^{11} & 2.038 \cdot 10^{11} & 0 & 0 & 0 \\ 2.038 \cdot 10^{11} & 2.038 \cdot 10^{11} & 5.241 \cdot 10^{11} & 0 & 0 & 0 \\ 0 & 0 & 0 & 1.602 \cdot 10^{11} & 0 & 0 \\ 0 & 0 & 0 & 0 & 1.602 \cdot 10^{11} & 0 \\ 0 & 0 & 0 & 0 & 0 & 1.602 \cdot 10^{11} \end{bmatrix}$$

Now, calculate the Eshelby S-tensor

$S = \text{identity}(6)$ **Initialize the S-tensor**

$$S_{1,1} = \frac{7 - 5 \cdot vm}{15 \cdot (1 - vm)}$$

$$S_{2,2} = S_{1,1}$$

$$S_{3,3} = S_{1,1}$$

$$S_{1,2} = \frac{-1-5\cdot vm}{15\cdot(1-vm)}$$

$$S_{2,1} = S_{1,2}$$

$$S_{1,3} = S_{1,2}$$

$$S_{2,3} = S_{1,3}$$

$$S_{3,1} = S_{1,3}$$

$$S_{3,2} = S_{3,1}$$

$$S_{4,4} = \frac{4-5\cdot vm}{15\cdot(1-vm)}$$

$$S_{5,5} = S_{4,4}$$

$$S_{6,6} = S_{5,5}$$

$$S = \begin{bmatrix} 0.542 & 0.083 & 0.083 & 0 & 0 & 0 \\ 0.083 & 0.542 & 0.083 & 0 & 0 & 0 \\ 0.083 & 0.083 & 0.542 & 0 & 0 & 0 \\ 0 & 0 & 0 & 0.229 & 0 & 0 \\ 0 & 0 & 0 & 0 & 0.229 & 0 \\ 0 & 0 & 0 & 0 & 0 & 0.229 \end{bmatrix}$$

Now the physical constants can be calculated for the fiber fraction, f. Cc: composite stiffness E3c: axial young's modulus; Stresses are mean stresses for matrix and fiber.

$$f = .4$$

$$Cc = \left[Cm^{-1} - f\cdot((Cf - Cm)\cdot(S - f\cdot(S - I)) + Cm)^{-1}\cdot(Cf - Cm)\cdot Cm^{-1}\right]^{-1}$$

$$Sc = Cc^{-1}$$

$$E3c = \frac{1}{Sc_{3,3}}$$ **This is axial young's modulus**

$$E3c = 1.614\cdot 10^{11}$$ **As a check this works, as it is the young's modulus for the unreinforced matrix material**

$$\sigma a = \begin{bmatrix} 0 \\ 0 \\ -8.195\cdot 10^{8} \\ 0 \\ 0 \\ 0 \end{bmatrix} \quad Ea = Cm^{-1}\cdot\sigma a \qquad Ea = \begin{bmatrix} 0.003 \\ 0.003 \\ -0.009 \\ 0 \\ 0 \\ 0 \end{bmatrix}$$

Now, calculate the transformation strain for an applied strain and a thermal strain

$$\varepsilon thermal := -\left((Cm - Cf)\cdot(S - f\cdot(S - I)) - Cm\right)^{-1}\cdot Cf\cdot Etstar \qquad \varepsilon thermal = \begin{bmatrix} 0.002 \\ 0.002 \\ 0.002 \\ 0 \\ 0 \\ 0 \end{bmatrix}$$

$$\varepsilon load := \left((Cm - Cf)\cdot(S - f\cdot(S - I)) - Cm\right)^{-1}\cdot(Cm - Cf)\cdot Ea\cdot(-1) \qquad \varepsilon load = \begin{bmatrix} -0.003 \\ -0.003 \\ 0.009 \\ 0 \\ 0 \\ 0 \end{bmatrix}$$

$$\sigma mt := -f\cdot Cm\cdot(S - I)\cdot \varepsilon thermal \qquad \sigma mt = \begin{bmatrix} 6.296\cdot 10^{7} \\ 6.296\cdot 10^{7} \\ 6.296\cdot 10^{7} \\ 0 \\ 0 \\ 0 \end{bmatrix}$$

This is the mean matrix stress from thermal contraction

$$\sigma ft := (1 - f)\cdot Cm\cdot(S - I)\cdot \varepsilon thermal \qquad \sigma ft = \begin{bmatrix} -9.445\cdot 10^{7} \\ -9.445\cdot 10^{7} \\ -9.445\cdot 10^{7} \\ 0 \\ 0 \\ 0 \end{bmatrix}$$

This is the mean fiber stress from thermal contraction

$$E1c := \frac{1}{Sc_{1,1}}$$

This is transverse young's modulus

$$E1c = 1.614\cdot 10^{11}$$

$$\sigma mload := -f\cdot Cm\cdot(S - I)\cdot \varepsilon load \qquad \sigma mload = \begin{bmatrix} -3.915\cdot 10^{7} \\ -3.915\cdot 10^{7} \\ 1.463\cdot 10^{8} \\ 0 \\ 0 \\ 0 \end{bmatrix}$$

This is the mean matrix stress as a result of the applied load

$$\sigma\text{fload} = (1 - f)\cdot \text{Cm}\cdot(S - I)\cdot\varepsilon\text{load} \qquad \sigma\text{fload} = \begin{bmatrix} 5.873\cdot 10^{7} \\ 5.873\cdot 10^{7} \\ -2.194\cdot 10^{8} \\ 0 \\ 0 \\ 0 \end{bmatrix}$$

This is the mean fiber stress as a result of the applied load

$$\sigma\text{mtotal} = \sigma\text{mt} - \sigma\text{mload} \qquad \sigma\text{mtotal} = \begin{bmatrix} 2.381\cdot 10^{7} \\ 2.381\cdot 10^{7} \\ 2.092\cdot 10^{8} \\ 0 \\ 0 \\ 0 \end{bmatrix}$$

These are the total mean stresses as a result of the applied load and the therma contractions.

$$\sigma\text{ftotal} = \sigma\text{ft} + \sigma\text{fload} \qquad \sigma\text{ftotal} = \begin{bmatrix} -3.572\cdot 10^{7} \\ -3.572\cdot 10^{7} \\ -3.138\cdot 10^{8} \\ 0 \\ 0 \\ 0 \end{bmatrix}$$

$$\sigma\text{mave} = \sigma\text{a} + \sigma\text{mtotal}$$

Finally, we arrive at the average matrix and fiber stresses as a result of thermal expansion and applied load.

$$\sigma\text{mave} = \begin{bmatrix} 2.381\cdot 10^{7} \\ 2.381\cdot 10^{7} \\ -6.103\cdot 10^{8} \\ 0 \\ 0 \\ 0 \end{bmatrix}$$

$\sigma fave = \sigma a + \sigma ftotal$ $\quad\quad$ $\sigma fave = \begin{bmatrix} -3.572\cdot10^{7} \\ -3.572\cdot10^{7} \\ -1.133\cdot10^{9} \\ 0 \\ 0 \\ 0 \end{bmatrix}$

Finally, we can use the calculated stresses to compute the Von Mises stresses:

$$\sigma vmm = \sqrt{\frac{\left(\sigma mave_1 - \sigma mave_2\right)^2 + \left(\sigma mave_2 - \sigma mave_3\right)^2 + \left(\sigma mave_3 - \sigma mave_1\right)^2}{2}}$$

$\sigma vmm = 6.341\cdot10^{8}$

This is the Von Mises stress for the matrix; for the fiber it is:

$$\sigma vmf = \sqrt{\frac{\left(\sigma fave_1 - \sigma fave_2\right)^2 + \left(\sigma fave_2 - \sigma fave_3\right)^2 + \left(\sigma fave_3 - \sigma fave_1\right)^2}{2}}$$

$\sigma vmf = 1.098\cdot10^{9}$

APPENDIX III

ESHELBY EQUIVALENT INCLUSION METHOD
FOR THE
CALCULATION OF ELLIPSOID FIBER COMPOSITE STRESS

This is a program to calculate the stresses in a discontinuous fiber composite using Eshelby's method.

First, enter the material constants;

$Em = 96\cdot 10^{9}$ **Youngs modulus for the matrix**

$Ef = 410\cdot 10^{9}$ **Fiber modulus**

$vm = .36$ **Matrix and fiber poisson ratio**

$vf = 0.28$

$\alpha m = 8.5\cdot 10^{-6}$ **Matrix and fiber thermal expansion, per degree C**

$\alpha f = 4.5\cdot 10^{-6}$

$\Delta T = -350$ **Temperature through which cooling occurs, below Tg**

$\varepsilon tstar = (\alpha f - \alpha m)\cdot \Delta T$ **This is thermal strain resulting from cooling**

$ar = 25$ **Fiber aspect ratio; 1 for round particles**

$$Etstar = \begin{bmatrix} \varepsilon tstar \\ \varepsilon tstar \\ \varepsilon tstar \\ 0 \\ 0 \\ 0 \end{bmatrix} \qquad Etstar = \begin{bmatrix} 0.001 \\ 0.001 \\ 0.001 \\ 0 \\ 0 \\ 0 \end{bmatrix}$$

This is the thermal strain vector

Now, define compliance matricies for the matrix and reinforcement

$I = \text{identity}(6)$ $\quad Cm = \text{identity}(6)$ $\quad Cf = \text{identity}(6)$

$$Cm_{1,1} = Em\cdot\frac{1 - vm}{(1 - 2\cdot vm)\cdot(1 + vm)}$$

$Cm_{2,2} = Cm_{1,1}$ $\quad Cm_{3,3} = Cm_{1,1}$

$$Cm_{4,4} = \frac{Em}{2\cdot(1 + vm)}$$

$Cm_{5,5} = Cm_{4,4}$ $\quad Cm_{6,6} = Cm_{4,4}$

$$Cm_{1,2} = Em\cdot\frac{vm}{(1 - 2\cdot vm)\cdot(1 + vm)}$$

$Cm_{1,3} = Cm_{1,2}$ $\quad Cm_{2,1} = Cm_{1,2}$ $\quad Cm_{2,3} = Cm_{1,2}$ $\quad Cm_{3,1} = Cm_{1,2}$ $\quad Cm_{3,2} = Cm_{1,2}$

$$Cf_{1,1} = Ef\cdot\frac{1 - vf}{(1 - 2\cdot vf)\cdot(1 + vf)}$$

$Cf_{2,2} = Cf_{1,1}$ $\quad Cf_{3,3} := Cf_{1,1}$

$$Cf_{4,4} := \frac{Ef}{2\cdot(1 - vf)}$$

$Cf_{5,5} := Cf_{4,4}$ $\quad Cf_{6,6} := Cf_{4,4}$

$$Cf_{1,2} := Ef\cdot\frac{vf}{(1 - 2\cdot vf)\cdot(1 + vf)}$$

$Cf_{1,3} := Cf_{1,2}$ $\quad Cf_{2,1} := Cf_{1,2}$ $\quad Cf_{2,3} := Cf_{1,2}$ $\quad Cf_{3,1} := Cf_{1,2}$ $\quad Cf_{3,2} := Cf_{1,2}$

$$I = \begin{bmatrix} 1 & 0 & 0 & 0 & 0 & 0 \\ 0 & 1 & 0 & 0 & 0 & 0 \\ 0 & 0 & 1 & 0 & 0 & 0 \\ 0 & 0 & 0 & 1 & 0 & 0 \\ 0 & 0 & 0 & 0 & 1 & 0 \\ 0 & 0 & 0 & 0 & 0 & 1 \end{bmatrix}$$

$$Cm = \begin{bmatrix} 1.613\cdot10^{11} & 9.076\cdot10^{10} & 9.076\cdot10^{10} & 0 & 0 & 0 \\ 9.076\cdot10^{10} & 1.613\cdot10^{11} & 9.076\cdot10^{10} & 0 & 0 & 0 \\ 9.076\cdot10^{10} & 9.076\cdot10^{10} & 1.613\cdot10^{11} & 0 & 0 & 0 \\ 0 & 0 & 0 & 3.529\cdot10^{10} & 0 & 0 \\ 0 & 0 & 0 & 0 & 3.529\cdot10^{10} & 0 \\ 0 & 0 & 0 & 0 & 0 & 3.529\cdot10^{10} \end{bmatrix}$$

$$Cf = \begin{bmatrix} 5.241\cdot10^{11} & 2.038\cdot10^{11} & 2.038\cdot10^{11} & 0 & 0 & 0 \\ 2.038\cdot10^{11} & 5.241\cdot10^{11} & 2.038\cdot10^{11} & 0 & 0 & 0 \\ 2.038\cdot10^{11} & 2.038\cdot10^{11} & 5.241\cdot10^{11} & 0 & 0 & 0 \\ 0 & 0 & 0 & 1.602\cdot10^{11} & 0 & 0 \\ 0 & 0 & 0 & 0 & 1.602\cdot10^{11} & 0 \\ 0 & 0 & 0 & 0 & 0 & 1.602\cdot10^{11} \end{bmatrix}$$

Now, calculate the Eshelby S-tensor

$S := \text{identity}(6)$ **Initialize the S-tensor**

$A := \ln\left(ar + \sqrt{ar^2 - 1}\right)$ $\quad A = 3.912$ **Calculate constants for S-tensor**

$$I1 := 2\cdot ar\cdot\frac{\left[ar\cdot\sqrt{\left(ar^2 - 1\right)} - A\right]}{\left(ar^2 - 1\right)\cdot\sqrt{ar^2 - 1}} \qquad I1 = 1.991$$

$$Q := \frac{3}{8\cdot(1 - vm)} \qquad Q = 0.586$$

$$R := \frac{1 - 2\cdot vm}{8\cdot(1 - vm)} \qquad R = 0.055$$

$$T = Q\cdot\frac{(4-3\cdot I1)}{3\cdot\left(ar^2-1\right)} \qquad T = -6.172\cdot 10^{-4}$$

$$S_{1,1} = Q + R\cdot I1 + 3\cdot\frac{T}{4} \qquad S_{1,1} = 0.694$$

$$S_{2,2} = S_{1,1}$$

$$S_{3,3} = 4\cdot\frac{Q}{3} + R\cdot(4-2\cdot I1) + 2\cdot ar^2\cdot T \qquad S_{3,3} = 0.011$$

$$S_{1,2} = \frac{Q}{3} - R\cdot I1 + 4\cdot\frac{T}{3} \qquad S_{1,2} = 0.086$$

$$S_{2,1} = S_{1,2}$$

$$S_{1,3} = -R\cdot I1 - ar^2\cdot T \qquad S_{1,3} = 0.277$$

$$S_{2,3} = S_{1,3}$$

$$S_{3,1} = -R\cdot(4-2\cdot I1) - T \qquad S_{3,1} = -4.046\cdot 10^{-4}$$

$$S_{3,2} = S_{3,1}$$

$$S_{4,4} = 4\cdot R - I1\cdot R - \left(1-ar^2\right)\cdot T \qquad S_{4,4} = 0.496$$

$$S_{5,5} = S_{4,4}$$

$$S_{6,6} = 2\cdot\frac{Q}{3} + 2\cdot I1\cdot R + \frac{T}{2} \qquad S_{6,6} = 0.608$$

$$S = \begin{bmatrix} 0.694 & 0.086 & 0.277 & 0 & 0 & 0 \\ 0.086 & 0.694 & 0.277 & 0 & 0 & 0 \\ -4.046\cdot 10^{-4} & -4.046\cdot 10^{-4} & 0.011 & 0 & 0 & 0 \\ 0 & 0 & 0 & 0.496 & 0 & 0 \\ 0 & 0 & 0 & 0 & 0.496 & 0 \\ 0 & 0 & 0 & 0 & 0 & 0.608 \end{bmatrix}$$

Now the physical constants can be calculated for the fiber fraction, f. Cc: composite stiffness E3c: axial young's modulus; Stresses are mean stresses for matrix and fiber.

$$f = .4$$

$$Cc = \left[Cm^{-1} - f\cdot((Cf - Cm)\cdot(S - f\cdot(S - I)) + Cm)^{-1}\cdot(Cf - Cm)\cdot Cm^{-1}\right]^{-1}$$

$$Sc = Cc^{-1}$$

$$E3c = \frac{1}{Sc_{3,3}}$$

This is axial young's modulus

$$E3c = 2.191\cdot 10^{11}$$

As a check this works, as it is the young's modulus for the unreinforced matrix material

$$\sigma a = \begin{bmatrix} 0 \\ 0 \\ -8.195\cdot 10^{8} \\ 0 \\ 0 \\ 0 \end{bmatrix} \quad Ea = Cm^{-1}\cdot\sigma a \quad Ea = \begin{bmatrix} 0.003 \\ 0.003 \\ -0.009 \\ 0 \\ 0 \\ 0 \end{bmatrix}$$

Now, calculate the transformation strain for an applied strain and a thermal strain

$$\varepsilon thermal = -((Cm - Cf)\cdot(S - f\cdot(S - I)) - Cm)^{-1}\cdot Cf\cdot Etstar \qquad \varepsilon thermal = \begin{bmatrix} 0.001 \\ 0.001 \\ 0.003 \\ 0 \\ 0 \\ 0 \end{bmatrix}$$

$$\varepsilon load = ((Cm - Cf)\cdot(S - f\cdot(S - I)) - Cm)^{-1}\cdot(Cm - Cf)\cdot Ea\cdot(-1) \qquad \varepsilon load = \begin{bmatrix} -0.005 \\ -0.005 \\ 0.012 \\ 0 \\ 0 \\ 0 \end{bmatrix}$$

$$\sigma mt = -f\cdot Cm\cdot(S - I)\cdot\varepsilon thermal \qquad \sigma mt = \begin{bmatrix} 4.555\cdot 10^{7} \\ 4.555\cdot 10^{7} \\ 1.285\cdot 10^{8} \\ 0 \\ 0 \\ 0 \end{bmatrix}$$

This is the mean matrix stress from thermal contraction

$$\sigma ft = (1 - f)\cdot Cm\cdot(S - I)\cdot\varepsilon thermal \qquad \sigma ft = \begin{bmatrix} -6.832\cdot 10^{7} \\ -6.832\cdot 10^{7} \\ -1.928\cdot 10^{8} \\ 0 \\ 0 \\ 0 \end{bmatrix}$$

This is the mean fiber stress from thermal contraction

$E1c := \frac{1}{Sc_{1,1}}$ **This is transverse young's modulus**

$E1c = 1.592 \cdot 10^{11}$

$$\sigma mload := -f \cdot Cm \cdot (S - I) \cdot \varepsilon load \qquad \sigma mload = \begin{bmatrix} -7.236 \cdot 10^{6} \\ -7.236 \cdot 10^{6} \\ 4.502 \cdot 10^{8} \\ 0 \\ 0 \\ 0 \end{bmatrix}$$

This is the mean matrix stress as a result of the applied load

$$\sigma fload := (1 - f) \cdot Cm \cdot (S - I) \cdot \varepsilon load \qquad \sigma fload = \begin{bmatrix} 1.085 \cdot 10^{7} \\ 1.085 \cdot 10^{7} \\ -6.752 \cdot 10^{8} \\ 0 \\ 0 \\ 0 \end{bmatrix}$$

This is the mean fiber stress as a result of the applied load

$$\sigma mtotal := \sigma mt + \sigma mload \qquad \sigma mtotal = \begin{bmatrix} 3.831 \cdot 10^{7} \\ 3.831 \cdot 10^{7} \\ 5.787 \cdot 10^{8} \\ 0 \\ 0 \\ 0 \end{bmatrix}$$

These are the total mean stresses as a result of the applied load and the thermal contractions.

$$\sigma ftotal := \sigma ft + \sigma fload \qquad \sigma ftotal = \begin{bmatrix} -5.747 \cdot 10^{7} \\ -5.747 \cdot 10^{7} \\ -8.68 \cdot 10^{8} \\ 0 \\ 0 \\ 0 \end{bmatrix}$$

$$\sigma mave := \sigma a + \sigma mtotal \qquad \sigma mave = \begin{bmatrix} 3.831 \cdot 10^{7} \\ 3.831 \cdot 10^{7} \\ -2.408 \cdot 10^{8} \\ 0 \\ 0 \\ 0 \end{bmatrix}$$

Finally, we arrive at the average matrix and fiber stresses as a result of thermal expansion and applied load.

$\sigma fave := \sigma a + \sigma ftotal$

$$\sigma fave = \begin{bmatrix} -5.747 \cdot 10^{7} \\ -5.747 \cdot 10^{7} \\ -1.688 \cdot 10^{9} \\ 0 \\ 0 \\ 0 \end{bmatrix}$$

Finally, we can use the calculated stresses to compute the Von Mises stresses:

$$\sigma vmm := \sqrt{\frac{\left(\sigma mave_1 - \sigma mave_2\right)^2 + \left(\sigma mave_2 - \sigma mave_3\right)^2 + \left(\sigma mave_3 - \sigma mave_1\right)^2}{2}}$$

$\sigma vmm = 2.791 \cdot 10^{8}$

This is the Von Mises stress for the matrix; for the fiber it is:

$$\sigma vmf := \sqrt{\frac{\left(\sigma fave_1 - \sigma fave_2\right)^2 + \left(\sigma fave_2 - \sigma fave_3\right)^2 + \left(\sigma fave_3 - \sigma fave_1\right)^2}{2}}$$

$\sigma vmf = 1.63 \cdot 10^{9}$

APPENDIX IV

ESHELBY EQUIVALENT INCLUSION METHOD FOR THE CALCULATION OF CONTINUOUS FIBER COMPOSITE STRESS

This is a program to calculate the stresses in a continuous fiber composite using Eshelby's method.

First, enter the material constants;

$Em = 96\cdot 10^{9}$ **Youngs modulus for the matrix**

$Ef := 410\cdot 10^{9}$ **Fiber modulus**

$vm = .36$ **Matrix and fiber poisson ratio**

$vf = 0.28$

$\alpha m = 8.5\cdot 10^{-6}$ **Matrix and fiber thermal expansion, per degree C**

$\alpha f = 4.5\cdot 10^{-6}$

$\Delta T = -350$ **Temperature through which cooling occurs, below Tg**

$\epsilon tstar = (\alpha f - \alpha m)\cdot \Delta T$ **This is thermal strain resulting from cooling**

$$Etstar = \begin{bmatrix} \epsilon tstar \\ \epsilon tstar \\ \epsilon tstar \\ 0 \\ 0 \\ 0 \end{bmatrix} \qquad Etstar = \begin{bmatrix} 0.001 \\ 0.001 \\ 0.001 \\ 0 \\ 0 \\ 0 \end{bmatrix}$$

This is the thermal strain vector

Now, define compliance matricies for the matrix and reinforcement

$I = \text{identity}(6) \qquad Cm = \text{identity}(6) \qquad Cf = \text{identity}(6)$

$$Cm_{1,1} = Em\cdot\frac{1 - vm}{(1 - 2\cdot vm)\cdot(1 + vm)}$$

$Cm_{2,2} = Cm_{1,1} \qquad Cm_{3,3} = Cm_{1,1}$

$$Cm_{4,4} = \frac{Em}{2\cdot(1 + vm)}$$

$Cm_{5,5} = Cm_{4,4} \qquad Cm_{6,6} = Cm_{4,4}$

$$Cm_{1,2} = Em\cdot\frac{vm}{(1 - 2\cdot vm)\cdot(1 + vm)}$$

$Cm_{1,3} = Cm_{1,2} \qquad Cm_{2,1} = Cm_{1,2} \qquad Cm_{2,3} = Cm_{1,2} \qquad Cm_{3,1} = Cm_{1,2} \qquad Cm_{3,2} = Cm_{1,2}$

$$Cf_{1,1} = Ef\cdot\frac{1 - vf}{(1 - 2\cdot vf)\cdot(1 + vf)}$$

$Cf_{2,2} = Cf_{1,1} \qquad Cf_{3,3} = Cf_{1,1}$

$$Cf_{4,4} = \frac{Ef}{2\cdot(1+vf)}$$

$Cf_{5,5} = Cf_{4,4}$ $\quad$ $Cf_{6,6} = Cf_{4,4}$

$$Cf_{1,2} = Ef\cdot\frac{vf}{(1-2\cdot vf)\cdot(1+vf)}$$

$Cf_{1,3} = Cf_{1,2}$ $\quad$ $Cf_{2,1} = Cf_{1,2}$ $\quad$ $Cf_{2,3} = Cf_{1,2}$ $\quad$ $Cf_{3,1} = Cf_{1,2}$ $\quad$ $Cf_{3,2} = Cf_{1,2}$

$$I = \begin{bmatrix} 1 & 0 & 0 & 0 & 0 & 0 \\ 0 & 1 & 0 & 0 & 0 & 0 \\ 0 & 0 & 1 & 0 & 0 & 0 \\ 0 & 0 & 0 & 1 & 0 & 0 \\ 0 & 0 & 0 & 0 & 1 & 0 \\ 0 & 0 & 0 & 0 & 0 & 1 \end{bmatrix}$$

$$Cm = \begin{bmatrix} 1.613\cdot10^{11} & 9.076\cdot10^{10} & 9.076\cdot10^{10} & 0 & 0 & 0 \\ 9.076\cdot10^{10} & 1.613\cdot10^{11} & 9.076\cdot10^{10} & 0 & 0 & 0 \\ 9.076\cdot10^{10} & 9.076\cdot10^{10} & 1.613\cdot10^{11} & 0 & 0 & 0 \\ 0 & 0 & 0 & 3.529\cdot10^{10} & 0 & 0 \\ 0 & 0 & 0 & 0 & 3.529\cdot10^{10} & 0 \\ 0 & 0 & 0 & 0 & 0 & 3.529\cdot10^{10} \end{bmatrix}$$

$$Cf = \begin{bmatrix} 5.241\cdot10^{11} & 2.038\cdot10^{11} & 2.038\cdot10^{11} & 0 & 0 & 0 \\ 2.038\cdot10^{11} & 5.241\cdot10^{11} & 2.038\cdot10^{11} & 0 & 0 & 0 \\ 2.038\cdot10^{11} & 2.038\cdot10^{11} & 5.241\cdot10^{11} & 0 & 0 & 0 \\ 0 & 0 & 0 & 1.602\cdot10^{11} & 0 & 0 \\ 0 & 0 & 0 & 0 & 1.602\cdot10^{11} & 0 \\ 0 & 0 & 0 & 0 & 0 & 1.602\cdot10^{11} \end{bmatrix}$$

Now, calculate the Eshelby S-tensor

$S = \mathrm{identity}(6)$ $\quad$ **Initialize the S-tensor**

$$S_{1,1} = \frac{5-vm}{8\cdot(1-vm)}$$

$S_{2,2} = S_{1,1}$

$S_{3,3} = 0$

$$S_{1,2} = \frac{4\cdot vm-1}{8\cdot(1-vm)}$$

$S_{2,1} = S_{1,2}$

$S_{1,3} = \frac{vm}{2\cdot(1 - vm)}$

$S_{2,3} = S_{1,3}$

$S_{2,3} = S_{1,3}$ $\quad S_{3,1} = 0$

$S_{3,2} = 0$

$S_{4,4} = \frac{1}{4}$

$S_{5,5} = S_{4,4}$

$S_{6,6} = \frac{3 - 4\cdot vm}{8\cdot(1 - vm)}$

$$S = \begin{bmatrix} 0.906 & 0.086 & 0.281 & 0 & 0 & 0 \\ 0.086 & 0.906 & 0.281 & 0 & 0 & 0 \\ 0 & 0 & 0 & 0 & 0 & 0 \\ 0 & 0 & 0 & 0.25 & 0 & 0 \\ 0 & 0 & 0 & 0 & 0.25 & 0 \\ 0 & 0 & 0 & 0 & 0 & 0.305 \end{bmatrix}$$

Now the physical constants can be calculated for the fiber fraction, f. Cc: composite stiffness E3c: axial young's modulus; Stresses are mean stresses for matrix and fiber.

$f = .4$

$Cc = \left[Cm^{-1} - f\cdot((Cf - Cm)\cdot(S - f\cdot(S - I)) + Cm)^{-1}\cdot(Cf - Cm)\cdot Cm^{-1}\right]^{-1}$

$Sc = Cc^{-1}$

$E3c = \frac{1}{Sc_{3,3}}$ **This is axial young's modulus**

$E3c = 2.192\cdot10^{11}$ **As a check this works, as it is the young's modulus for the unreinforced matrix material**

$$\sigma a = \begin{bmatrix} 0 \\ 0 \\ -8.195\cdot 10^{8} \\ 0 \\ 0 \\ 0 \end{bmatrix} \quad Ea = Cm^{-1}\cdot\sigma a \quad Ea = \begin{bmatrix} 0.003 \\ 0.003 \\ -0.009 \\ 0 \\ 0 \\ 0 \end{bmatrix}$$

Now, calculate the transformation strain for an applied strain and a thermal strain

$$\varepsilon thermal = -((Cm - Cf)\cdot(S - f\cdot(S - I)) - Cm)^{-1}\cdot Cf\cdot Etstar \qquad \varepsilon thermal = \begin{bmatrix} 0.001 \\ 0.001 \\ 0.003 \\ 0 \\ 0 \\ 0 \end{bmatrix}$$

$$\varepsilon load = ((Cm - Cf)\cdot(S - f\cdot(S - I)) - Cm)^{-1}\cdot(Cm - Cf)\cdot Ea\cdot(-1) \qquad \varepsilon load = \begin{bmatrix} -0.004 \\ -0.004 \\ 0.012 \\ 0 \\ 0 \\ 0 \end{bmatrix}$$

$$\sigma mt = -f\cdot Cm\cdot(S - I)\cdot\varepsilon thermal \qquad \sigma mt = \begin{bmatrix} 2.12\cdot 10^{7} \\ 2.12\cdot 10^{7} \\ 1.138\cdot 10^{8} \\ 0 \\ 0 \\ 0 \end{bmatrix}$$

This is the mean matrix stress from thermal contraction

$$\sigma ft = (1 - f)\cdot Cm\cdot(S - I)\cdot\varepsilon thermal \qquad \sigma ft = \begin{bmatrix} -3.18\cdot 10^{7} \\ -3.18\cdot 10^{7} \\ -1.708\cdot 10^{8} \\ 0 \\ 0 \\ 0 \end{bmatrix}$$

This is the mean fiber stress from thermal contraction

$$E1c = \frac{1}{Sc_{1,1}}$$

This is transverse young's modulus

$$E1c = 1.494\cdot 10^{11}$$

$$\sigma mload = -f\cdot Cm\cdot(S - I)\cdot \varepsilon load \quad \sigma mload = \begin{bmatrix} 9.191\cdot 10^{7} \\ 9.191\cdot 10^{7} \\ 5.268\cdot 10^{8} \\ 0 \\ 0 \\ 0 \end{bmatrix}$$

This is the mean matrix stress as a result of the applied load

$$\sigma fload = (1 - f)\cdot Cm\cdot(S - I)\cdot \varepsilon load \quad \sigma fload = \begin{bmatrix} -1.379\cdot 10^{8} \\ -1.379\cdot 10^{8} \\ -7.903\cdot 10^{8} \\ 0 \\ 0 \\ 0 \end{bmatrix}$$

This is the mean fiber stress as a result of the applied load

$$\sigma mtotal = \sigma mt + \sigma mload \quad \sigma mtotal = \begin{bmatrix} 1.131\cdot 10^{8} \\ 1.131\cdot 10^{8} \\ 6.407\cdot 10^{8} \\ 0 \\ 0 \\ 0 \end{bmatrix}$$

These are the total mean stresses as a result of the applied load and the thermal contractions.

$$\sigma ftotal = \sigma ft + \sigma fload \quad \sigma ftotal = \begin{bmatrix} -1.697\cdot 10^{8} \\ -1.697\cdot 10^{8} \\ -9.61\cdot 10^{8} \\ 0 \\ 0 \\ 0 \end{bmatrix}$$

$$\sigma mave = \sigma a - \sigma mtotal \quad \sigma mave = \begin{bmatrix} 1.131\cdot 10^{8} \\ 1.131\cdot 10^{8} \\ -1.788\cdot 10^{8} \\ 0 \\ 0 \\ 0 \end{bmatrix}$$

Finally, we arrive at the average matrix and fiber stresses as a result of thermal expansion and applied load.

$\sigma fave = \sigma a + \sigma ftotal$

$$\sigma fave = \begin{bmatrix} -1.697\cdot 10^{8} \\ -1.697\cdot 10^{8} \\ -1.781\cdot 10^{9} \\ 0 \\ 0 \\ 0 \end{bmatrix}$$

Finally, we can use the calculated stresses to compute the Von Mises stresses:

$$\sigma vmm = \sqrt{\frac{\left(\sigma mave_1 - \sigma mave_2\right)^2 + \left(\sigma mave_2 - \sigma mave_3\right)^2 + \left(\sigma mave_3 - \sigma mave_1\right)^2}{2}}$$

$\sigma vmm = 2.919\cdot 10^{8}$

This is the Von Mises stress for the matrix; for the fiber it is:

$$\sigma vmf = \sqrt{\frac{\left(\sigma fave_1 - \sigma fave_2\right)^2 + \left(\sigma fave_2 - \sigma fave_3\right)^2 + \left(\sigma fave_3 - \sigma fave_1\right)^2}{2}}$$

$\sigma vmf = 1.611\cdot 10^{9}$